THE UNIVERSITY *of* EDINBURGH

Computational analysis of interactions between AMPA receptor and con-ikot-ikot conotoxin

Natalia Szlachetka

Doctor of Philosophy

UKRI Centre for Doctoral Training in Biomedical AI
School of Informatics
University of Edinburgh

2025

Abstract

AMPA receptors (AMPARs) are a subtype of ionotropic glutamate receptors (iGluRs) found in excitatory synapses in the central nervous system, where they mediate the majority of excitatory synaptic transmission. AMPARs are encoded by 4 different genes, *GRIA1–4*, whose protein products assemble into functional tetramers. *In vivo*, AMPARs can be present as homomers, diheteromers and triheteromers. Each of these AMPAR subtypes has specific kinetics, expression profile and hence a distinct physiological role. Synapses involved in information storage change their AMPAR subunit composition as well as the total number of AMPARs. This phenomenon is known as synaptic plasticity and is widely recognised as the molecular mechanism underlying the processes of memory formation and learning. However, to date, there are no known compounds that specifically recognise one AMPAR subunit composition over the other.

Con-ikot-ikot (CII), a naturally occurring conotoxin found in the venom of a marine cone snail *Conus striatus*, specifically binds to AMPARs with EC_{50} of $\sim$5 nM and exhibits unique potential to serve as a scaffold to generate novel, heteromer-specific AMPAR binders and modulators. Its unique binding site, localised within the AMPAR extracellular domains, where it makes contacts with all 4 subunits, might provide a starting point for design of heteromer-specific binders. At the same time, its small size, minimal perturbation of AMPAR size (about 1 nm increase in receptor height), 1:1 binding stoichiometry and the fact that it leaves AMPAR extracellular domains open for physiological interactions make it an attractive, novel labelling tool for fluorescent studies of AMPARs, including super-resolution imaging (SRI).

SRI was essential in demonstrating activity-dependent changes in AMPAR numbers within synapses. In these experiments, AMPARs are labelled with a fluorescent tag either by genetic fusions (e.g. GFP or Halo tag) or by fluorescently labelled antibodies. While overexpression of genetic fusions can lead to non-physiological conditions, antibodies are large (10–15 nm in size) and almost all bind to the surface of AMPAR extracellular domains. This could significantly hinder free movement of AMPARs into and out of the already crowded and narrow synaptic space, where AMPAR extracellular domains interact with other synaptic and presynaptic proteins. CII toxin has the potential to overcome all these limitations.

Here, I explore the interactions between CII toxin and AMPARs using computational approaches followed by experimental validation of the results. I have performed a series of molecular dynamics simulations and developed NAppEd – a novel approach to analyse the resulting trajectories based on residue interaction network analysis. Using NAppEd in combination with computational alanine scanning, I have confirmed residues known to be important for the interaction between the toxin and AMPAR and identified new interactions. Importantly, this includes a network of novel interactions between the toxin and the AMPAR amino-terminal domains (ATDs). This interaction network is of particular importance as ATD sequence varies

between AMPAR subunit types. My analysis identifies CII as the only known non-antibody AMPAR binder that interacts with AMPAR ATDs. The results of computational analyses were validated by mutating CII tyrosine 54 into alanine (Y54A), identified as one of the strongest interactors with AMPARs by NAppEd. The single-point mutant resulted in a right-shift in CII dose response curve in electrophysiology experiments, validating the computational findings.

These results, along with additional computational analyses showing minimal effects of fluorescent labelling on CII binding to AMPARs, confirm the unique potential of the CII as a novel fluorescent probe and as a scaffold for design of AMPAR-heteromer specific binders for investigation of AMPARs.

Lay summary

AMPA receptors (AMPARs) are proteins found at the points of neuronal connections (synapses) in the brain. They take part in the transmission of information through the synapse and have an important role in the processes of learning and memory, in which they move into and out of sites within the synapse. These movements can be studied using advanced microscopy techniques that use specialised tools to track AMPARs. The tools commonly used to do this often prevent the receptors from moving in a way they normally would because of their large size, or from interacting with other proteins present in the synapse because of where they attach to the receptors.

Con-ikot-ikot (CII) is a toxin found in the venom of a tropical sea snail. It binds to AMPARs at a unique binding site located within the receptor and does not bind to any of the closely related proteins, which makes it a good candidate for developing scientific tools to study AMPA receptors. Because of its small size and unusual binding site, it also does not obstruct AMPARs' movements or their interactions with other proteins. By making changes to the toxin, we could make it even better for different types of studies, for example looking at how different types of AMPARs move at the synapse or adjusting the properties of a group of AMPARs.

In this thesis, I used computational methods to study the interactions between AMPARs and CII. I ran molecular dynamics (MD) simulations of the protein complex and developed a new network analysis tool – NAppEd – to analyse them to understand which parts of the toxin are the most important for its interaction with AMPAR. I also produced the toxin in bacteria in two versions: as it exists in nature and in a variant altered in a way that should weaken its interaction with AMPAR. Testing those two toxin variants for how strongly they interact with AMPAR showed that our prediction from computational results was correct. This suggests that the network analysis tool can be useful in finding out which parts of the protein could be altered to change the binding of two protein interaction partners. Such information could be used to help understand protein complexes, design scientific tools and protein-based drugs.

Acknowledgements

This thesis could never have happened without the many people who have supported, helped, and encouraged me throughout my PhD journey.

Firstly, I would like to express my gratitude to my two PhD supervisors, Dr Jelena Baranovic and Dr Christopher Wood. I cannot imagine having a better, more supportive pair of supervisors for my Masters and PhD journey. Thank you for your unending support and patience, and for being there for me not only as academics and mentors, but also as people.

Thank you also to Dr Douglas Houston for his thoughtful feedback and encouragement as annual review panel member.

Many thanks to all of the people who contributed to carrying out the work presented in this thesis: Jana Hennelova and Manaal Shah for their summer project work on the MD simulations of (to Manaal also for her work on some of the NAppEd code), Matthew Turner for his help with silver staining of SDS-PAGE gels and fluorescent labelling of the WT toxin, Dr Chigdem Arslan for preparing the DNA constructs for CII toxin mutants, Alexander Edwards for conducting the electrophysiology experiments, and Rhona Cowan from the University of Edinburgh School of Chemistry's Mass Spectrometry facility for conducting the MS analysis of labelled toxin. I would also like to thank the Ellgaard lab at the University of Copenhagen for their kind gift of the csCyDisCo plasmid and support with planning our csCyDisCo CII expression experiment. Thank you to Dr Martin Wear and Dr Matthew Nowicki personally for their help with the practical aspects of toxin purification, and to EPPF facility for making available the equipment required to complete the wet lab work. I would also like to thank Alison Fulton, who has always been exceptionally understanding about the many liters of 15x LB I would order ahead of my purification rounds and just as many full trolleys of liquid waste I would bring to be decontaminated after each round, and has always been happy to answer any of my questions.

Thank you to all of the members of the Baranovic and Wood labs for feedback and support, especially to Dr Chigdem Arslan, who has been like a lab mum to me. I've had some great times with the members of both groups and hope for many more.

Special thanks to Rebecca Pfister and Shilpa Balaram, whose support has been instrumental to my life and growth as a person and a young researcher.

Finally, thank you to my friends and family, who have been with me day in and day out and never stopped believing in me. Thank you to those who are not here and can't see me getting so close to the finish line of my PhD but who I know have been cheering me on from above the whole time.

This work was supported by the United Kingdom Research and Innovation (grant EP/S02431X/1), UKRI Centre for Doctoral Training in Biomedical AI at the University of Edinburgh, School of Informatics.

Table of Contents

Chapter 1

Introduction

1.1 AMPA receptors

1.1.1 Ionotropic glutamate receptors

Ionotropic glutamate receptors (iGluRs) are cation-permeable ligand-gated ion channels activated by the neurotransmitter glutamate. iGluRs are divided into functional classes on the basis of their highly specific synthetic agonists: *N*-methyl-D-aspartic acid (NMDA) receptors (NMDARs), α-amino-3-hydroxy-5-methyl-4-isoxazolepropionic acid (AMPA) receptors (AMPARs), and kainate (KA) receptors. Delta (δ) glutamate receptors (GluD receptors) are included in the family due to sequence homology [1, 2, 3] but do not bind glutamate [1, 3] and their physiological function in the central nervous system remains poorly understood [4, 5].

All ionotropic glutamate receptors are tetramers and their assembly as homo- or heterotetramers depends on the class they belong to (AMPARs and kainate receptors can form functional homo- and heterotetramers, NMDARs are obligate heterotetramers, and δ receptors exist as homotetramers; whether they can assemble as heteromers remains unknown). All subunit types of AMPAR (GluA1–4) and kainate receptors (GluK1–5) bind glutamate, but of NMDAR subunits (GluN1, GluN2A–D, GluN3A–B), only GluN2 subunits are glutamate-binding, while GluN1 and GluN3 bind glycine and D-serine, similarly to delta glutamate receptor subunits GluD1–2 [6] (Figure 1.1 A). Recent studies have found that GluD1 receptors, uniquely present not only at excitatory, but also inhibitory synapses [7], also bind GABA and play a role in driving inhibitory synaptic plasticity [8].

Subunits of all iGluRs share a common structural organisation, with each consisting of four domains – extracellular amino-terminal domain (ATD) and ligand-binding domain (LBD; composed of two stretches of amino acids separated in the primary sequence), membrane-spanning transmembrane domain (TMD), and cytoplasmic carboxy-terminal domain (CTD) – connected by flexible linkers and arranged in the same way in the primary sequence of all subunits (Figure

1.1 B). When four subunits come together to form a functional receptor, the domains assemble into layers, with the transmembrane domains forming the ion channel pore [6].

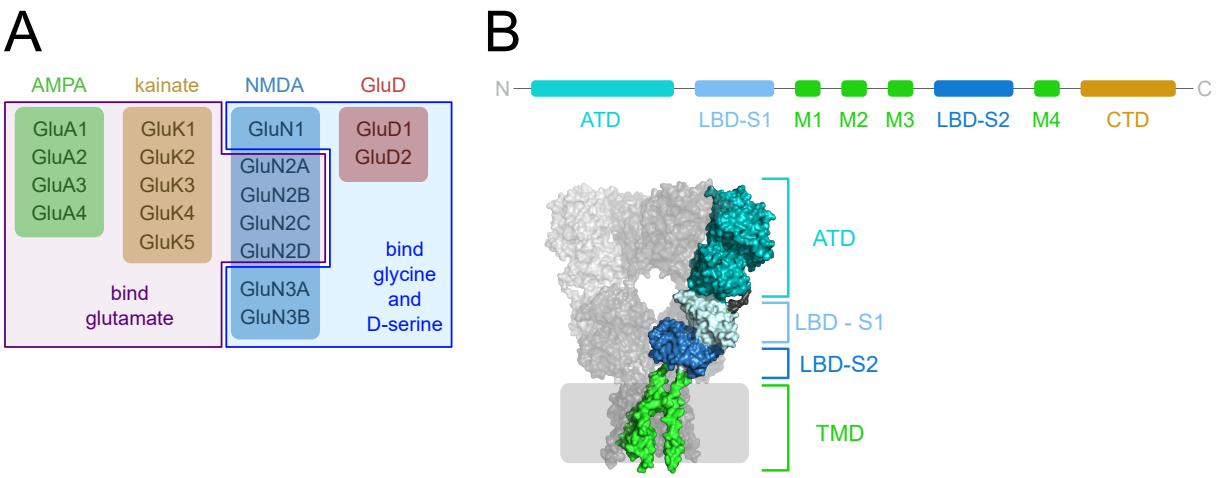

Figure 1.1: A. iGluR functional classes: subunits and their ligands. B. iGluR structural organisation. Top: linear architecture of an iGluR subunit. Bottom: A single subunit in an example iGluR shown in the same colour scheme; other subunits shown in grey. Carboxy-terminal domain was not resolved as it is structurally disordered. PDB ID: 3KG2 [9].

1.1.2 AMPAR structure

AMPA receptors (AMPARs) share the tetrameric structure exhibited by other ionotropic glutamate receptors [9]. Functional receptors are assembled from protein products of four genes – *GluA1–4* (also referred to as *GluR1–4* or *GRIA1–4*) – which exist in a variety of isoforms due to mRNA splicing (e.g. flip/flop variants present in all subunit types [10]) and editing (e.g. Q/R editing in GluA2 subunits [11]). Different AMPAR subtypes vary with respect to their spatial and temporal expression [10, 12] and functional properties [10, 13], e.g. AMPARs containing GluA2(R) edited subunits (representing virtually all of GluA2-containing AMPARs in the rodent and human brain [14, 15]) are calcium-impermeable due to the positive charge introduced by the arginine residue [16], while GluA2-lacking AMPARs are calcium-permeable [16, 17]; flip and flop isoforms exhibit different desensitization and deactivation kinetics [18] and sensitivity to some allosteric modulators, such as cyclothiazide (CTZ) [19].

Functional AMPARs can adopt a variety of subunit compositions, ranging from homotetrameric (e.g. GluA2), to diheterotetrameric (e.g. GluA1A2A1A2), to triheterotetrameric (e.g. GluA1A2A3A2), with GluA1-GluA2 and GluA2-GluA3 heteromers together comprising the majority of native AMPARs and A1A2A3A2 AMPARs representing around 25% of the AMPAR population [20]. Exchanging the synaptic composition of AMPAR subtypes is one of the mechanisms of synaptic plasticity [21].

Like other iGluR subunits, each AMPAR subunit consists of four domains, connected by flexible linkers, which form layers in the overall structure of the receptor (Figure 1.1 B):

- extracellular amino-terminal domains (ATDs), also referred to as N-terminal domains (NTDs), are a site for AMPAR interactions with other proteins present in the synaptic cleft [22] and play a role in the assembly and trafficking of the receptors [23, 24]. While they are not essential for the ion channel function of the receptor, their removal has been shown to alter some of the functional properties of AMPAR [25]

- extracellular ligand-binding domains (LBDs), also referred to as agonist-binding domains (ABDs) [6, 26], are responsible for binding the physiological ligand of the receptor – full agonist, glutamate – released from the presynaptic neuron's neurotransmitter vesicles, as well as other ligands (such as synthetic agonist AMPA [27] or competitive antagonist NBQX [28])

- membrane-spanning transmembrane domains (TMDs) are composed of M1, M3, and M4 helices and a reentrant M2 pore loop and make up the ion channel which opens and shuts in the functional cycle of an AMPA receptor

- cytosolic carboxy-terminal domains (CTDs) are structurally disordered and have a role in receptor regulation and localization through their interactions with intracellular scaffolding, adaptor, and signalling proteins [29, 30, 31].

The four positions occupied by individual subunits in the overall structure of an AMPA receptor, denoted A, B, C, and D (Figure 1.2), can be divided into two distinct pairs: A/C and B/D. Subunits occupying these positions are conformationally similar within subunit pairs, but different between pairs [9]. The B/D positions in heteromeric GluA2-containing AMPARs are predominantly occupied by GluA2 subunits, whereas GluA1 and GluA3 subunits preferentially occupy positions A/C [20]. An interesting structural feature of AMPARs, shared by most of the other iGluRs is the "domain swapping" or "subunit crossover", which is observed between the LBD and ATD layers of the receptor (it is not observed in delta iGluRs [32, 33] and recently, a non-domain-swapped conformation has also been identified in $\sim$20% GluA1 homotetramers [34]). In both layers, the same domains from the four subunits form pairs ("local dimers"); however, this pairing occurs between different subunits in the ATD layer (A+B and C+D pairing) and the LBD layer (A+D and B+C pairing) (Figure 1.2). While the ATD and LBD layers display two-fold rotational symmetry, the membrane-spanning ion channel pore formed by the TMDs is four-fold symmetrical [9].

Native AMPA receptors typically assemble with auxiliary proteins, which include transmembrane AMPAR regulatory proteins (TARPs) [35, 36], cornichon homologs (CNIHs) [37], cysteine-knot AMPA receptor modulating proteins (CKAMPs, also known as SHISA proteins)

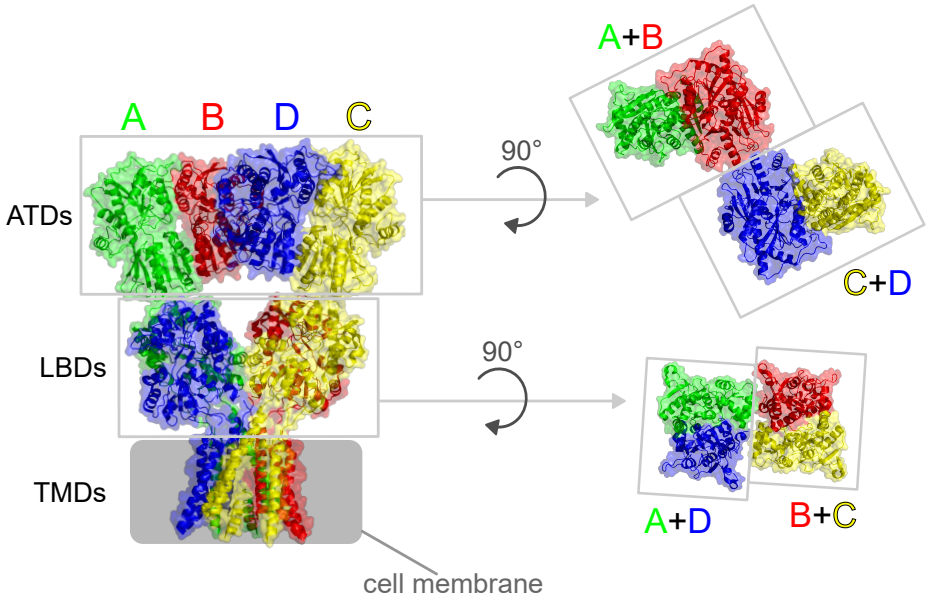

Figure 1.2: AMPAR structure. Left: full-length AMPAR (PDB ID: 3KG2 [9]). Right: Top view of the dimer-of-dimers arrangement of amino-terminal domains (top) and ligand-binding domains (bottom).

[38], GSG1L (GSG1-like protein / germ cell-specific gene 1-like protein) [39], and SynDIG4/Prrt1 (synapse differentiation-induced gene 4 / proline-rich transmembrane protein 1) [40]. These transmembrane accessory proteins do not have receptor or ion channel function themselves; instead, they associate with AMPARs in a non-transient manner and can modify their localisation and trafficking [35], as well as functional properties such as gating kinetics [38, 41] and ion permeation [42], further contributing to the vast diversity of AMPAR functional and structural landscape, especially taking into account that multiple types of auxiliary subunits can associate with the same receptor simultaneously and regulate its function together [43, 44].

Apart from the interactions with AMPAR auxiliary subunits, the receptors also form a number of contacts with other transmembrane, cytoplasmic, and secreted proteins [22]. One important example of this is PSD-95 (also known as SAP-90 or DLG4), a scaffolding protein which AMPARs bind indirectly through associated TARPs [45, 46]. PSD-95 is a major component of the excitatory postsynaptic density (PSD), a protein-dense area in the postsynaptic membrane, and contributes to trapping AMPARs in receptor nanodomains, which are typically ∼70–80 nm across and contain ∼20 receptors each [47, 48, 49, 50]. These AMPAR nanodomains are spatially aligned with the presynaptic neurotransmitter release sites in so-called trans-synaptic nanocolumns [51]. As PSD-95 itself aligns with the presynaptic vesicle release site [48, 51], it is thought that its interactions with AMPAR through TARPs may be sufficient for this nanoscale organisation to arise [52]. Other proteins, such as LRRTM2 [53, 54], neurexin and neuroligin [55], have also been proposed to also contribute to the clustering and alignment of AMPAR nanodomains with the presynaptic neurotransmitter release machinery.

1.1.3 AMPAR functional cycle and role in synaptic transmission

AMPA receptors are responsible for mediating the majority of the fast excitatory synaptic transmission in the central nervous system. When the action potential at the presynaptic neuron reaches the axon terminal, an influx of calcium ions triggers the fusion of neurotransmitter-containing synaptic vesicles with the terminal membrane, which results in the release of the neurotransmitter (in this case, glutamate) into the tight space of the synaptic cleft (20–30 nm [56]). Once in the synaptic cleft, glutamate molecules can bind to AMPAR and other glutamate receptors located on the postsynaptic membrane. The rapid and precise response of AMPARs to the release of glutamate is facilitated by the spatial alignment of AMPAR nanodomains with the presynaptic neurotransmitter release sites in trans-synaptic nanocolumns [51]. Glutamate molecules that did not bind to receptors or have dissociated from them are cleared from the synaptic cleft by specialised excitatory amino acid transporter (EAAT) proteins [57] to maintain normal glutamatergic signalling and prevent cell death due to glutamate toxicity (excitotoxicity [58]); or diffuse out of the synaptic cleft [59].

Each AMPA receptor can bind up to four molecules of glutamate – one in each of its subunits' ligand-binding domain. Upon binding glutamate, the clamshell-like structure formed by the LBD's two lobes – D1 and D2 – closes around the ligand molecule as the D2 lobe rotates up towards the D1 lobe by about 20° [60] (Figure 1.3 A). The energy of this conformational change is transferred to the transmembrane domains through the flexible LBD-TMD linkers, which pull the pore-lining M3 helices apart (Figure 1.3 B). This causes the opening of the transmembrane pore, allowing the flow of ions into the postsynaptic neuron, which can lead to the generation of action potential if the ion influx reaches the threshold level.

AMPARs can open to four conductance states which can be observed in single-channel recordings [61, 62, 63]. While it may be tempting to draw a conclusion that reaching each conductance level is the result of one subunit's LBD binding a molecule of glutamate, evidence from functional [64, 65] and structural studies [66] suggests that the relationship between agonist binding and conductance states is more complex. The binding of at least two molecules of glutamate has been found to be required for the opening of the channel to the lowest conducting state [64] and sufficient for its opening to the highest conductance [66], while the full occupancy of the agonist binding sites by glutamate does not always result in the opening of the channel to the full extent [66].

The return of the transmembrane pore to the closed state occurs either via deactivation, caused by the dissociation of glutamate from its binding site and opening of the LBD clamshell; or via desensitization, whereby the interface between D1 lobes of neighbouring LBDs within LBD dimers ruptures and the transmembrane channel closes despite glutamate remaining bound to the receptor [67, 68, 69] (Figure 1.3 B).

The functional properties of AMPAR – activation, deactivation, desensitization, and con-

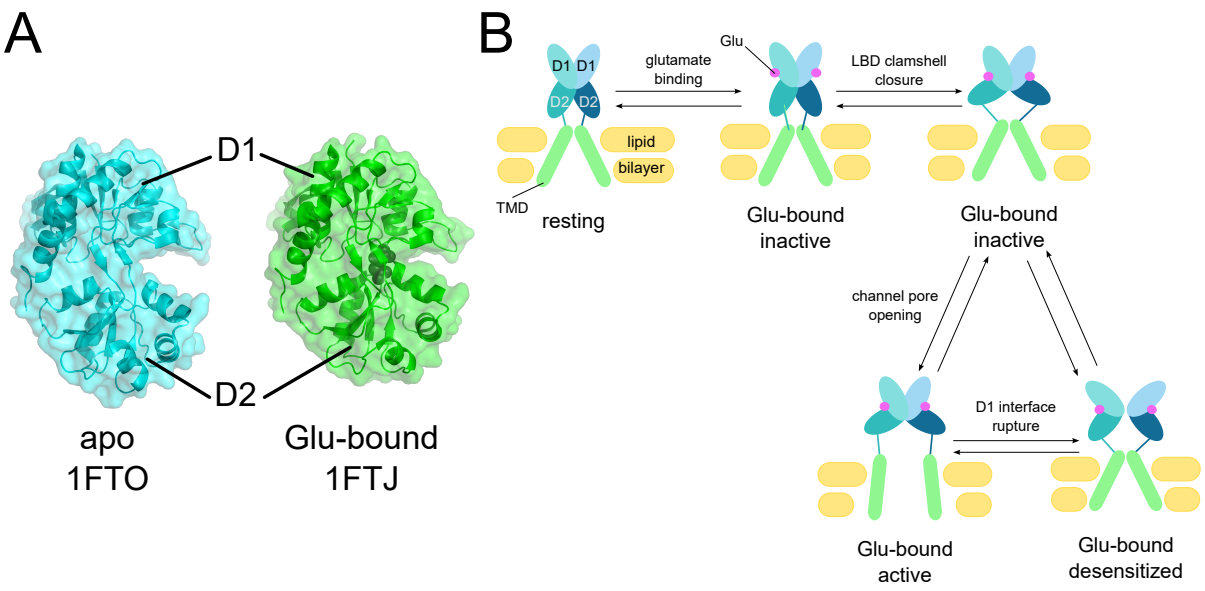

Figure 1.3: AMPARs open in response to binding glutamate. A. Structures of the LBD clamshell in *apo* state (1FTO [60]) and with glutamate bound (1FTJ [60]) B. The AMPAR functional cycle (ATDs omitted for clarity). The binding of glutamate causes a closure of the LBD clamshells, which in turn results in the opening of the ion channel pore composed of the receptor's transmembrane domains. The rupture of the D1 lobe interface triggers the closure of the transmembrane pore despite glutamate still being bound at the agonist binding site within the LBD clamshells.

ductance – are affected by the receptor's subunit composition and the presence and identity of associated auxiliary subunits, as mentioned in Section 1.1.2.

1.1.4 AMPAR trafficking and role in synaptic plasticity

Synaptic plasticity describes modifications in the synaptic strength or efficacy in response to the stimulation of the synapse. The synaptic response can be enhanced (facilitation/potentiation) or dampened (depression) on a short-term or long-term timescale, resulting in multiple forms of synaptic plasticity. While short-term synaptic plasticity is thought to contribute to short-lasting forms of memory and processing of sensory information [70], long-term forms of synaptic plasticity are believed to be the molecular mechanism behind learning and memory formation [71, 72, 73].

Synaptic plasticity can be expressed via changes at the pre-synaptic (adjustment of neurotransmitter release [74]) or post-synaptic neuron (adjustment in the number and/or nanoscale organisation of synaptic AMPARs). During long-term potentiation, NMDAR receptors act as molecular detectors of concurrent pre- and postsynaptic activity (glutamate released from the presynaptic terminal and depolarization of the postsynaptic membrane [75, 76]) and their activation allows cations, including Ca^{2+} to enter the postsynaptic neuron [77, 78]. The influx of calcium ions leads to the activation of cytoplasmic CaMKII (calcium/calmodulin-dependent

kinase II), which phosphorylates AMPAR GluA1 subunits [79], as well as stargazin (TARP-γ2) [80]. These phosphorylation events cause an increase in conductance through the GluA1-containing AMPAR channels [81, 82] and promote AMPAR trafficking to the synapse [80] and the anchoring of stargazin-associated AMPARs at the PSD through their association with PSD-95 [46]. The postsynaptic membrane is rendered more sensitive to the release of glutamate from the presynaptic active zone [83] via recruitment of additional AMPA receptors to the synapse [84], which can be accompanied by the adjustment of the functional properties of synaptic AMPARs [21, 85]; improved alignment of the AMPAR nanodomains with presynaptic neurotransmitter vesicle release sites [86, 87], or increased AMPAR density inside receptor nanoclusters [88] (though it is thought to be an unlikely mechanism due to the density of AMPAR at nanodomains already likely being close to its maximum [89]). The opposite is achieved in the process of long-term depression (LTD), associated with a decrease in synaptic AMPAR numbers resulting from their internalisation [90].

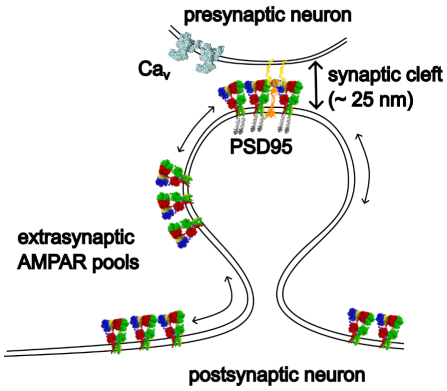

Figure 1.4: AMPAR at the synapse. AMPA receptors are exchanged between the intracellular receptor pools (not shown) and the cell membrane (at extrasynaptic sites) via endo- and exocytosis. The movement of receptors between extrasynaptic and synaptic sites (indicated by arrows) occurs via lateral diffusion. AMPARs then become stabilised at the PSD via TARP-mediated interactions with PSD-95 and other scaffold proteins. Adapted from [91].

The plasticity-related changes in receptor numbers, as well as the maintenance of receptor number at equilibrium conditions are achieved by the cycling of AMPARs between intracellular receptor pools, extrasynaptic sites on the plasma membrane, and synaptic sites [92] (Figure 1.4). The trafficking of receptors between these AMPAR populations happens via endo- and exocytosis (between intracellular receptor pool and extrasynaptic sites) and via lateral diffusion (between extrasynaptic and synaptic sites and between/within synaptic sites) [93, 94, 95, 96]. AMPARs within synaptic nanodomains are spatially ”trapped”, i.e. confined to the nanoclusters, via direct (through the AMPAR CTD) or indirect (through TARPs) interactions with scaffold proteins in the PSD [97], but can be freed from this anchoring by for example becoming

desensitized in response to binding glutamate [98]. The conformational changes associated with the process of desensitization might lead to a partial loss of the interaction of AMPAR with stargazin and thus to an increase in synaptic AMPAR mobility [98]. Alternatively, the rearrangements of the extracellular domains of the receptor – ATDs and LBDs – upon desensitization [99, 100] may lead to loss of interactions with AMPAR-interacting synaptic and presynaptic proteins which contribute to the anchoring of AMPAR at the synapse [24, 101, 83], as increasing the conformational mobility of the AMPAR ATD layer by destabilising the GluA2 B/D subunit ATD interface has been found to affect the synaptic insertion and mobility of AMPARs [34, 102].

1.1.5 Relevance in human disease

Due to AMPARs' ubiquity across excitatory synapses and their role in synaptic transmission and plasticity, they are essential for normal functioning of the central nervous system. It is therefore no surprise that dysregulation of AMPAR function and/or regulation is commonly found in patients with various neurological diseases, such as Alzheimer's disease (AD) [103], epilepsies [104, 105, 106], and intellectual disability [107, 106, 108, 109]. *GRIA3* has been identified as a candidate for X-linked intellectual disability [108, 110, 111, 112] as it is located on the X chromosome [113].

The first disease-associated *GRIA* variant was reported in 2007 [111] and since then, the genome-wide sequencing of healthy individuals and patients has revealed a multitude of genetic variations in all of the *GRIA1–4* genes, many of which were found to be disease-associated [6]. *GRIA1–4* genes are relatively intolerant to mutation compared to other protein-coding human genes, evidenced by their presence in the low residual variation intolerance percentiles (6, 13, 45, and 7% for *GRIA1*, *2*, *3*, and *4*, respectively) [114]. Mutation-intolerant hotspots identified in GluA1–4 using MTR (missense tolerance ratio) [115] or 3DMTR (three-dimensional missense tolerance ratio) analysis [116] have been found in regions known to have critical roles in the function of the receptor [106, 109, 117], e.g. the M1 and M4 helices in the TMDs, which are the site of the receptor's interaction with auxiliary subunits such as TARPs and CNIHs; around the agonist binding site within the LBDs [106], in the hinge region which connects the LBD's D1 and D2 lobes [109], or in the LBD-TMD linkers [117]. Interestingly, another intolerant patch of residues is present at the top of the GluA1–3 amino-terminal domain, pointing at the importance of this portion of the receptor, perhaps through its involvement in protein-protein interactions at the synaptic cleft [106]. *De novo* variants present in patients with neurological diseases localise to regions with lower missense tolerance scores than those present in the healthy general population, suggesting that missense tolerance analysis may be a useful tool in predicting potential pathogenicity for *GRIA* mutations [106, 109, 117].

The disease-associated *GRIA* variants exhibit a range of effects on the function of AMPARs

– both loss-of-function and gain-of-function phenotypes, as well as functionally neutral variants have been identified in patients [106, 109, 117], with some variants displaying a mix of gain- and loss-of-function effects on different functional characteristics [117] contributing to the overall effect. A functional study of *GRIA3* variants harboured by patients with neurodevelopmental disorders revealed that there is an association between the observed functional phenotype and reported clinical features, in which gain-of-function variants are associated with more severe outcomes than loss-of-function variants [117]. Understanding how the functional phenotype of a *GRIA* gene variant translates into the clinic is important for efficient diagnosis and appropriate choice of pharmacological intervention. Although only one AMPAR-targeting drug – perampanel [118], marketed as Fycompa ®– has so far been approved by the FDA, other modulators of AMPARs could also be explored as treatment options for patients.

1.2 Con-ikot-ikot toxin

1.2.1 Animal venom toxins as tools for studying ion channels

Venomous animals, such as snakes [119], scorpions [120], spiders [121], and cone snails [122], have evolved a variety of peptide toxins for the purposes of defence and/or capturing prey. Venoms are usually produced and stored in specialised venom glands and delivered into other organisms via envenomation apparatus such as fangs (snakes, spiders), stingers (scorpions), or harpoons (cone snails), and are highly complex mixtures of peptides with a wide range of pharmacological targets. Due to this, as well as their exquisite selectivity and high potency, animal venom toxins have been used as research tools and valuable drug leads [123] (e.g. conotoxin-based analgesic ziconotide [124, 125] or scorpion chlorotoxin, which is currently evaluated in clinical trials for glioblastoma [126, 127]). Key ion channel targets of animal venom toxins include voltage-gated sodium, potassium, and calcium channels, as well as acetylcholine receptors.

The growing availability of ion channel crystal structures has allowed researchers to employ homology modelling, docking, and molecular dynamics simulations to build models of ion channel-toxin complexes. Such models can then be used to understand the toxins' binding modes with the aim of improving their properties for research and/or therapeutic purposes. One example of this is the case of a sea anemone (*Stichodactyla helianthus*) toxin ShK. ShK is a potent inhibitor of K^+ channels [128], including $K_v1.3$ – an established target for treatment of autoimmune diseases [129]. However, it lacks selectivity for $K_v1.3$ against other K_v channels [130]. Modelling ShK's interactions with $K_v1.3$ and $K_v1.1$ channels (models built based on the $K_v1.2$ channel structure [131] by homology modelling) [132, 133] showed that a single mutation – K18A – despite reducing the potency of the toxin against $K_v1.3$ channel, gave it

124-fold selectivity for $K_v1.3$ over $K_v1.1$ [133] without the need to introduce unnatural amino acids or adducts to the toxin [130, 134]. Related work from the same group [135, 136] focused on HsTX1 toxin from the venom of a scorpion *Heterometrus spinnifer*, which also blocks K^+ channels [137] but displays high selectivity for $K_v1.3$ versus $K_v1.1$ [138]. The analyses revealed the structural mechanism behind the selectivity [135] and yielded an even more $K_v1.3$-selective HsTX1 analogue [136].

Toxins with various types of labels have been used in many ion channel research applications [139, 140, 141].

1.2.2 Conotoxins

Conotoxins are peptides present in the venom of ∼1000 species of marine cone snails [122] (Figure 1.5). Cone snails use their specialised harpoon delivery apparatus to inject venom into their prey – fish, worms, or molluscs – and immobilise it via the synergistic action of a cocktail of toxic peptides with a wide array of targets [142, 143, 144].

Figure 1.5: Shells of various *Conus* snail species (not to scale), adapted from [122].

Each *Conus* snail species produces a distinctive venom containing more than 100 different components, and it is estimated that overall, over 50 000 different active components can be found across the venoms of all cone snails [145]. These peptide toxins are relatively small

compared to toxins found in venoms of other animals and are translated from mRNA as peptide precursors. Conotoxin precursors share a common organisation of a highly conserved N-terminal signal peptide (responsible for targeting the precursor peptide), a propeptide (involved in the correct folding of the precursor and subsequently removed [146]), and highly divergent mature peptide, which is the secreted product [147] (Figure 1.6 A). Conotoxins are typically rich in cysteines and disulfide bonds, but can also contain no disulfide bonds. Historically, the "disulfide-poor" or "cysteine-poor" peptides (containing 0–1 disulfide bonds) were termed conopeptides, while the "disulfide-rich" or "cysteine-rich" peptides (containing 2 or more disulfide bonds) were called conotoxins; however, this distinction is now considered outdated and current literature uses the two terms interchangeably [145, 148].

Conotoxins can be classified in three ways, which reflect the development of methods used to identify them over time. Early conotoxin research efforts concentrated on isolating the toxins directly from the venom and gave rise to classifications based on the toxins' targets (pharmacological family, indicated with a Greek letter, e.g. ω-toxins target Ca^{2+} channels [144]) and arrangement of cysteine residues in their primary sequence (cysteine framework, indicated with a Roman numeral, e.g. conotoxins with cysteines arranged as CC-C-C are grouped under cysteine framework I). The third, most recent classification method is based on the identity of the signal peptide sequence (gene superfamily, indicated with a Latin letter) [147, 145].

Like other animal venom toxins, conotoxins have been used as research tools and drug leads due to their wide range of pharmacological targets and high specificity. Most notably, ω-conotoxin MVIIA, isolated in 1982 from the venom of *Conus magus* [149], which targets the $Ca_v2.2$ channel, has been developed into the only, so far, FDA-approved conotoxin-based drug, potent [124, 125] analgesic ziconotide (marketed as Prialt ®).

1.2.3 Con-ikot-ikot toxin

Con-ikot-ikot (CII) is a conotoxin found in the venom of a predatory marine cone snail *Conus striatus* (Figure 1.6 A) [150]. Its unique name comes from a Filipino word "ikot-ikot" – meaning "spinning around" or "turning around" – which describes the behaviour of fish following injection with the toxin [150]. The toxin exists as a ∼20 kDa homodimeric complex [151], contrary to the initial suggestions that it is a dimer of dimers [150]. Each of its subunits consists of 86 amino acid residues arranged into a four-helical bundle and contains 5 intra-subunit disulfide bonds, which, together with 3 disulfide bonds formed between the two subunits, give con-ikot-ikot a stable and rigid structure [151] (Figure 1.6 C–E). Both the size and dimeric structure of CII are unusual amongst conotoxins, though other conotoxins that share those features have been identified [152, 153, 154, 155, 156].

Con-ikot-ikot has been found to bind specifically to AMPA receptors (homomers of any subunit type – GluA1–4 – as well as native AMPARs, likely heteromeric) and modify their

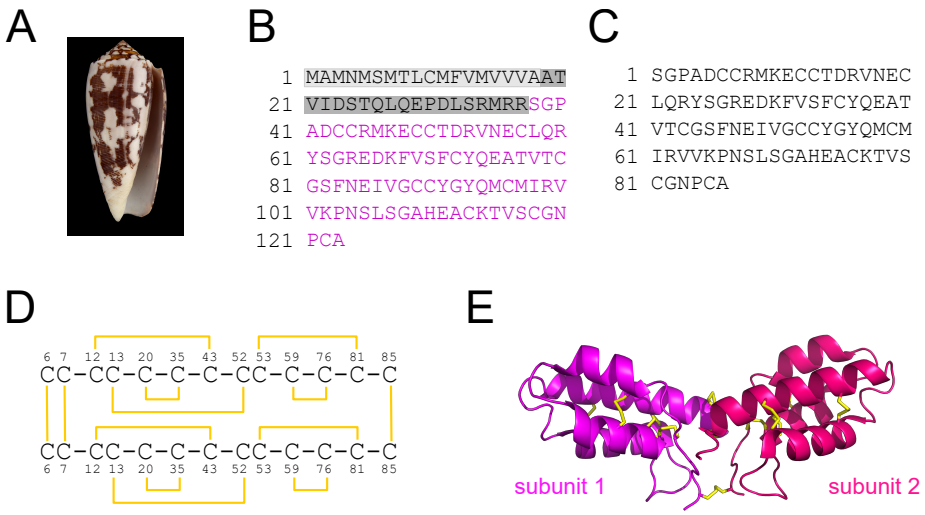

Figure 1.6: Con-ikot-ikot toxin. A. *Conus striatus* shell image [157]. B. Full sequence of CII precursor peptide [150]. Light grey box, signal sequence. Dark grey box, propeptide. Magenta text, mature peptide sequence. C. Mature CII peptide sequence and residue numbering. D. Cysteine framework and disulfide bond network in CII. E. Structure of CII. Subunits shown in magenta and hot pink, disulfide bonds shown in yellow sticks.

glutamate-gated currents by inhibiting AMPAR desensitization [150] (Figure 1.7 B) with an EC_{50} of 5 nM [63]. At the same time, it has been shown not to have an effect on the currents of other iGluRs – GluK2 kainate receptors and GluN1/GluN2A NMDA receptors – nor GABA-A receptors [150]. CII binds to AMPAR at a site distinct to that of other desensitization blockers, cyclothiazide (CTZ) and (R,R)-2B [150, 151]. While these compounds occupy a binding site located within individual LBD dimers, CII is nestled in the solvent-filled cavity between the receptor's LBD and ATD layers, participating in interactions with the LBDs of all four AMPAR subunits [151]. This unique binding mode allows the toxin to stabilize the entire AMPAR LBD layer in a conformation characterised by a considerable increase in the distances between the A/C and B/D pairs of LBD subunits, as compared to their conformation in the inactive state. The distances measured between Cα atoms of R660 of the A/C subunit pair and Q756 of the B/D subunit pair increase from 16.5 to 27.4 Å between B/D subunits, and from 19.7 to 22.0 Å between A/C subunits. Stabilising this conformation prevents the rupture of the LBD dimer interface [151], thus blocking AMPAR desensitization [67].

Based on the crystal structure of the GluA2 AMPAR-CII complex (Figure 1.7 A), CII has been described as making few contacts with the ATD layer of AMPAR. However, three CII residues were highlighted as forming crucial interactions with the LBD layer of AMPAR: Q37, E48, and A86 (Figure 1.7 C–E). The AMPAR residues that form contacts with those three CII amino acids (R453, R660, and K752, respectively) have been found to be conserved between AMPA receptor subtypes, but not in kainate receptors or NMDA receptors. The importance of

the highlighted interactions was confirmed in AMPAR mutagenesis experiments, where GluA2 residues listed above were mutated to corresponding residues from kainate receptors (R453Q, R660K, and K752Q). Each of the introduced mutations lowered the effect of CII on the mutated GluA2 AMPAR, and when R453Q and K752Q were introduced simultaneously, the effect of the toxin was abolished [151].

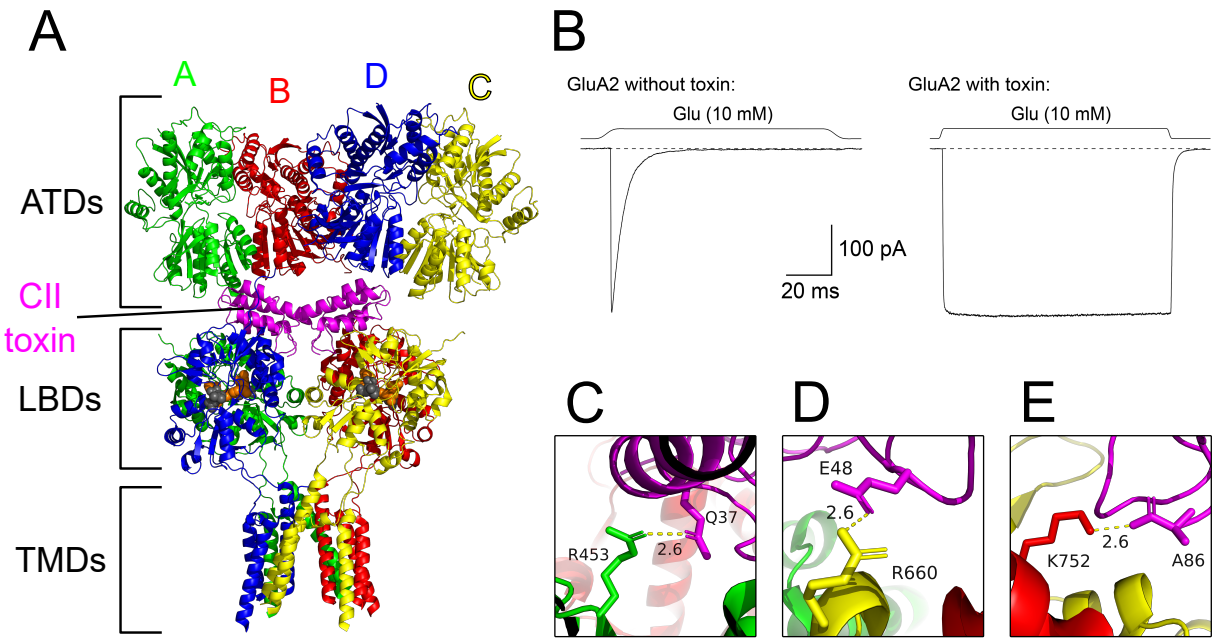

Figure 1.7: A. Crystal structure of GluA2 AMPAR in complex with CII, partial agonist kainate (grey spheres), and positive modulator (R,R)-2B (orange spheres) PDB ID: 4U5D [151]. B. CII blocks AMPAR desensitization. Adapted from [63]. C, D, E. Close-up view of the interactions between CII toxin and AMPAR LBDs: CII Q37 with AMPAR A/C subunit R453, CII E48 with AMPAR A/C subunit R660, and CII A86 with AMPAR B/D subunit K752, respectively.

1.2.4 Con-ikot-ikot as a tool for studying AMPA receptors

Con-ikot-ikot is an excellent candidate for the development of tools for studying AMPA receptors. Firstly, it is highly specific for AMPAR versus other ionotropic glutamate receptor types [150] and binds tightly to the receptor, taking minutes to wash out [63]. The 1:1 binding stoichiometry between AMPAR and CII [151] means that there is no risk of cross-linking, which is a common problem when using immunolabelling [95, 96]. This, together with the fact that CII binding to AMPAR causes minimal perturbation to the receptor's size (about 1 nm increase in how far the receptor extends into the synaptic cleft [151]) and does not introduce any bulk on the surface of the receptor (due to binding within the receptor's structure), suggests that CII-tagged AMPAR could move in and out of the synaptic cleft with little steric hindrance compared to

receptors bound to bulky probes like antibodies/large quantum dots [158] or genetically fused with fluorescent proteins or self-labelling tags.

The unique positioning of the CII binding site would also be advantageous in super-resolution imaging applications due to the resulting minimal linkage error (distance between the source of fluorescence and the target protein). In contrast, labelling strategies based on antibodies (primary only or primary + secondary), nanobodies, or genetic fusions necessarily introduce a larger linkage error, ranging between 10–20 nm for antibodies [159], 2.5–4 nm for nanobodies [160], and 3–5 nm for genetic fusion approaches [161].

The location of toxin binding site within the extracellular portion of the receptor means that even with the toxin bound, the surface of the extracellular domains of the receptor remains unobstructed and available for physiological interaction partners to bind to. This is important as we are increasingly more aware of the confirmed and potential synaptic AMPAR interactors [101], which may play an important role in contributing to the nanoscale organisation of the synapse.

Another aspect that makes CII attractive as an AMPAR probe is the fact that its crystal structure alone as well as in complex with the receptor has already been solved [151]. As membrane proteins are difficult targets for crystallography [162], many research efforts focused on ion channel complexes with toxins rely on homology modelling or the use of structure prediction software such as AlphaFold [133, 136, 163, 164]. In contrast, the availability of crystal structures of CII and AMPAR in complex with CII presents an opportunity to draw from the knowledge of their structure and interactions to selectively modify CII properties to better suit particular research needs.

One of such needs that could be addressed by learning more about CII toxin's interactions with AMPAR is the lack of probes with the ability to target specific AMPAR subunit combinations. Different AMPAR types have different functional properties [16, 17] and are differentially expressed in different areas of the central nervous system at different times [10, 12]. Selectively targeting specific AMPAR subunit combinations would be of great interest to the field as it would bring better understanding of the distribution and functional characteristics of different subunit compositions, but also because of the potential for subunit composition-specific modulators that could be used to treat AMPAR-related diseases [165]. As CII binds in the space between the amino-terminal and ligand-binding domains of the AMPA receptor, understanding its interactions with the ATDs could allow us to target this domain layer as the ATDs show high sequence diversity among GluA1–4 subunits (Figure 1.8).

Another way in which a more detailed understanding of the AMPAR-CII interactions could guide the development of CII into an AMPAR-specific probe could be by targeting toxin residues which confer its desensitization-blocking properties to produce a variant of the toxin that would still bind to the receptor without impairing its function, as functional states have been found to

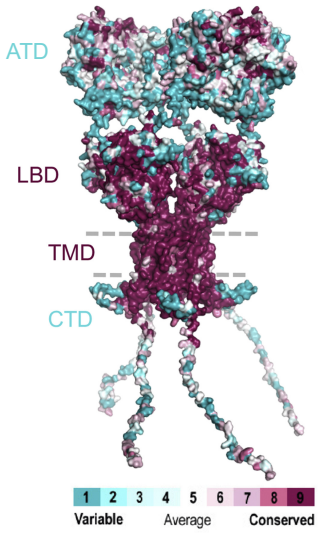

Figure 1.8: Sequence diversity between GluA1–4 subunits. Adapted from [166].

affect the receptors' movements in and out of synapses [98]. Tracking movements of AMPARs while blocking their desensitization with the toxin could also be useful for replicating this finding with a different experimental design, providing additional evidence for functional signals regulating synaptic AMPARs' mobility.

Understanding the interactions between con-ikot-ikot and AMPAR in detail could also be used to design new peptides [167, 168] that would target the receptor in a similar way as the toxin and could be manufactured chemically instead of having to be expressed in bacteria and purified from lysate. The purification of CII is expensive and time-consuming, and the purified protein yield is consistently low [151, 63], but due to its large size (86 amino acid residues per subunit) as well as numerous disulfide bonds, it cannot easily be synthesised chemically [169].

Beyond understanding the interactions between AMPAR and CII and using this knowledge to tune the toxin's properties in relation to AMPAR, several aspects of toxin expression, purification, and fluorescent labelling could be improved upon. Firstly, the original protocol for protein expression that was used for producing the toxin by us and others [151] involves the use of relatively slow-growing ORIGAMI *E. coli*, which puts the timeframe for one full expression-purification round at about one week. Optimising the protocol to use a faster-growing bacterial strain could accelerate the process and additionally could increase the very low yield of protein. We decided to incorporate in our protocol an additional plasmid carrying genes responsible for facilitating the formation and shuffling of disulfide bonds (see Section 1.5), which meant we could use the BL21 (DE3) *E. coli* strain in our experiments.

Additionally, using the knowledge from simulations and their analysis, we could design toxin mutants that would give us additional control over how many and which sites on the protein become fluorescently labelled. This, as well as determining an efficient way to remove unbound dye from the reaction mixture without significant protein loss, could be important

practical improvements to the realistic and practical potential of CII as a fluorescent AMPAR-specific probe.

1.3 Molecular Dynamics simulations

Molecular dynamics (MD) simulations are a powerful computational tool for studying processes involving molecules of biological relevance, such as nucleic acids or proteins, at an atomic scale. In MD simulations, Newton's equations of motion are integrated to predict the positions of all atoms in a simulated system over time, given their initial positions and a model of physical forces that act upon the system. The interactions between atoms are captured in a functional form in molecular mechanics force fields [170, 171, 172, 173, 174], which include terms describing the covalent (bond stretching, angle bending, dihedral angles, and out-of-plane geometry) interactions, as well as non-covalent (non-polar and electrostatic) interactions. User-defined forces acting on the system can also be added to the simulation (resulting in so-called steered molecular dynamics simulations) [175].

Since the first research article employing molecular dynamics simulations in a biological context was published in 1977 [176], the development in computer hardware and molecular dynamics software [177, 178, 179, 180, 181] have made MD simulations more accessible to scientists interested in tracking the trajectories of various molecular systems [182, 183, 184]. MD simulations offer insight into different levels of physical detail over timescales ranging from hundreds of femtoseconds in methods with higher degree of accuracy and physical detail to milliseconds in coarse-grained simulations with particles representing groups of atoms. The accessibility of X-ray crystallography, Cryo-EM, and NMR structures of many proteins in the Protein Data Bank (PDB) [185] also means that the mechanisms of action of many systems can be investigated this way to gain the level of understanding that may never have been available before.

MD simulations can quickly generate vast amounts of data in the form of three-dimensional coordinate trajectories of all atoms over a large number of steps, as well as additional associated information collected over the course of the simulation, such as temperature, potential energy, periodic box volume, and system density; the analysis of the obtained data can therefore be a complex and difficult process. While standard, traditional trajectory analysis tools, such as root square mean deviation (RMSD) or root square mean fluctuation (RMSF) provide valuable insights into the simulation, there are many more complex aspects of the simulated system's behaviour which can be investigated based on the trajectories. One of such aspects is the dynamic profile of interactions between protein binding partners, which cannot be inferred from a static structure.

1.3.1 MD simulations of AMPARs

Molecular dynamics simulations have been used to investigate AMPA receptors for almost a quarter of a century. The first high-resolution structure of the isolated ligand-binding core of a GluA2 AMPA receptor (in complex with kainate) was published in 1998 [186] and was followed by a number of other structures of the AMPAR LBDs in the apo state [60] or bound to a variety of agonists, such as glutamate, kainate, or AMPA; and antagonists, such as CNQX or DNQX [60, 187, 188, 189]. The availability of these crystal structures allowed simulation-based investigations to explore the conformational changes of the LBD upon ligand binding and form ideas about the mechanism through which they happen as well as their implications for channel gating [190, 191, 192, 193, 194]. In a number of studies, point mutations were computationally introduced to simulated LBD models in order to better understand the role of specific AMPAR residues in stabilising LBD clamshell conformations and dimer interfaces or in the receptor's interactions with binders [195, 196, 197, 193, 194]. The binding modes of different ligands could be investigated and compared [190, 191, 196, 198].

After the first full-length AMPA receptor structure [9] was solved, molecular dynamics simulations studies of AMPARs could extend the simulated system to portions of the receptor other than the ligand-binding domains. Including the transmembrane domains in the simulated system enabled insights into the mechanism of receptor activation and desensitization from targeted MD simulations where the ligand-binding domains were forced to move between the antagonist-bound to agonist-bound conformation [199]. The availability of full-length AMPAR structures has made it possible to perform computational electrophysiology studies on the transmembrane regions of the receptor to examine their ion permeation properties [200, 66, 201]. More recently, MD simulations have also been employed to study the elusive conformational dynamics of the amino-terminal domain layer of AMPARs [102, 202], bringing new insights to our understanding of this portion of the receptor.

1.4 Residue interaction network analysis

Networks (also referred to as graphs) are mathematical structures consisting of a set of nodes connected by edges, and can be used to represent various objects or entities (nodes) as well as interactions between them (edges). Examples of contexts in which networks can be used include social networks, food webs in ecology, etc.

Networks can also be used to represent interactions between proteins at different scales. Taking proteins as nodes and interactions between them as edges, we obtain a network of protein–protein interactions and can identify interacting partners or groups of interacting proteins [203, 204]. At a different scale, taking individual residues within interacting proteins as nodes, and their interactions as edges, we obtain a residue interaction network (RIN), which

can be used as an intuitive method to identify and investigate groups of interacting residues. While investigating static networks [205, 206] can shed some light on the main interactions within a protein or a protein complex, the generation of vast amounts data from MD simulations presents an opportunity to include multiple structures in the analysis, thus taking into account the dynamic nature of protein complexes and allowing insights into the relevance of interactions present in one frame in the larger context of a structural ensemble.

1.4.1 Distance-based approaches

A number of available RIN analysis tools construct residue interaction networks based solely on the distance between amino acid residues, computed as distances between C_α atoms [207, 208, 209, 210, 211, 212], C_β atoms [209, 210, 211], heavy atoms [210, 211], or any atoms in the residues [210, 211]; or other, user-defined atom selections [211] The more coarse-grained approaches, which consider only C_α or C_β atoms, are not as computationally intensive as the more fine-grained methods (like those considering heavy atoms or all atoms in the residue). While these approaches allow a good representation of the topology of the protein and can be useful in understanding the protein dynamics, they lack the insight into the types of interactions which are present in the system.

1.4.2 Energy-based approaches

Some of the other tools use residue interaction energy networks instead [209, 213, 214]. Though this approach provides quantitative information about the interactions present in the system, similarly as above, the interaction types are not considered as part of the analysis. Moreover, it is computationally intensive and the computation of interaction energies may require the use of simulation program that was used to produce the trajectory, which can be limiting [213, 214].

The tools in this category are either unavailable [213], or have not been updated since publication several years ago [209, 214].

1.4.3 Approaches considering interaction type

Other tools explicitly consider various non-covalent interaction types that residues can participate in, such as hydrogen bonds and salt bridges [212, 215, 216]. The tools define interactions based on the geometric and physico-chemical characteristics of amino acid residues in the simulated system and compute a network of interactions for each frame of the MD simulation trajectory. The published (but unavailable) version of RIP-MD [212] seems to be better suited to the analysis of selected residues in the context of specific interactions they participate in or the relative numbers of interactions of different types that are present in various sections of the

trajectory. The latest version of the program, not published in scientific literature, is available at https://github.com/Cold7/RIP-MD3.

Rinmaker [215] can process MD simulation trajectories and output a collection of networks – one for each frame of the MD trajectory – but does not offer any tools for their subsequent analysis.

RING 4.0 [216] provides a powerful opportunity to engage with the generated networks in a more exploratory fashion and the latest version has been published earlier this year, two years after the previous update came out [217].

1.4.3.1 RING

RING 3.0 (Residue Interaction Network Generator) [217], the version of the RING software [218, 219, 217, 216] which I use as the source of network data in my analysis approach, has incorporated the ability to process multi-state structures (NMR structural ensembles and MD simulation trajectory files) into its functionality (the previous version of the program could only be used for a single model at a time). Taking into account the geometry and physico-chemical characteristics of amino acids residues in the simulated system, RING 3.0 computes a network of interactions with six different interactions types (hydrogen bonds, van der Waals forces, ionic interactions, π-cation interactions, π-π stacking, and disulfide bridges), for each frame of the input trajectory. Using the web server of RING 3.0, the user can investigate an interactive visualisation of the probabilistic network generated from the overall trajectory data, where the weights of edges (in the range of 0–1) represent the frequency at which a given edge occurs in the trajectory.

The user can also filter edge types (by interaction type, as well as intra-chain vs inter-chain) and select any node on the interactive graph to highlight the corresponding residue on the 3D visualisation of the model structure, and vice versa. Moreover, a ”conformational dependent contact map” is also available for inspection and analysis, showing the types of contacts each of the residues in the system is involved in along the time axis of the trajectory, grouped by contact type. By investigating the probabilistic network, the user can identify both very dynamic as well as highly conserved contacts and map them onto the structure.

A new, updated version of RING – RING 4.0 [216] – has been published earlier this year with the main improvements relating to the variety of chemical compounds it is able to process (over 35 000 molecules available in the PDB chemical component library), extending the types of interactions it is able to detect (π-hydrogen bonds, halogen bonds, metal ion coordination), and refined definitions of interaction types included previously, as well as improving time of execution.

1.5 The csCyDisCo system for cytoplasmic expression of conotoxins

Like other conotoxins, con-ikot-ikot contains multiple disulfide bonds (13 in total – 3 inter-subunit and 5 intra-subunit disulfide bonds in each subunit; Figure 1.6). This property gives rise to its stable, rigid structure, but also makes it challenging to produce as disulfide bond formation requires targeting the protein of interest to cellular compartments specialised for this purpose – the endoplasmic reticulum in eukaryotes and the periplasm in prokaryotes – which contain appropriate catalysts for disulfide bond formation and isomerisation. Producing disulfide bond-containing proteins in the cytoplasm is possible and has initially been achieved by producing *E. coli* strains with disrupted disulfide bond reducing pathways in the cytoplasm [220, 221, 222]. However, the yields produced using them are often low as they do not contain a catalyst of *de novo* bond formation.

The CyDisCo (Cytoplasmic Disulfide bond formation in *E. coli*) system was developed to facilitate the formation and isomerisation of disulfide bonds in the *E. coli* cytoplasm [223] by introducing a sulfhydryl oxidase Erv1p from yeast, as well as a disulfide isomerase from either bacteria (DscB) or human (hPDI) on a single plasmid vector. This was shown to allow high level expression of proteins containing disulfide bonds [223].

The original CyDisCo system has since been expanded for use in expression of cone snail toxins by the addition of a conotoxin-specific protein disulfide isomerase to produce the csCyDisCo (conotoxin-specific CyDisCo) system [224]. A comparison of expression of three conotoxins – H-Vc7.2 [224], Conk-S3 [225], and Mu8.1 [155] – with or without the csCyDisCo system plasmid revealed that in the presence of csCyDisCo, a larger proportion of the expressed target protein was found in the soluble fraction.

1.6 Aims of the project

The aim of this project was to use a data-driven approach to characterise the interactions between AMPA receptor and con-ikot-ikot conotoxin in order to inform downstream investigations of con-ikot-ikot as an AMPAR-specific molecular probe.

To achieve this, I produced a dataset of molecular dynamics simulations of the AMPA-CII complex and developed a new residue interaction network analysis for MD simulation trajectories. I used this new network analysis method to analyse the MD simulation trajectories and carried out experimental validation of the results of computational analyses.

Chapter 2

Methods

2.1 Computational methods

2.1.1 Molecular Dynamics simulations

2.1.1.1 Building the simulated systems

AMPAR GluA2 homotetramer in complex with glutamate and WT CII

The simulated model of the the extracellular portion of the homomeric GluA2 AMPAR (ATDs, ATD–LBD linkers and LBDs) in complex with four glutamate ions and wild-type CII was built by me based on an earlier LBD-Glu-CII model (Figure 2.1 A).

The LBD-Glu-CII model was built by superimposing four copies of the 1FTJ [60] crystal structure (isolated GluA2 ligand-binding domain in complex with glutamate) on the AMPAR ligand-binding domains in the 4U5C [151] structure (full-length GluA2 homotetramer (with truncated CTDs) in complex with CII toxin, partial agonist FW, and positive modulator (R,R)-2B) and copying the position of CII toxin from 4U5C. Missing residues and atoms were modelled in using PDB-Fixer [226] and the N- and C-termini of the AMPAR portion of the system were capped with acetyl (ACE) or *N*-methyl amide (NME) caps, respectively, in order to avoid generating artificial interactions with charged terminal residues where they would not be present in a full-length AMPAR.

The ATD-LBD-Glu-CII model (Figure 2.1 B) was based on the 4U5D [151] structure (full-length GluA2 homotetramer in complex with CII toxin, partial agonist KA, and positive modulator (R,R)-2B) instead (Figure 2.1 C). Side chains which were not resolved in the 4U5D structure were modelled in manually using the ”Mutagenesis wizard” tool in PyMOL based on the side chain conformations in related structures (PDB ID 4U5C [151], 3KG2 [9], and 5VHY [227]) if the side chain of interest was present and would not introduce clashes if copied over to the 4U5D-based structure; or based on the lowest energy score in the ”Mutagenesis wizard” tool otherwise.

The linkers connecting amino-terminal and ligand-binding domains were not resolved in the 4U5D structure (Figure 2.1 C) and were modelled in manually using the PyMOL Build tool. The amino acid sequence of the linker region in the construct used to obtain the crystal structure was 2 residues shorter than the full-length linker [151]. The two residues (L383 and P384) were also manually modelled in at their correct place in the sequence. The sources of all residues in the ATD-LBD-Glu-CII model can be found in Appendix B.

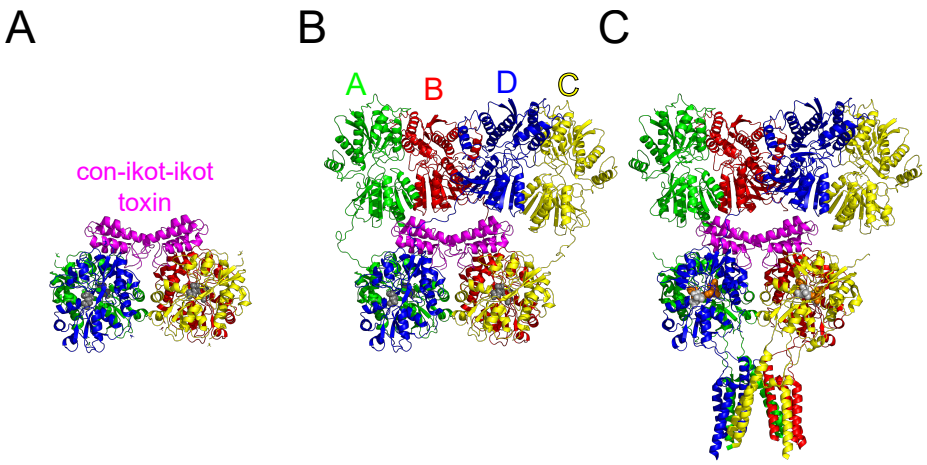

Figure 2.1: A. Simulated system – AMPAR LBDs in complex with CII and glutamate (dark grey spheres) B. Simulated system – AMPAR extracellular domains in complex with CII and glutamate (dark grey spheres) C. 4U5D [151] – crystal structure of full-length AMPAR (with truncated CTDs) in complex with CII toxin, partial agonist kainate (grey spheres), and positive modulator *N*,*N*'-[biphenyl-4,4'-diyldi(2*R*)propane-2,1-diyl]dipropane-2-sulfonamide (orange spheres). Note that the ATD-LBD linkers are not resolved in this structure.

Con-ikot-ikot toxin lysine mutants

Structures of all proposed con-ikot-ikot lysine mutants (K10A K30A K77A, K10R K30R K77R, K10A K30A K65A K77A, and K10R K30R K65R K77R) were created by mutating appropriate residues using the PyMOL Mutagenesis Wizard tool.

Fluorescent dye – PA-JF 549

As we are interested in investigating the dynamics of a system including a fluorescent dye, it was important to be able to include the dye in our MD simulations. The approach I used to do this was treating the dye as a ligand separate from the rest of the system, and creating the covalent bond between the amino acid and the dye at the level of system preparation in tLEaP, which allowed me to take advantage of the torsion angle bias terms included in the force field that result in a more accurate backbone parameters for amino acids [172].

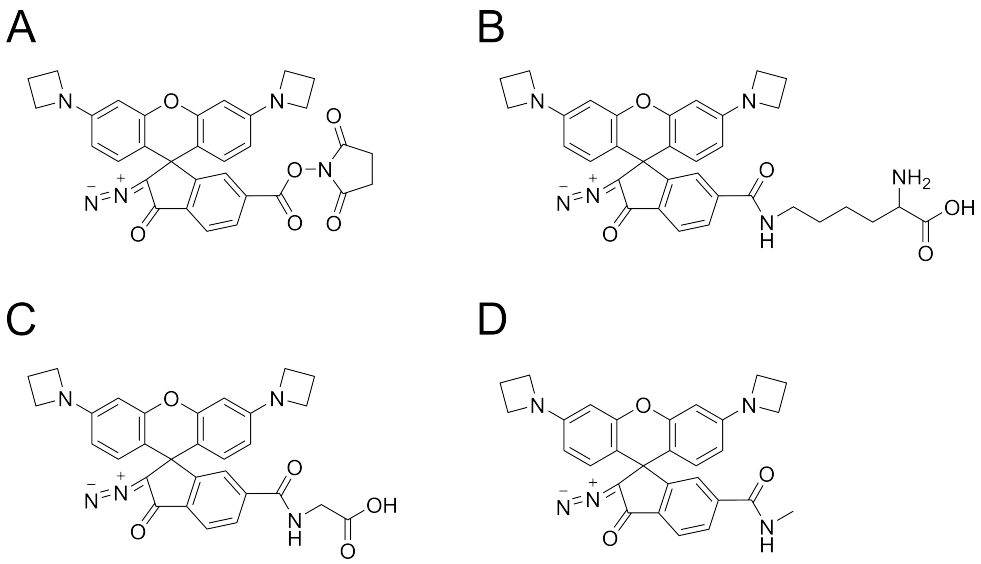

Figure 2.2: A. Photoactivatable Janelia Fluor 549 fluorescent dye (PA-JF 549) [229]. B. PA-JF 549 bound to the side chain amine group of a lysine residue. C. PA-JF 549 bound to the amine group of a glycine residue. D. Modified structure of PA-JF 549 used to obtain partial charges.

This approach involved derivation of force field parameters for the dye molecule by itself (to be able to load it into the program used for preparation of simulation input files), as well as bound to the target amino acid – in this case, either lysine or glycine (Figure 2.2 A–C) – in order to be able to set the parameters of the ”bridge” formed by bonding the ligand (dye) and amino acid. The reason for this is that while the atoms coming from the protein (i.e. those belonging to the amino acid residues) have atom types specific for the protein force field ff14SB [172], the atoms coming from the dye molecule have GAFF2 [228] types assigned to them in the process of deriving force field parameters, and neither one of the force fields can produce parameters for bonds with a mix of the two atom types.

The protein system and appropriately placed molecule of dye were loaded into tLEaP, modified (some atoms need to be removed from the amino acid as well as the dye – Figure 2.3), and covalently bonded. Removing atoms from the amino acid and the dye molecule results in the removal of their partial charges from the system, which creates a charge imbalance. In order to minimise this effect, I slightly modified the structure of the dye (Figure 2.2 D) as it is loaded into tLEaP to limit the number of atoms that have to be removed. Even with this modification, some charge imbalance remained. In order to eliminate the remaining imbalance, I adjusted the partial charges of several atoms in the amino acid and dye according to the charges computed for the structure of amino-acid bound dye. The table of modified atoms, along with their assigned partial charges, can be found in Appendix C.

AMPAR GluA1/2 heterotetramer in complex with glutamate and CII

Native AMPA receptors exist in various arrangements of GluA1–4 subunits, from homote-

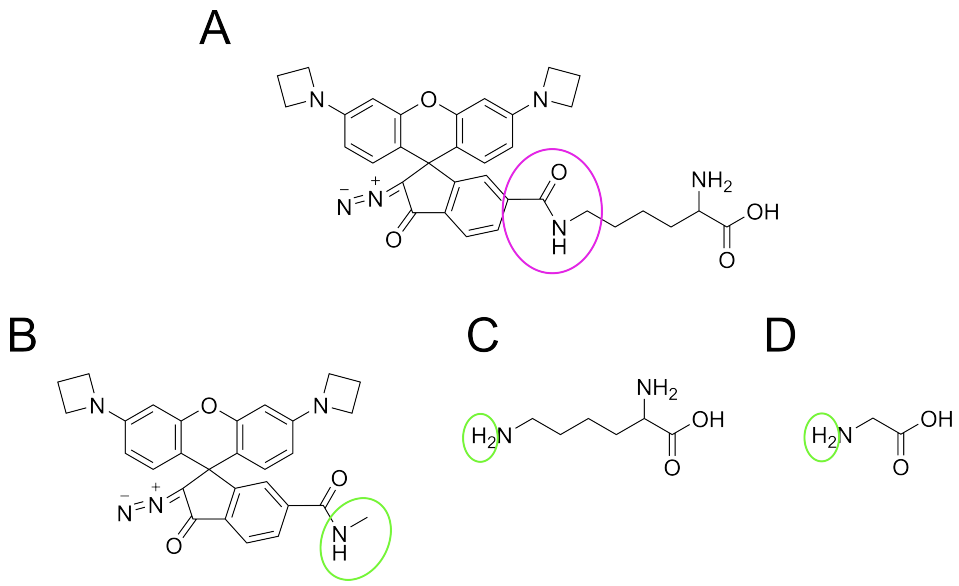

Figure 2.3: A. The area for which parameters will be missing following the process of attaching the dye to an amino acid residue in tLEaP, the same in the case of glycine and lysine (magenta circle). B, C, D. Groups of atoms removed in the process of attaching the fluorescent dye to the protein in tLEaP (green circles).

tramers (GluA2) to triheterotetramers (GluA1A2A3A2), with different variants expressed at different abundance (e.g. GluA2 homotetramers at about 1.1% and GluA1A2A3A2 at about 25% in the rat brain [20]) and exhibiting different functional and expression characteristics [10, 12, 13, 16, 17, 18, 19]. Selective targeting of specific subunit compositions of interest for fluorescent imaging or functional modulation is an active field of current research, but at the moment remains an unsolved problem.

The unusual positioning of the con-ikot-ikot binding site between the ATD and LBD layers of the AMPA receptor presents a unique opportunity to explore whether possible interactions between the toxin and the ATD layer of AMPAR can be harnessed to develop subunit composition-specific binders for AMPARs, as the ATDs are a domain that is highly variable between the four AMPAR subunit types.

We chose the starting point of our investigation to be a GluA1A2A1A2 diheterotetramer due to the relatively high percentage of native rat receptors of this subunit composition (24% [20]), as well as the fact that GluA1 and GluA2 subunit types share a high level of sequence identity and similarity (see Appendix D). Although GluA1A2A3A2 AMPARs represent a higher percentage of native rat AMPARs than GluA1A2A1A2, as identified in [20], they are composed of three AMPAR subunit types (GluA1, GluA2, and GluA3), which makes them a more complex system, more suitable as the subject of further analysis once basic inferences are made with a simpler model.

The GluA1A2A1A2 ATD-LBD-Glu-CII heterotetramer model was built based on the orig-

inal GluA2 homotetramer model, in which I manually converted subunits A and C from the GluA2 to GluA1 sequence in order to retain the overall shape of the homotetramer system and relative positions of the subunits around the binding site of CII, as all available crystal structures of AMPAR in complex with CII are of the GluA2 homotetramer [151].

I performed a sequence alignment of rat (*Rattus norvegicus*) GluA1 and GluA2 proteins (Appendix D) using the EMBOSS Needle pairwise sequence alignment tool [230] and based on this alignment modified the A and C subunits by removing 5 amino acid residues (a deletion of 1 residue – GluA2 S50 – and a 4 residue stretch – GluA2 N185–K188 – in each subunit) and substituting 194 amino acids in each of them. The amino acid substitutions were performed using the PyMOL Mutagenesis Wizard tool, selecting the lowest energy rotamer for every substitution. In order to close gaps resulting from deletions, I created the missing backbone bonds to ensure backbone continuity and allowed the structure to energy minimise until convergence in OpenMM.

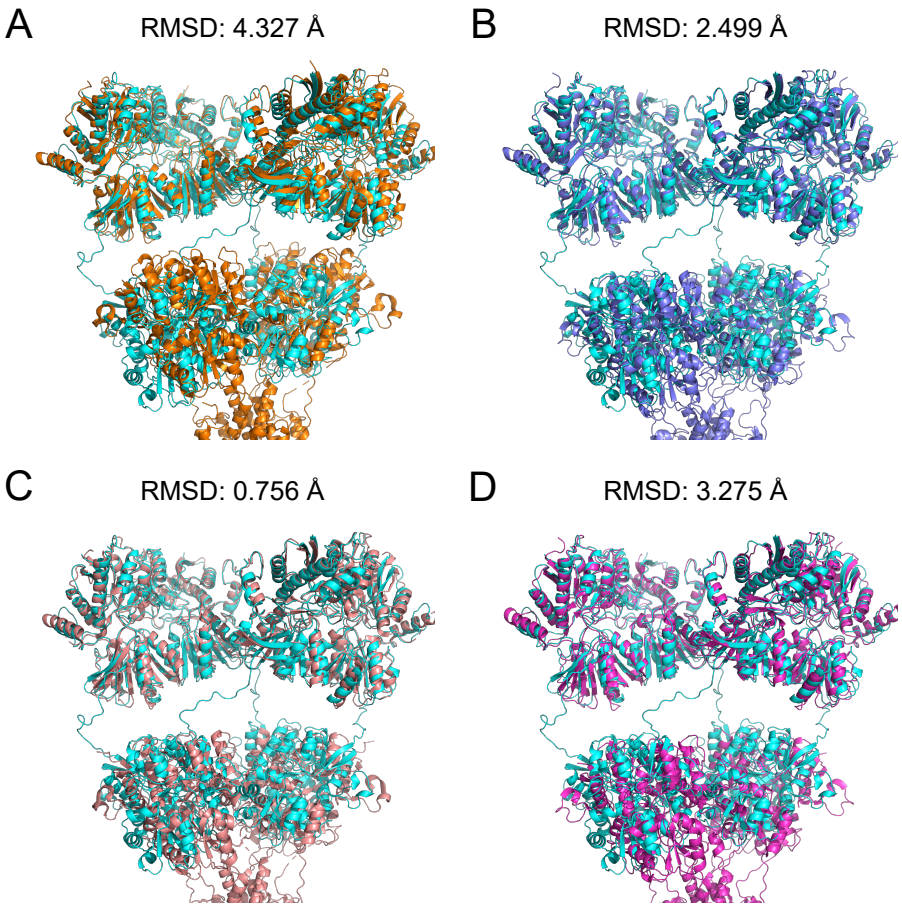

Figure 2.4: Structure alignments of GluA1A2A1A2 heterotetramer model built by me with published CryoEM GluA1A2A1A2 structures: A. 6QKZ [231]. B. 6NJL [20]. C. 7OCA [232]. D. 7LDD [233].

In order to verify that the structure of the GluA1A2A1A2 heterotetramer does not diverge too far from the real published structures of GluA1A2A1A2 AMPAR, I performed structure

alignments with several published CryoEM structures (Figure 2.4).

I used the `super` command to align only the CA atoms of whole structures (except for structure 6QKZ, for which `super` could not be used, therefore I used `cealign` instead) and compute CA-only RMDS values (Figure 2.4).

Further, I was interested in whether the change in residues at the interface between CII toxin and AMPAR LBDs from GluA2 to GluA1 residues would cause clashes in the prepared structure. To evaluate this, I focused on residues which differ between GluA1 and GluA2 LBDs and are within 10 Å from any CII toxin residues in the A/C subunits of the original homotetrameric GluA2 model. Table 2.1 shows the identities of the corresponding residues in GluA1 and GluA2 (numbering in line with the numbering in the alignment - Figure D.1). Of the seven GluA1/GluA2 residue pairs that fit the criteria, four had smaller side chains in GluA1 than GluA2, and therefore would not be a risk for clashes. I examined the positions of the three remaining residues (corresponding to GluA1 P469, R485, and R757) in the model and concluded that they were positioned far away enough from the toxin to not cause clashes.

Table 2.1: LBD residues differing between GluA1 and GluA2 AMPAR subunits and located in A/C AMPAR subunits within 10 Å of CII toxin.

GluA1 residue	**GluA2 residue**
P469	A476
A473	I480
R485	K492
E682	D689
K689	R696
A755	S762
R757	G764

p53-MDM2 system

In order to validate the new network analysis approach, I carried out additional MD simulations of another system, a pair of proteins well-researched in terms of their interactions: p53 (tumour suppressor which regulates cell processes such as cell cycle [234] and apoptosis [235]) and MDM2 (regulator of p53 [236]). In nearly half of human cancers, p53 is inactivated by a mutation [237], and in many others, its inactivation is due to MDM2 [238]. Due to their relevance in the cancer research field, the interactions between the two proteins have been studied extensively.

The simulated system (Figure 2.5) was built based on the crystal structure of a fragment of MDM2 bound to the transactivation domain of p53 (1YCR [239])). Terminal residues of either

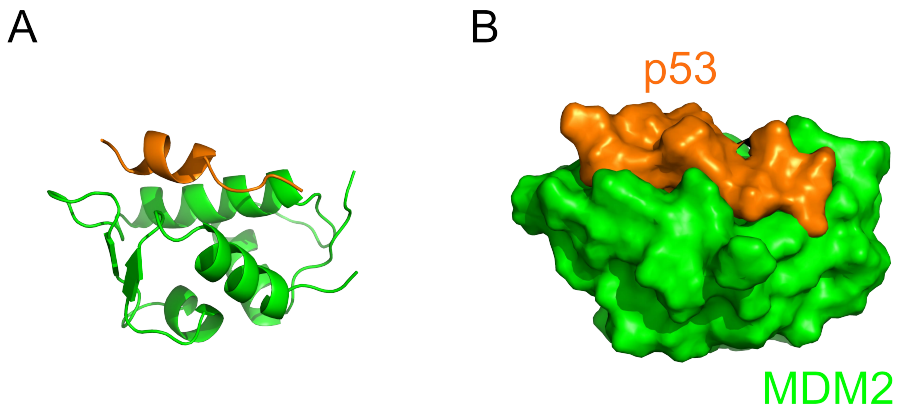

Figure 2.5: Simulated system – p53-MDM2 complex (PDB ID: 1YCR [239]. A. Cartoon representation. B. Surface representation.

peptide which were missing from the structure were not modelled in; therefore, as neither the N- nor C-termini of the simulated peptides coincided with full-length MDM2 or p53 termini, the termini were capped (N-termini with ACE, C-termini with NME). There were no non-terminal missing residues or atoms.

2.1.1.2 Running MD simulations

All simulation input files were prepared in AMBER tLEaP [240, 241] using the ff14SB force field [172] for protein components of the system, GAFF2 [228] for glutamate and dye molecules, and the TIP3P water model [242] for the solvent. All systems were neutralised with appropriate ions and solvated in tLEaP. For each of the simulated systems, I generated a .prmtop file with parameters and topology, an .inpcrd file with atom coordinates, and a .pdb file which was used to visually assess the correct preparation of the system.

MD simulations were carried out in explicit solvent (water) using OpenMM software [243] and the .prmtop and .inpcrd input files. 10 replicates were run for each of the simulated systems to improve sampling of their conformations [244, 245].

Each simulation was run at 300 K and with periodic boundary conditions applied. The simulated time was 20 ns for each replicate, with a time step of 2.5 fs and conformation snapshots saved to the output trajectory every 40 000 steps, resulting in a total of 200 frames for each trajectory in a simulation set. Simulations used a Langevin integrator [246] with friction coefficient of 1 ps^{-1} and the Particle mesh Ewald (PME) method [247] for evaluating Coulomb interactions with a cut-off of 1 nm.

A summary of all simulations of the AMPAR-CII toxin system carried out for this thesis can be found in Table A.1 in Appendix A

2.1.1.3 Simulation quality control and RMSF

The trajectories obtained as an output of the MD simulations were assessed with several measures as a means of quality control to ensure that over the simulated time, the system has reached an equilibrated state.

Root mean square deviation (RMSD)

Root mean square deviation (RMSD) is a measure commonly used in structural bioinformatics to quantify similarity between two structures [248]. RMSD is computed by first centering all conformations in a simulation trajectory and subsequently comparing the coordinates of all or a set of atoms in the structure with a reference structure:

$$RMSD = \sqrt{\frac{\sum_{i=1}^{N}(x_i^t - x_i^{ref})^2}{N}} \tag{2.1}$$

where N is the number of atoms in the structure, x_i^t is the position of the atom in the target structure (for which the RMSD is being calculated), and x_i^{ref} is the position of the equivalent atom in the reference structure (against which the target structure is being compared). I used the starting frame as the reference structure for each trajectory and computed the RMSD based on coordinates of all atoms (as opposed to e.g. only looking at backbone atoms).

In an equilibrated trajectory where no major conformational changes are occurring, the RMSD of the system plotted against the time course of the simulation initially increases, but then reaches a plateau. RMSD values that continue increasing throughout the course of the simulation trajectory may be indicative of large conformational changes occurring in the system, which should be inspected before proceeding with further analyses if it is not the expected behaviour of the system.

Temperature

During the simulations, several observables, including the system's temperature, were monitored alongside collecting conformation snapshots in order to assess the quality of the resulting trajectories. In an equilibrated trajectory of a constant temperature system, the temperature, plotted against the time course of the simulation, will initially sharply increase and then fluctuate closely around the pre-set value in response to the thermostat algorithm. Here, the simulation temperature was set to 300 K.

Potential energy

Another simulated system observable which was monitored throughout the run of every simulation and subsequently inspected to evaluate the quality of the trajectory is the potential energy. In an equilibrated trajectory, the potential energy of the system, plotted against the time course

of the simulation, should reach a plateau. A systematic drift in the potential energy value along the course of the simulation suggests that the system has not equilibrated.

RMSF

Root mean square fluctuation (RMSF) is a measure related to the fluctuations of individual residues of the structure over time – a high RMSF value indicates that a given residue fluctuates or moves around a lot during the simulation, while a low RMSF value indicates more static residues. RMSF values were computed using CPPTRAJ [249].

The RMSF of each residue was computed as a mass-weighted mean of fluctuations of its backbone atoms across the trajectory after centering all conformations in the trajectory, i.e.

$$\langle RMSF_{res} \rangle = \frac{(\sum RMSF_{atom}) \cdot m_{atom}}{\sum m_{atom}} \tag{2.2}$$

where angle brackets represent an average over all input frames, $RMSF_{res}$ is the RMSF for the residue, m_{atom} is the mass of a backbone atom, and $RMSF_{atom}$ is the RMSF of the backbone atom, calculated as follows:

$$RMSF_{atom} = \sqrt{\langle (x_{atom} - \langle x_{atom} \rangle)^2 \rangle} \tag{2.3}$$

where x_{atom} represents the position of the atom [250].

2.1.2 Computational alanine scanning

In alanine scanning mutagenesis, single mutations to alanine are introduced to the protein of interest in order to determine which amino acid residues contribute the most to the overall free energy of interaction [251]. However, performing experimental alanine scanning can be time-consuming and expensive, particularly in the case of proteins such as CII, which express at very low yields [151] and require multiple lengthy rounds of protein expression in order to produce enough protein for downstream characterisation and further experiments. Therefore, *in silico* alanine scanning methods have been developed to predict free energy contributions based on protein structures [252].

I used one of such computational approaches, BudeAlaScan [253], also available as a web server [254], to investigate the contributions of CII toxin residues to the overall energy of its interaction with AMPAR. As the simulated system is very large in size, we decided against using the whole equilibrated portion of each trajectory as input to the alanine scanning program and instead chose to extract 3 frames per trajectory. Frames were extracted from each trajectory based on the identified equilibrated portion (Figures 3.1, 3.6, and E.1); one frame from the beginning of the equilibrated portion, one from the middle, and one from the end. The resulting .pdb files were prepared by dividing the topology into AMPAR ATDs, AMPAR LBDs, and CII toxin in order to speed up computation. CII was assigned as ”ligand” and the appropriate

AMPAR portion as ”receptor”. The results for each residue were collated and the mean and standard deviation of the obtained values were computed for each residue. A positive $\Delta\Delta G$ value indicates positive contribution to the overall interaction and a residue is considered to be an ”interaction hotspot” if the free binding energy change upon its mutation to an alanine residue is at least 1 kcal/mol (4.18 kJ/mol). Residues with -1 – 1 kcal/mol free binding energy change are considered to be neutral in the context of their contribution to the interaction [255, 253].

The same process was followed for computational alanine scanning analysis of the p53-MDM2 system, with p53 assigned as ”ligand”, and MDM2 as the ”receptor”.

2.1.3 Network analysis with NAppEd

We were interested in developing a new approach for RIN analysis of MD trajectories which would build on the capabilities of RING 3.0 (at publication of RING 4.0, my work on the network analysis approach had been mostly completed, and as the speed of computation of the previous version, RING 3.0 [217], was adequate for my analysis and the added interaction types were outside of the scope of my study, I decided to continue using RING 3.0 rather than upgrading to RING 4.0.) and provide opportunity for focusing specifically on interactions between protein partners in complexes.

I developed the network analysis approach, which we decided to called NAppEd (Network Analysis of protein-protein interactions - Edinburgh) to take advantage of the MD simulation trajectory dataset produced during this project and utilise it as source of dynamic interaction information to collate and analyse, rather than having to rely on a single static structure. Based on this dynamic information, we could try to understand whether interactions we may observe in a single frame are relevant in the context of an entire trajectory or set of simulation replicates. The nuanced understanding of the network of interactions between two proteins in an MD simulation is essential for the hypothesis-generating role of our approach in identifying residues that contribute most to the overall interaction. This allows us to be able to more intentionally target those crucial residues in experimental procedures, which is especially meaningful in cases such as our AMPAR-CII toxin system, where purification of the toxin is low in yield ($\sim$100-200 μg from 12 l of bacterial culture [151, 63]), expensive, and time-consuming.

2.1.3.1 Basic properties of NAppEd networks

Basic properties of the interaction networks in NAppEd (see Figure 2.6):

- nodes represent individual amino acid residues
- edges represent interactions between pairs of residues (nodes they connect)

- interaction networks are undirected (i.e. edges do not have an orientation) as most interaction types do not have an orientation and the orientation of those for which it can be determined is outside the scope of my analysis

- interaction networks are multigraphs (i.e. multiple edges between the same pair of nodes are allowed) in order to be able to distinguish between and investigate different interaction types

- interaction networks are weighted (i.e. each edge has a weight attribute), with the weights representing the overall number of frames in which the interaction represented by a given edge is present

- Only one edge per interaction type is allowed between the same pair of nodes (i.e. if two residues are found to make van der Waals interactions via multiple pairs of atoms, this will only be represented as a single van der Waals interaction in a NAppEd network).

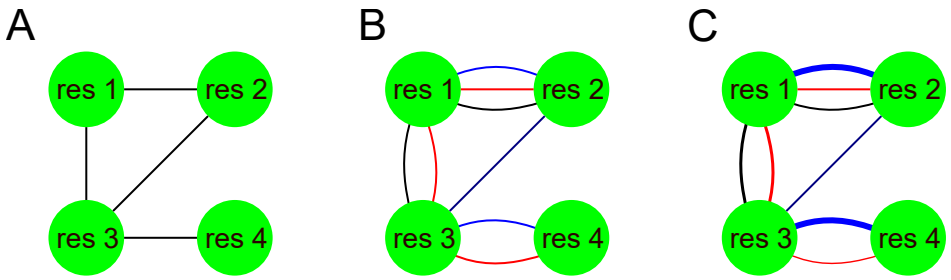

Figure 2.6: Three representations of the same toy example residue interaction network, showing different levels of information about the network. A. Undirected, unweighted graph with only a single edge allowed between any pair of nodes. The network shows the presence (e.g. edge between res 1 and res 2) or absence (e.g. no edge between res 2 and res 4) of interaction between any two nodes (residues). B. Undirected, unweighted multigraph – different edge colours represent different interaction types. The network shows the presence/absence of interaction between any two nodes (as above), and the type of interaction (e.g. res 1 forms interactions of three different types with res 2, but only two different types with res 3). C. Undirected, weighted multigraph – edges of the different colours represent different interaction types and different edge widths represent different weights. The network shows the presence/absence of interaction between any two nodes (as above), type of interaction (as above), as well as a relative measure of how many frames a given interaction was present in across the simulation (e.g. the interaction between res 3 and res 4 represented as the blue line was present in more frames than the interaction between the same two residues represented as the red line).

2.1.3.2 NAppEd Process summary

In order to obtain a summary network from the MD simulation trajectory, NAppEd includes a number of steps, summarised in Figure 2.7. Firstly, the trajectory file can undergo optional pre-processing, after which RING 3.0 is used to produce files describing the nodes and edges of residue interaction networks for each frame of the trajectory. These networks are collated to produce a summary residue interaction network, which contains information about interactions across the whole trajectory. Summary networks from all trajectories forming one simulation set (10 replicates) are then collated into a meta-network, which summarises interactions across the entire simulation set. Finally, the properties of the networks can be investigated with additional functions and the networks can be interrogated via interactive visualisations.

Pre-processing

The optional pre-processing steps utilise MDTraj [256] for accessing the topology of the input simulation trajectory and can be useful in the following situations:

- if the simulated system is converted into a single chain in the process of running the simulation. It is useful to reassign chain identifiers to separate chains in the trajectory, as this may be used for downstream filtering of the analysis results (e.g. to only include intra-chain interactions or interactions between two specific chains)

- if the simulated system is large, but only a smaller portion of it is of interest in the analysis (e.g. only the regions in the immediate vicinity of the binding interface between two interacting proteins). The trajectory can be filtered to only include residues that at any point in the simulation come within a specified threshold distance from the region of interest. This limits the number of residues and therefore interactions that need to be computed by RING 3.0.

Processing with RING 3.0

The pre-processed .pdb file with reassigned chain identifiers can then be passed as input to RING 3.0 [217], which computes interactions between all possible pairs of residues that are separated from each other by at least 3 residues in the same chain's sequence (default value). RING 3.0 produces a number of files as output, including a nodes file, which contains information about each of the nodes (residues) in the computed network, such as the chain, position, and residue 3-letter code; and an edges file, which contains information about each of the edges (interactions) in the network, such as node identifiers of the source and target node for the given edge, interaction type (hydrogen bonds, van der Waals interactions, ionic interactions, π–cation interactions, and π–π interactions), and which model (frame) in the trajectory the edge was found in.

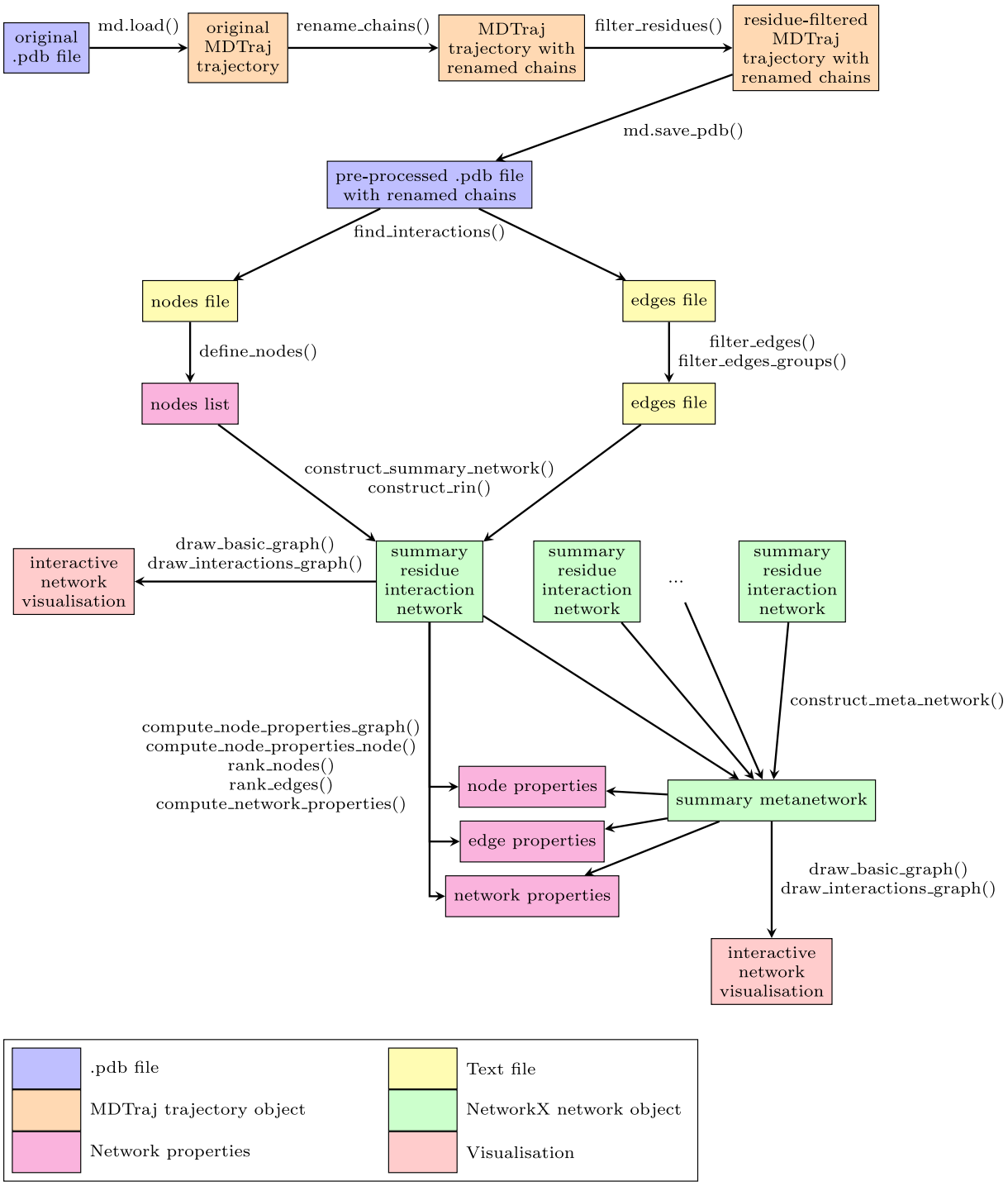

Figure 2.7: Diagram illustrating the process of residue interaction network analysis for MD simulation trajectories with NAppEd.

Constructing residue interaction networks

In the next step of the process, the nodes file is used to produce a nodes list. The edges can optionally be filtered to include only edges between user-defined groups of residues (e.g. only interactions between two specific groups of chains in the simulated system). The nodes list and edge file are then used to construct a residue interaction network for a single defined frame or the entire simulation trajectory as a NetworkX [257] MultiGraph object. It is important to note that although the edges file produced as RING 3.0 output may contain multiple interactions of the same type between the same pair of residues, I have decided to only represent them as one edge of the appropriate interaction type to simplify the analysis of the network. I also decided not to include interaction sub-type information (i.e. whether the interacting atoms are part of the main chain or side chain of the amino acid residue) as this level of detail is not within the scope of my analysis.

Once the network is constructed, any isolates (nodes with degree 0, i.e. nodes without any links to other nodes) are removed.

A summary network is constructed by adding together residue interaction networks constructed for each frame of the trajectory. Each edge representing an interaction present in at least one frame of the trajectory will therefore by present in its summary network. In order to understand how prevalent each interaction is in the scale of the simulation trajectory, each edge is assigned a weight attribute, which represents the number of frames in which the edge is present; and a max_persistence attribute, which represents the maximum number of consecutive frames that the edge is present in.

Summary networks from all simulation replicates can be combined into a meta-network, which summarises the information from them all. Here, the weights of the same edge from the summary networks are summed up (i.e. if an edge is present for 100 frames in one replicate and 50 in another, its weight in the meta-network combining the two summary networks would be equal to 150); however, the max_persistence value is taken as a maximum of the values from summary networks (i.e. if an edge is present for a maximum of 20 consecutive frames in one replicate and 25 consecutive frames in another, its max_persistence value in the meta-network combining the two would be 25).

Analysis of residue interaction networks

Once a summary or meta-network is constructed, it can be visualised in the form of an interactive graph, built using the Bokeh package [258]. The network can also be broken down into networks containing only edges of a particular interaction type (Figure 3.8). The interactive visualisation of any network can be explored by zooming in and hovering over nodes of interest, which causes a box with additional information about the node to appear (Figure 3.8 A). Based on the visual inspection of the interactive network, the user can then identify interactions or

residues they find to be of interest for their analysis.

The visualisation of the residue interaction network encodes more than just the presence or absence of interaction between pairs of residues:

- edge lengths are inversely proportional to edge weights, i.e. edges with higher weights are shorter in length or nodes representing residues that form interactions in many frames are positioned closer together than those representing residues that only interact in a few frames

- the degree of each node (the number of edges incident to the node) is encoded in the size of the node glyph – the higher the degree, the larger the glyph size

- shape and colour of the node glyphs can be used to encode user-defined node properties such as domain the residue belongs to.

Summary and meta-networks can also be analysed by investigating the node, edge, and network properties. Node properties can be computed for one node of interest or for all nodes in the summary network. Nodes can also be ranked according to their degree (the number of edges incident to the node) or weighted degree (the sum of weights of edges incident to the node), to give the user information about residues involved in the highest number of interactions, as well as those involved in interactions present in many frames.

Edge properties can be investigated by looking up a specific edge's weight and max_persistence values or by ranking all edges in the network, either by weight or by max_persistence.

Network properties (number of connected components, number of nodes, number of isolates – nodes of degree 0, number of edges, and sum of edge weights) can be computed to get a general sense of the structure and size of the network.

2.1.3.3 Network analysis

The GluA2 AMPAR ATD-LBD-Glu-CII and p53-MDM2 simulations were prepared and carried out as described in Section 2.1.1.2. The equilibrated portion of the resulting trajectories was then processed with NAppEd in the process described in Section 2.1.3.2 (Figure 2.8). Summary meta-networks were visualised and investigated in more detail.

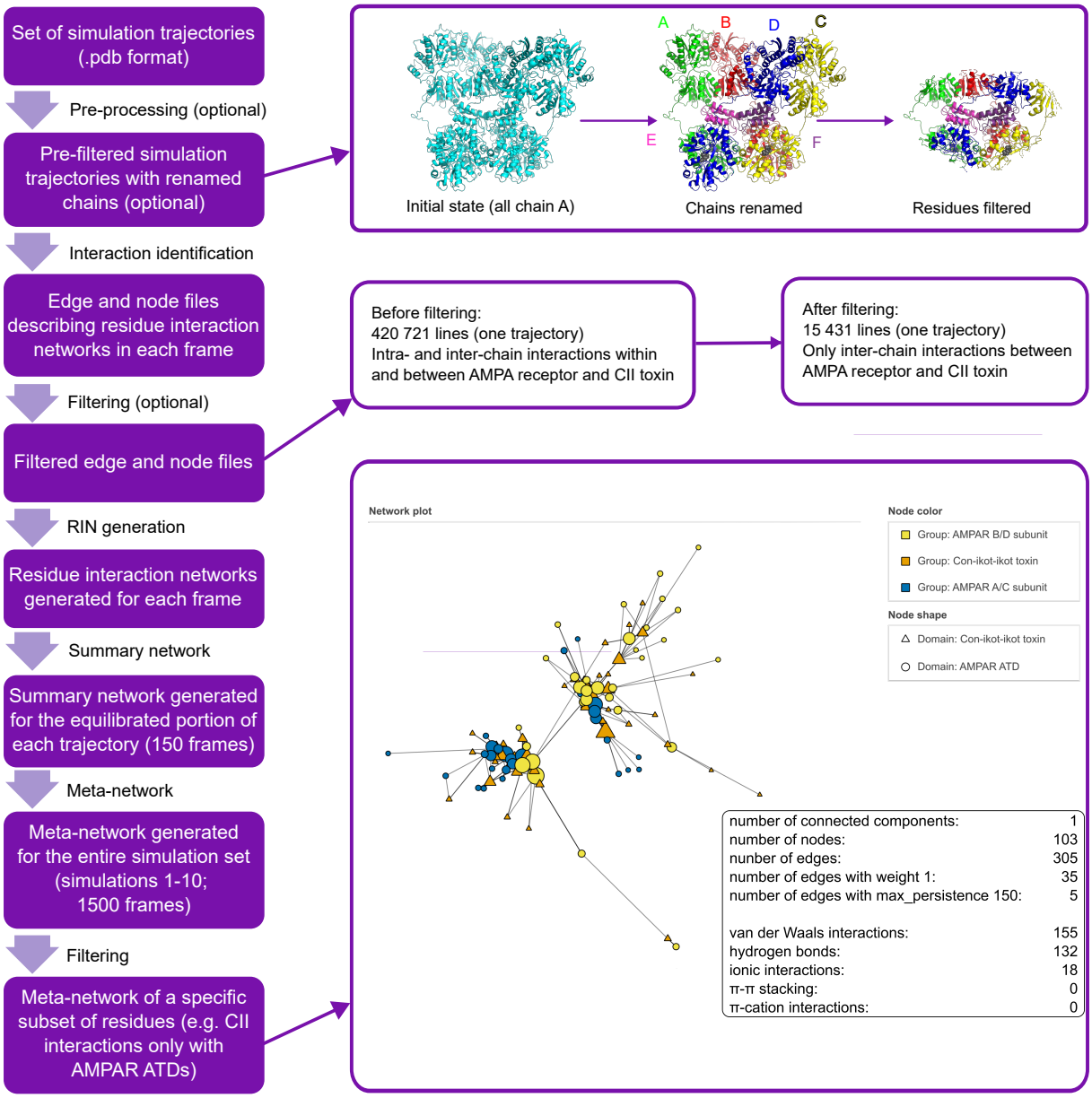

Figure 2.8: Diagram illustrating the process of residue interaction network analysis for MD simulation trajectories of the AMPAR-CII complex with NAppEd.

2.2 Experimental methods

2.2.1 Expression of CII in BL21(DE3) *E. coli* using the csCyDisCo system

Figure 2.10 summarises the CII expression protocol. We used the original protocol from Chen *et al.* [151], modified to include the use of the csCyDisCo system 1.5 and BL21(DE3) *E. coli* strain as opposed to the Origami(DE3) strain used originally.

We expressed WT CII as well as the Y54A CII mutant using BL21(DE3) *E. coli* strain [259], which we co-transformed with the csCyDisCo plasmid [224] (received as a kind gift from the Ellgaard lab at the University of Copenhagen), and either CII plasmid (Figure 2.9) or CII Y54A

plasmid.

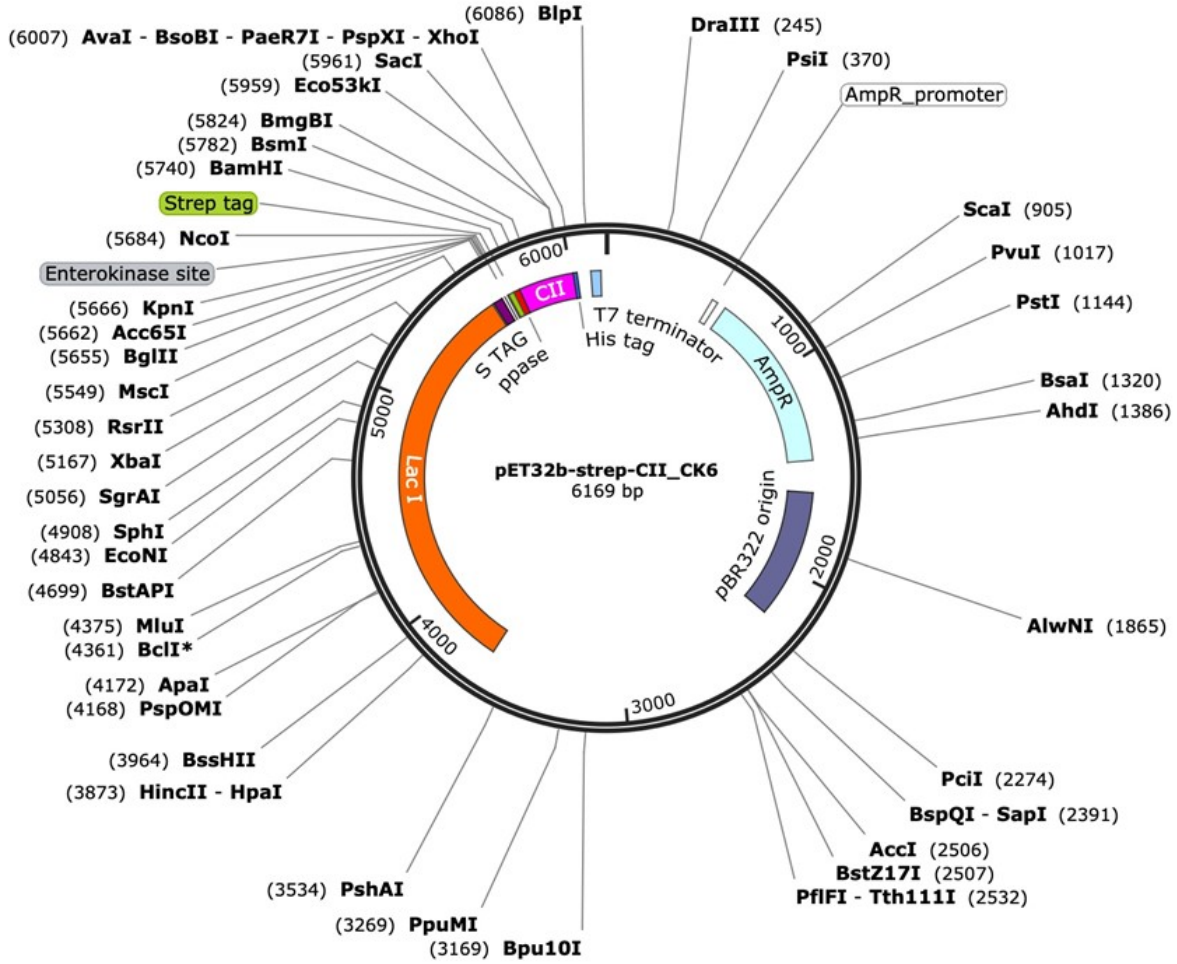

Figure 2.9: CII toxin plasmid map. Figure created with SnapGene [260].

BL21(DE3) cells were transformed using approximately 100 ng DNA of the plasmid carrying WT or Y54A CII toxin gene, and 100 ng of the csCyDisCo plasmid (with the exceptions of WT CII expression runs 3 and 4, where 50 ng of the csCyDisCo plasmid was used). The bacteria were plated on an LB agar plate containing chloramphenicol (25 µg/ml) and either ampicillin or carbenicillin (100 µg/ml) and incubated at 37°C overnight, after which several well-defined colonies could be observed for both WT and Y54A CII.

We explored whether the use of BL21(DE3), a faster-growing *E. coli* strain than the Origami strain used in the original protocol, would allow us to remove the pre-pre-culture step. To do this, I set up two parallel pre-culture protocols:

- PPC → PC (pre-pre-culture → pre-culture), where I used a single colony picked from the bacterial plate to inoculate 3 x 5 ml of pre-heated LB medium with antibiotics in 50 ml Falcon tubes as pre-pre-culture, which was then incubated for 4.5 hours at 37°C with shaking at 200 RPM. Next, all 15 ml of pre-pre-culture was used to inoculate 250 ml of pre-heated LB with antibiotics (pre-culture)

- plate → PC (plate → pre-culture), where I used a single colony picked from the bacterial plate to inoculate 250 ml of pre-heated LB with antibiotics.

Both pre-cultures were inoculated at the same time and incubated overnight at 37°C at 190 RPM, after which their OD600 was compared to determine whether including a pre-pre-culture step was necessary. As the OD600 values were comparable for both pre-cultures (2.9 for PPC → PC and 2.8 for plate → PC), we decided to only proceed with the plate → PC pre-culture protocol in subsequent rounds of toxin expression.

The plate → PC pre-culture was used to inoculate 12 l of main culture, which continued to be incubated at 37°C with shaking at 180 rotations per minute until the OD600 reached a value between 0.8 and 1.0 (around 3 hours), at which point the incubator temperature was lowered to 16°C and protein expression was induced using 100 µM IPTG.

Following the addition of IPTG to the main culture, it was incubated for further 20–23 hours at 16°C with shaking at 180 RPM, after which time the cells were harvested by centrifugation. Harvested cells were flash-frozen with liquid nitrogen and stored at -80°C until they could be used for the further steps of the protocol.

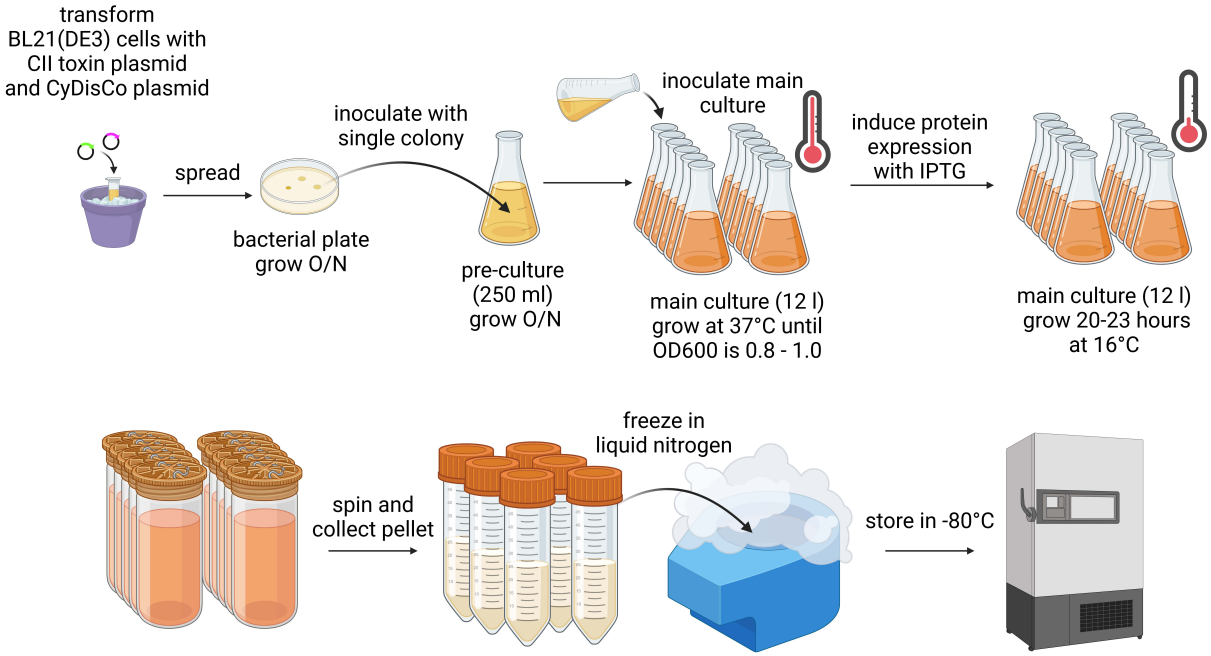

Figure 2.10: Summary of the CII toxin expression protocol using BL21(DE3) *E. coli* and the csCyDisCo system. Figure created with BioRender.com.

2.2.2 Purification of CII

Preparation of cell lysate

The frozen harvested *E. coli* cells were thawed on ice with addition of 400–500 ml of cold lysis buffer (containing 50 mM Tris, 150 mM NaCl, and 5 mM EDTA), protease inhibitor tablets, DNase I (in order for the resulting lysate to be less viscous and able to pass through a 0.22 μm filter), and $MgCl_2$ (to provide an excess of Mg^{2+} ions for the correct functioning of DNase I in the presence of EDTA, which is a chelating agent). The cell suspension was passed through the cell disruptor three times at 25 kPsi and subsequently sonicated for a total of 2 min in the 30 s ON/59 s OFF sonication pattern at 40% amplitude of the sonicator used (Fisherbrand Model 505 Sonic Dismembrator).

The cell lysate was centrifuged and the supernatant, containing our target protein, was filtered through a 0.22 μm filter before applying to the StrepTactin column.

StrepTactin affinity chromatography

We used a 10 ml StrepTactin column, buffers Strep_A (20 mM Tris, 150 mM NaCl, and 1 mM EDTA) and Strep_B (same as Strep_A, with an addition of 2.5 mM desthiobiotin) and an ÄKTA Pure chromatography system to perform affinity chromatography. The eluted fractions of 2 ml each were collected in a deep-well 96-well plate for further steps of the purification protocol.

SDS-PAGE electrophoresis was performed on the peak fractions to verify the presence of target protein in the fractions. The peak fractions from multiple expression runs were pooled and concentrated using Vivaspin 20 or Vivaspin 15 centrifugal concentrators with molecular weight cut-off of 30 kDa. The affinity purification tag was cleaved off using PreScission Protease at 1:100 (PSP: target protein) mass ratio and precipitated with methanol. Methanol was then exchanged for StrepTactin buffer A using a centrifugal concentrator. glutathione (GSH) was added to the sample to a final GSH concentration of 1 mM in order to increase the fraction of toxin existing as dimer by providing a redox agent to participate in disulfide bond reshuffling. Before applying the GSH-treated sample to the ion exchange chromatography column, it was diluted 10-fold with SP_A buffer.

The column was regenerated between uses according to the manufacturer's protocol.

Ion exchange chromatography

We used a 1 ml HiTrap Sulfopropyl Sepharose High Performance column, buffers IEX_A (30 mM NaAc) and IEX_B (same as IEX_A, with the addition of 1 M NaCl), and an ÄKTA Pure chromatography system to perform cation exchange chromatography. The eluted fractions of 1 ml each were collected in a deep-well 96-well plate and saved for further steps of the purification protocol.

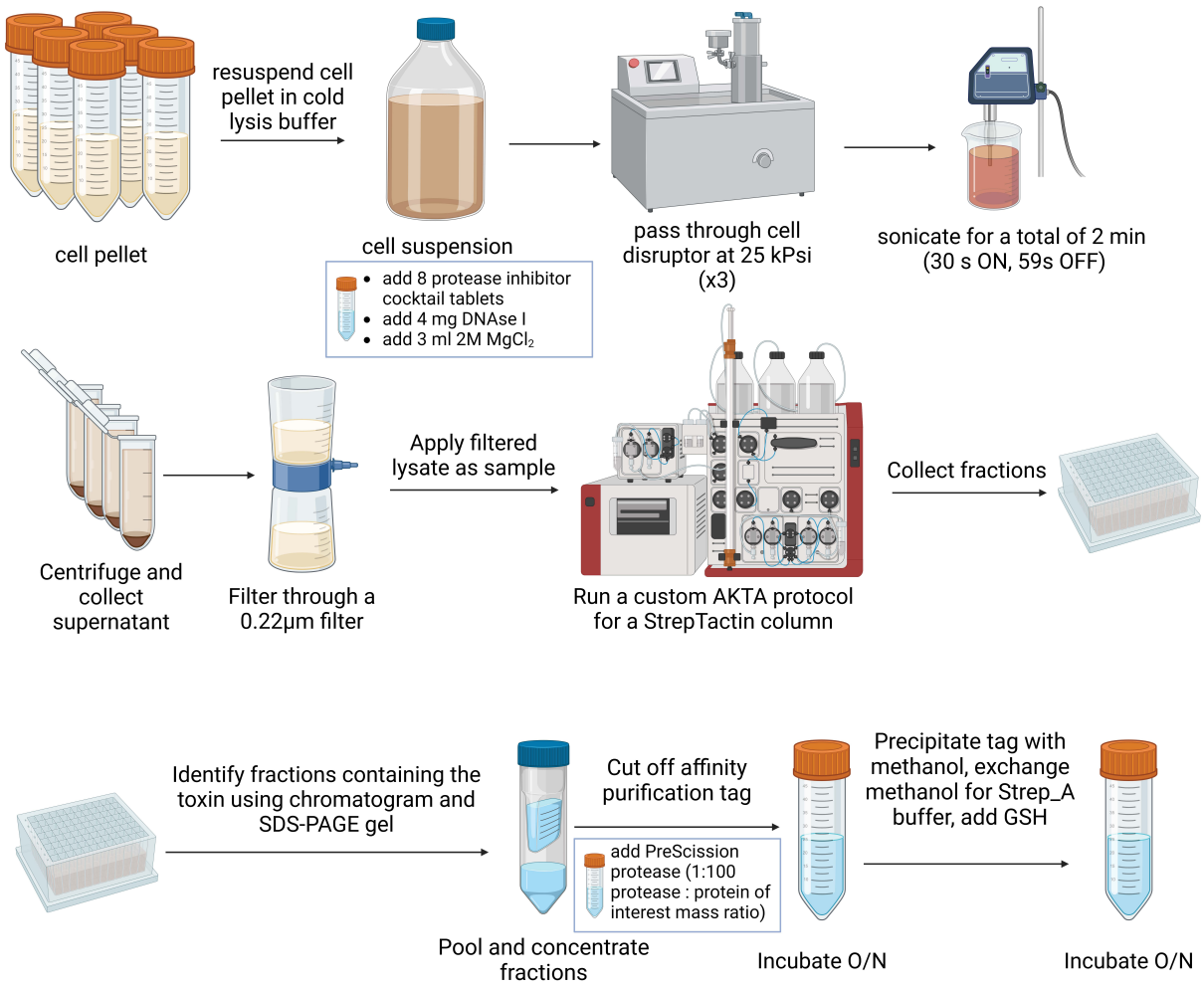

Figure 2.11: Summary of CII purification protocol – preparation of cell lysate and StrepTactin affinity chromatography. Figure created with BioRender.com.

SDS-PAGE electrophoresis was performed on the peak fractions to verify the presence of target protein in the fractions. Peak fractions were collected and pooled together, concentrated using an Amicon Ultra-4 centrifugal concentrator and buffer exchanged for SEC buffer in preparation for size exclusion chromatography.

Any protein concentration measurements throughout the thesis were carried out using a NanoDrop spectrophotometer and appropriate buffer as the blank solution.

The column was regenerated between uses.

Size exclusion chromatography

We used a Superdex 75 10/300 GL column, SEC buffer (10 mM HEPES and 150 mM NaCl), and an ÄKTA Pure chromatography system to perform size exclusion chromatography. The eluted fractions of 0.5 ml each were collected in a deep-well 96-well plate.

SDS-PAGE electrophoresis was performed on the peak fractions to verify the presence of

target protein in the fractions.

The column was cleaned between uses.

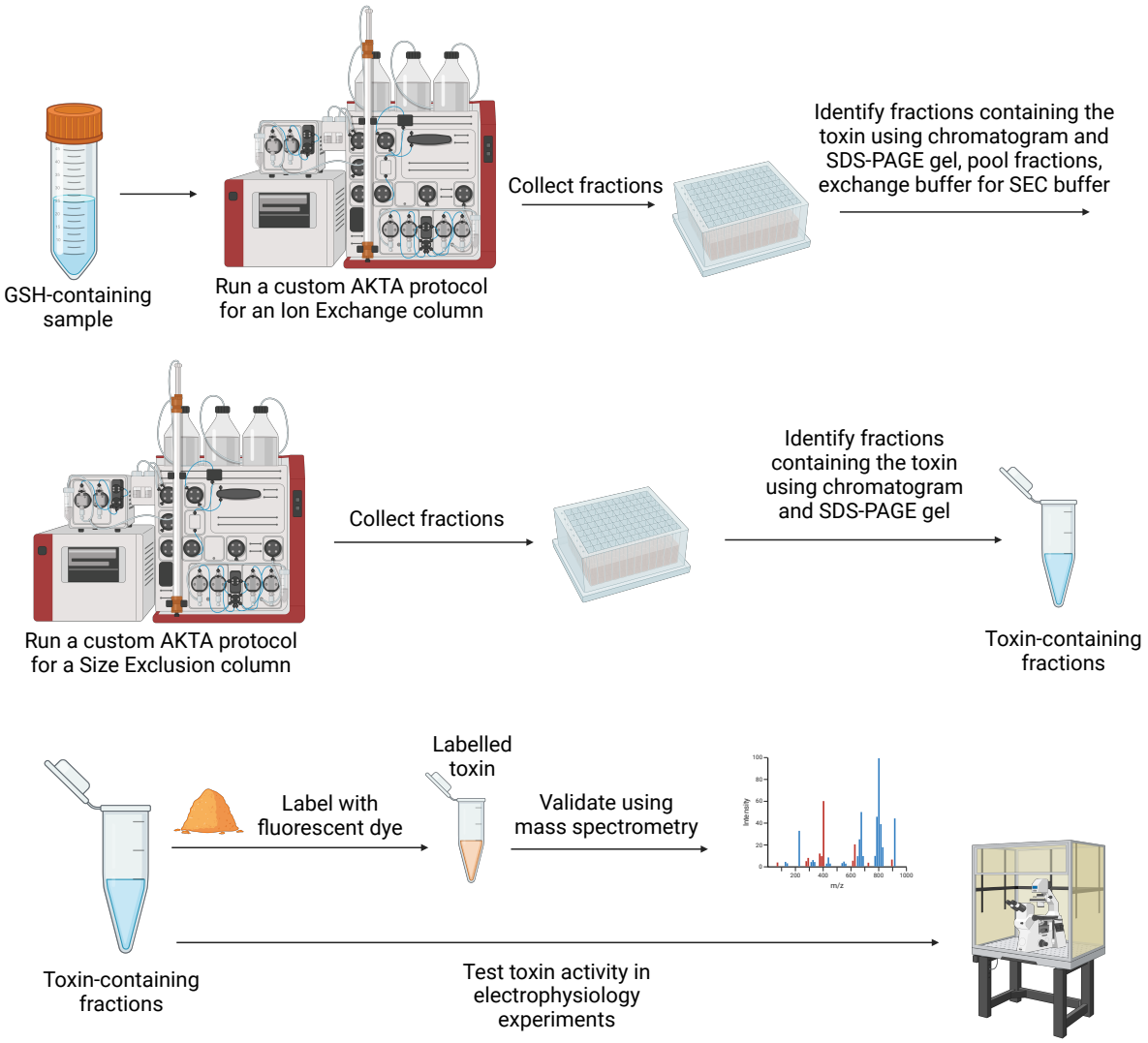

Figure 2.12: Summary of WT CII purification protocol – ion exchange and size exclusion chromatography and downstream experiments. Figure created with BioRender.com.

Polyacrylamide gel electrophoresis

SDS-PAGE gel electrophoresis was performed using home-made gels at acrylamide concentrations of 4% (stacking) and 15% (separating). Samples were prepared by mixing equal amounts of sample material and sample buffer (non-reducing for SEC fraction and IEX fraction gels and reducing for the rest). 10 µl of prepared sample was loaded into each sample well (with the exception of peak fractions from SEC of Y54A CII mutant, where 20 µl of sample was loaded into each sample well). For reference protein molecular weight markers, we used the PageRuler Broad Range Unstained Protein Ladder from Thermo Scientific, 1 µl of which was loaded onto the gel. Electrophoresis was performed at 80 V until the dye front had reached the

border between the stacking and resolving gel, and at 200 V thereafter.

Visualisation of bands of SDS-PAGE gels

SDS-PAGE gels of StrepTactin fractions were stained using the InstantBlue Coomassie Blue protein stain according to the manufacturer's instructions. SDS-PAGE gels of ion exchange and size exclusion chromatography fractions were silver-stained following a 30 min silver staining protocol [261].

2.2.3 Fluorescent labelling with PA-JF 646

We labelled WT and Y54A mutant CII toxin with a photoactivatable Janelia Fluor fluorescent dye, PA-JF 646 [229], at 30:1 dye:protein molar ratio, following the manufacturer's protocol.

The dye solution in DMSO was prepared by adding 50 µl of DMSO (anhydrous) to 300 µg of PA-JF 646. It was then divided into aliquots of 10 µl each and stored at -20°C.

For labelling of WT CII toxin, fraction B1 from size exclusion chromatography (Figure 3.16 B) was used concentrated with a centrifugal filtering device to 1.0 mg/ml (in about 35 µl). 15 µl of this concentrated toxin solution was mixed with 1.68 µl of 75 mg/ml sodium bicarbonate solution and 2.4 µl of PA-JF 646 for the labelling reaction and incubated at room temperature, protected from light, overnight. After the incubation period, 20 µl Tris-HCl (100 mM, pH 7.4) was added to the reaction mixture in order to quench the reaction.

For labelling of Y54A CII mutant, we used 50 µl of the 3.6 mg/ml Y54A sample ready for loading onto the size exclusion column (i.e. peak fractions from ion exchange chromatography pooled, concentrated, and buffer exchanged for SEC buffer) and diluted this amount 2-fold with SEC buffer, resulting in 100 µl of Y54A CII sample at 1.8 mg/ml. 11.2 µl of 74 mg/ml sodium bicarbonate solution and 26.8 µl of the PA-JF 646 solution were then added to the toxin solution and incubated on a rotary mixer at room temperature and protected from light overnight. After the incubation period, 140 µl of Tris-HCl (100 mM, pH 7.4) was added to the reaction mixture to quench the reaction. The labelled Y54A CII solution was loaded onto the size exclusion chromatography setup in order to test whether we can use the last purification step to remove unbound dye from the mixture while retaining the labelled target protein for further experiments.

Validation with mass spectrometry

A 30 µl sample of labelled WT CII at 0.275 mg/ml protein concentration was submitted to the University of Edinburgh School of Chemistry's Mass Spectrometry facility for analysis using high-resolution mass spectrometry (TOF MS ES+).

2.2.4 Electrophysiology

All recordings were performed in wild-type GluA2iQ AMPAR expressed in the Human embryonic kidney (HEK)-293 cell line (Sigma). Cells were transfected using a lipofectamine transfection kit (Invitrogen) and maintained according to standard protocol in Minimum Essential Medium supplemented with 10% v/v Fetal Bovine Serum, 2 mM L-glutamine, and 50 U/ml penicillin-streptomycin (all reagents purchased from Gibco). 4 hours following transfection, the cells were washed and the medium was changed to fresh MEM containing 30 μM of selective competitive AMPAR antagonist 2,3-dioxo-6-nitro-1,2,3,4-tetrahydrobenzo[*f*]quinoxaline-7-sulfonamide (NBQX). Cells expressing AMPAR were identified by green fluorescence from IRES co-expression of eGFP. Electrophysiological recordings were carried out after another 18–74 hours from outside-out patches to enable exogenous modulation of the receptors.

Recordings were performed at 22–25°C using patch clamp electrodes pulled from borosilicate glass (1.5 mm outer diameter, 1.17 mm inner diameter)(Harvard Apparatus) with resistance of 3–8 MΩ. The internal solution contained 115 mM NaCl, 10 mM NaF, 5 mM Na_4BAPTA, 0.5 mM $CaCl_2$, 1 mM $MgCl_2$, 5 mM HEPES, and 10 Na_2ATP, titrated to pH 7.3 with NaOH, 280–300 mOsm. The external solution contained 150 mM NaCl, 50 mM HEPES, 1 mM $MgCl_2$ at pH 7.3, 280 mOsm. Currents were recorded at -60 mV or -40 mV. Signals were low-pass filtered at 5 kHz and digitized at 20 kHz.

Rapid agonist application, i.e rapid solution exchange to the patches was achieved by alternating between continuously flowing solutions through lateral oscillation of a custom-made four-barrel application tool [63, 262].

All electrophysiology experiments included in this thesis were carried out by Alexander Edwards.

Chapter 3

Results

3.1 Molecular dynamics simulations

3.1.1 AMPAR GluA2 homotetramer in complex with WT CII

After running a full set of AMPAR GluA2 homotetramer ATD-LBD-Glu-CII simulations, I plotted several quality control measures as described in Section 2.1.1.3. As seen in Figure 3.1, the potential energy and temperature of the simulated system, as well as the all-atom RMSD from the first frame of each trajectory all reach a plateau during the simulation time, together suggesting that the trajectories reached equilibrium and can therefore be used for further analyses (Section 3.2.2).

For the purpose of downstream analyses, I decided to treat frames 50–200 (to the right of the grey dashed line in Figure 3.1 A, B, and C) as the equilibrated portion of the simulation as all three measures used to determine equilibration reach a plateau in this section across trajectories.

Figure 3.1 D shows structural alignments of the first (green) and last frame of two simulation replicates – one with a higher final RMSD (red), and one with a lower final RMSD (purple) – the colours correspond to the colours of lines in Figure 3.1 C. A visual assessment of the structures shows that as suggested by the RMSD plot, we do not observe significant structural rearrangements of the simulated system throughout the course of the trajectory and the RMSD reaches a plateau within the simulation time, like the other quality control measures.

3.1.2 AMPAR GluA2 homotetramer in complex with CII lysine mutants

The fluorescent dyes we are planning to use for super-resolution of AMPAR in the future – photoactivatable Janelia Fluor 549 and 646 [229] (PA-JF 549 and PA-JF 646, Figure 3.2 A) – both bind to the protein via a chemical reaction between the *N*-hydroxysuccinimide (NHS) ester group of the dye and the primary amine group of the protein, either at the side chain of a lysine residue or at the N-terminus (Figure 3.2 C). As con-ikot-ikot exists as a homodimer,

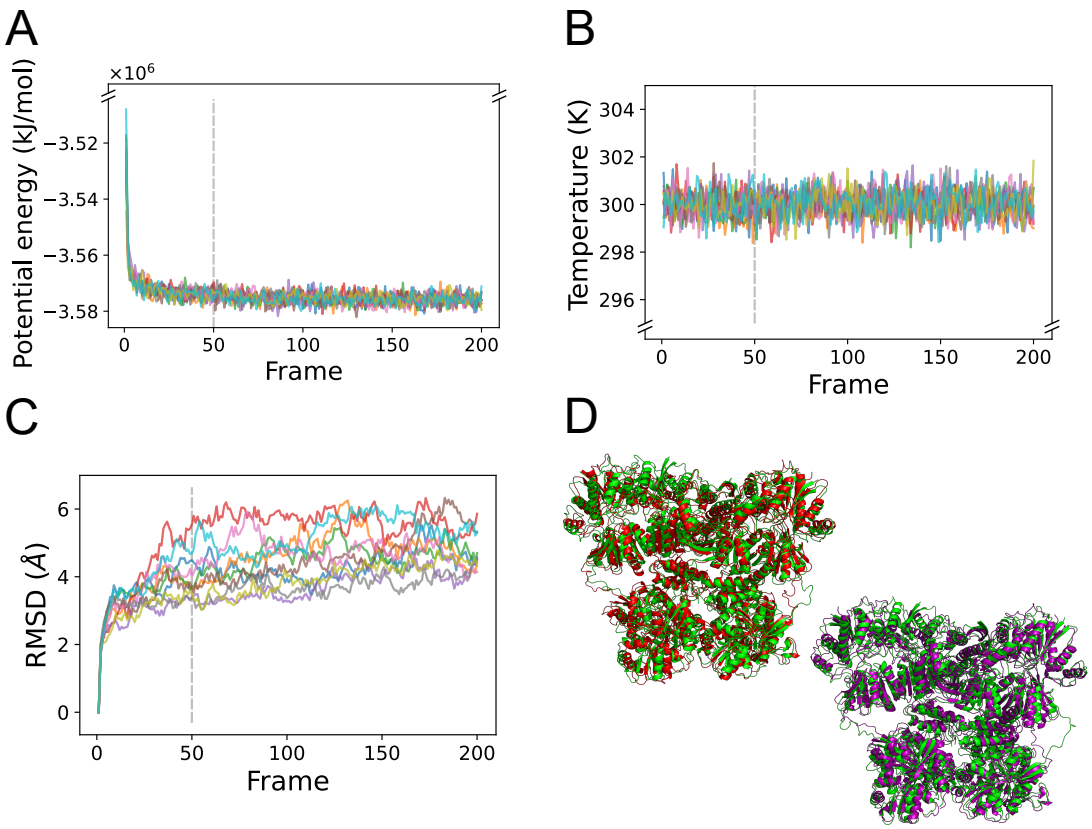

Figure 3.1: Quality control measures over the course of simulation – GluA2 homotetramer ATD-LBD-Glu-CII system. A. Potential energy. B. Temperature. C. RMSD. D. Structure alignments of first (green) vs last (red and purple) frames of two simulation replicates. The grey vertical lines in A.-C. show Frame 50, which was taken as the beginning of the equlibrated portion of the simulations.

each containing 4 lysine residues (K10, K30, K65, and K77), the overall number of available dye conjugation sites in the toxin is 10 (Figure 3.2 B).

If we intend to use CII as a fluorescent AMPAR marker for super-resolution imaging, it would be ideal for each toxin molecule to be labelled with exactly one molecule of the fluorescent dye, as with the degree of labelling (i.e. the ratio of fluorescent molecules to targets) equal to 1, we can confidently state that each fluorescent signal in the imaging data corresponds to one protein of interest, which would make the interpretation of fluorescent signal more relevant and convincing for quantitative analysis. With multiple conjugation sites available for the dye to attach to the protein, we cannot predict how many of the sites will be occupied by the dye on any given toxin molecule and not all molecules in a batch may become uniformly labelled, which would make the interpretation of fluorescent microscopy results challenging.

Therefore, we wanted to explore mutating lysine residues in CII to other amino acids which would not react with the dye due to the lack of an amine group in their side chains. Due to the location of lysine side chains in CII with respect to the rest of the protein as well as to the

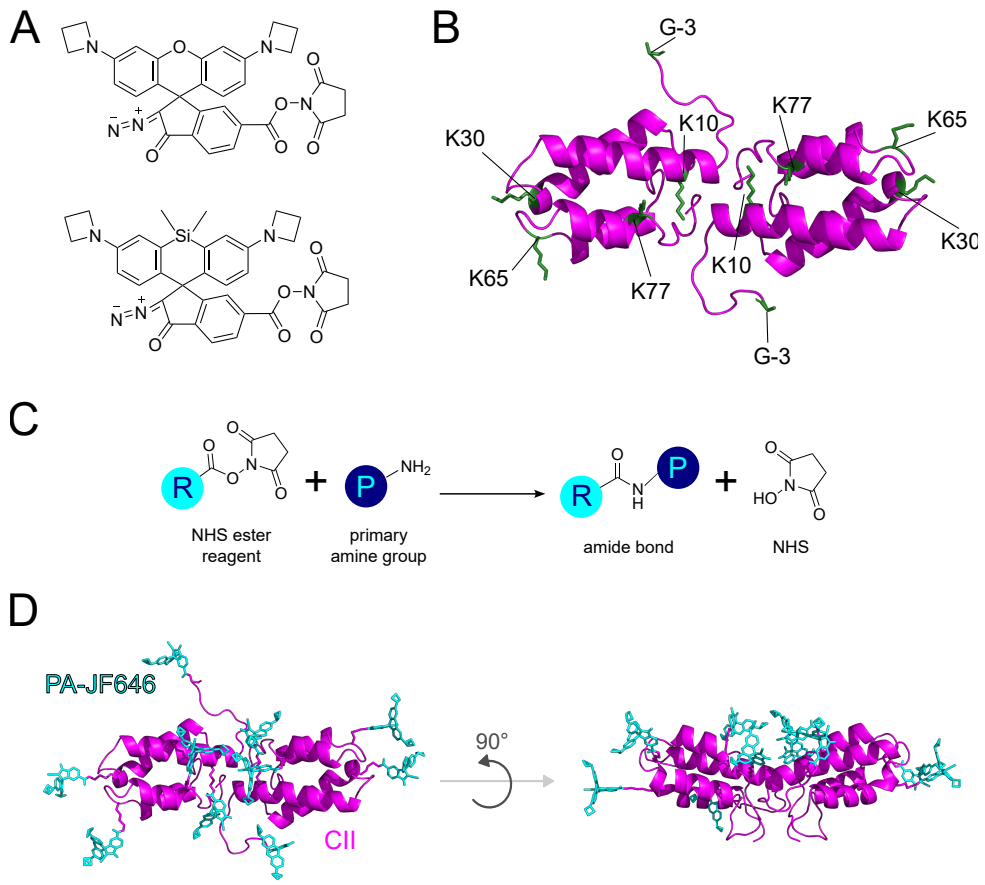

Figure 3.2: A. Photoactivatable Janelia Fluor (PA-JF) dyes [229] Top: PA-JF 549. Bottom: PA-JF 646. B. Primary amine groups in con-ikot-ikot toxin (green) – lysine residues and N-termini. Numbering of residues according to the 4U5H crystal structure [151]. C. The conjugation reaction between an NHS ester reagent and a primary amine. D. Con-ikot-ikot toxin (magenta) fully labelled (i.e. labelled at all sites indicated in B) with fluorescent dye PA-JF646 (cyan).

AMPAR LBDs, K65 (Figure 3.2 B) was selected as an attractive candidate for attaching the fluorescent dye. The remaining three lysine residues in each subunit would therefore be subject to mutation. However, it could turn out that some of the lysine residues in the toxin are crucial for the CII-AMPAR interaction, in which case mutating those residues would be undesired. To determine this, I examined the computational alanine scanning results from the GluA2 AMPAR ATD-LBD-Glu-CII simulations (Figure 3.3) in the context of lysine residues' contributions to the toxin's interactions with AMPAR LBDs, as this is where the main interaction interface is located.

10 of the CII residues exhibited scores $\geq$ 5 BUDE units ($\geq$ 1 kcal/mol): Q37, Y54, F34, and I49 from both CII subunits, E38 from subunit 1, and E48 from subunit 2 (Table G.1). Of these, three residues scored $\geq$ 10 BUDE units ($\geq$ 2 kcal/mol) – Q37 in subunit 1 and Y54 in both subunits. It is important to note that Q37 and E48 have also been previously identified as important for the CII-AMPAR interaction based on the crystal structure of the AMPAR-

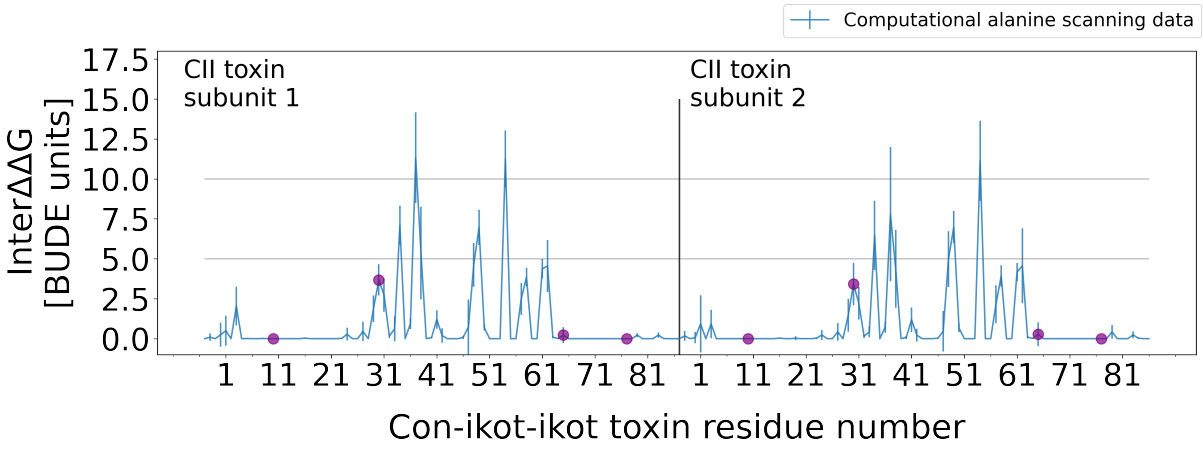

Figure 3.3: ΔΔG values from alanine scanning of WT CII toxin with AMPAR LBDs. CII lysine residues – K10, K30, K65, and K77 – are indicated by purple dots. Results shown as mean ± standard deviation.

CII complex, together with the C-terminal alanine A86. Its lack among the residues with top alanine scanning scores is not surprising as mutating it to an alanine residue would not produce any binding free energy change.

None of the lysine residues – K10, K30, K65, and K77 – displayed BUDE scores $\geq$ 5 units ($\geq$ 1 kcal/mol), therefore they can be considered neutral in terms of their contribution to the overall interaction and could be mutated to alanine without disrupting the binding between the toxin and AMPAR LBDs. Therefore, we proposed four CII lysine mutants:

- K10A K30A K77A – lysine residues except K65 mutated to alanine residues
- K10R K30R K77R – lysine residues except K65 mutated to arginine residues (preserving the overall neutral charge of the protein)
- K10A K30A K65A K77A – all lysine residues mutated to alanine residues
- K10R K30R K65R K77R – all lysine residues mutated to arginine residues (preserving the overall neutral charge of the protein).

To examine whether interactions between CII and the LBDs of AMPAR are disrupted in the proposed mutants, I carried out MD simulations of AMPAR ATD-LBD tetramer in complex with glutamate and each of the CII mutants as described in Section 2.1.1.2. I then assessed the quality of the resulting trajectories (quality control measure plots can be found in Figure E.1 in Appendix E) and after excluding trajectories which had not reached equilibration, I performed computational alanine scanning on the remaining trajectories as described in Section 2.1.2. In addition, in order to investigate whether introducing lysine mutations would lead to unexpected flexibility of the toxin, I computed RMSF per residue for wild-type and mutant CII variants, as described in Section 2.1.1.3.

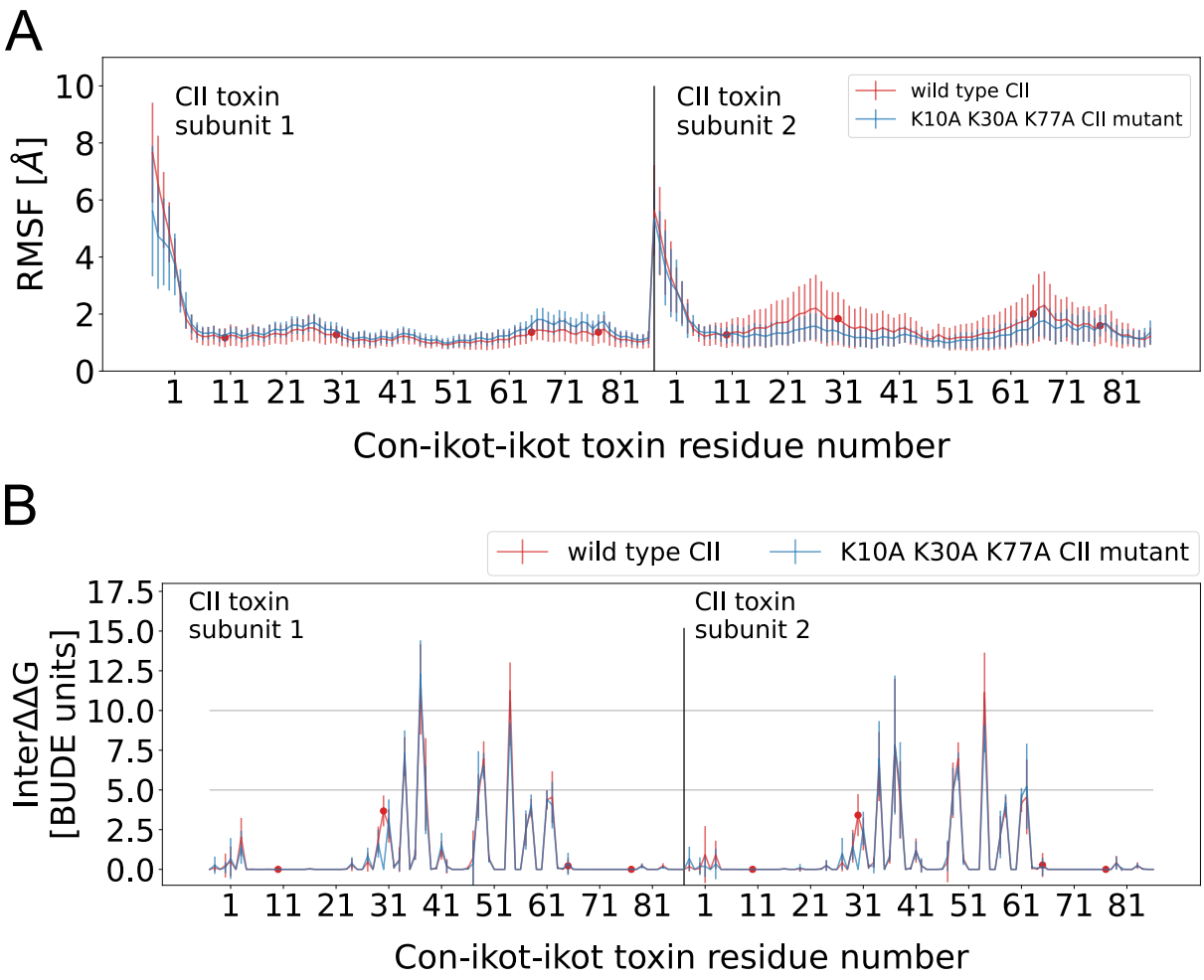

Figure 3.4: Results of RMSF per residue (A) and alanine scanning (B) analyses for WT CII toxin (red) and the triple lysine-to-alanine mutant K10A K30A K77A (blue). Results shown as mean ± standard deviation.

Figures 3.4 and 3.5 show results for the triple lysine-to-alanine mutant (K10A K30A K77A) and quadruple lysine-to-alanine mutant (K10A K30A K65A K77A), respectively. The results for both lysine-to-arginine mutants can be found in Figures E.2 and E.3 in Appendix E.

The results for all proposed mutants were similar: both the RMSF plots (Figures 3.4 A, 3.5 A, E.2 A, and E.3 A) and the alanine scanning plots (Figures 3.4 B, 3.5 B, E.2 B, and E.3 B) follow the same trends for the WT and mutant CII toxin variants. The exception is the alanine scanning results for residue K30, displaying a weak positive contribution to the overall energy of the interaction between the toxin and AMPAR, which is lost when the lysine residue is mutated to an alanine (Figures 3.4 B and 3.5 B).

Overall, these results suggest that of the four lysine mutants proposed for CII toxin, provided that they fold to the same overall shape as the wild-type toxin, all are expected to exhibit similar binding to AMPAR as WT CII and not to display excessive mobility of any of the regions of the protein. Therefore, producing them could be pursued as a potentially effective way of ensuring

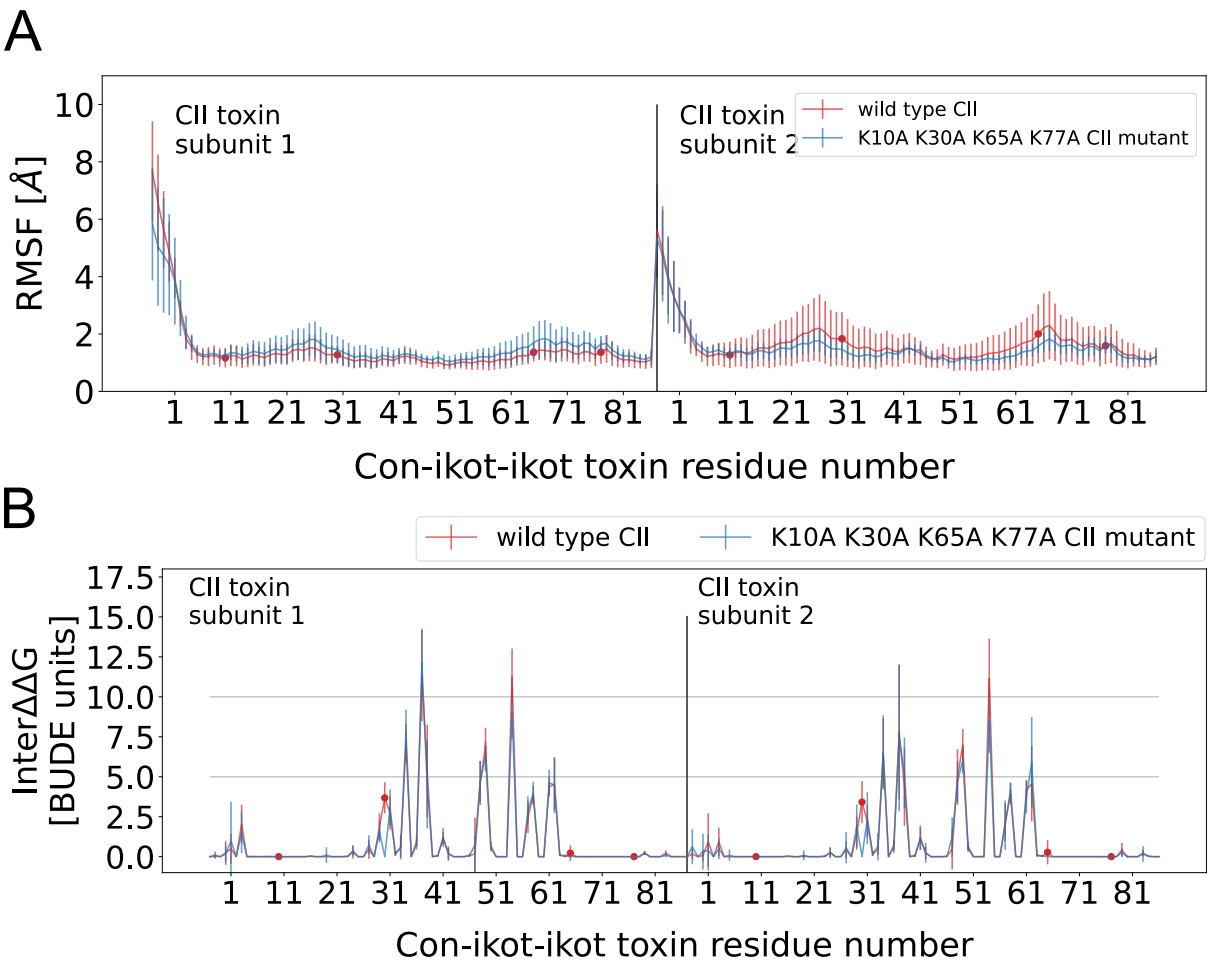

Figure 3.5: Results of RMSF per residue (A) and alanine scanning (B) analyses for WT CII toxin (red) and the quadruple lysine-to-alanine mutant K10A K30A K65A K77A (blue). Results shown as mean ± standard deviation.

labelling with the fluorescent dye at a more limited number of conjugation sites as compared to the wild-type CII.

3.1.3 AMPAR GluA2 homotetramer in complex with fluorescently labelled WT and mutant CII

Following the findings of the alanine scanning analysis of CII lysine mutants showing that they could bind to AMPAR in a similar fashion as the wild-type toxin, I expanded the simulation trajectory dataset further by including PA-JF 549 in the simulated system. The following CII variant - dye combinations were simulated, all in complex with AMPAR ATD-LBD tetramer:

- triple lysine-to-alanine mutant K10A K30A K77A
  - labelled at G-3 (N-terminus)
  - labelled at K65

  - labelled at both G-3 and K65

- quadruple lysine-to-alanine mutant K10A K30A K65A K77A - labelled at G-3
- triple lysine-to-arginine mutant K10R K30R K77R
  - labelled at G-3
  - labelled at K65
  - labelled at both G-3 and K65
- quadruple lysine-to-arginine mutant K10R K30R K65R K77R - labelled at G-3.

In addition, a simulation set of fully labelled (i.e. at G-3, K10, K30, K65, and K77) wild-type CII in complex with the AMPAR ATD-LBD tetramer in order to establish whether the presence of ten residues of PA-JF 549 protruding from the toxin's surface (Figure 3.2 D) could be accommodated by the system or whether they would introduce excessive bulk and prevent the toxin from being able to continue interacting with the receptor. It is important to note here that the simulated system includes the toxin positioned in its binding site and assumes that the interaction is formed in the first place, which may not be the case due to the presence of linkers connecting the ATD and LBD layers of AMPAR and being in the way of the toxin reaching its destination.

The quality control plots for all simulations of AMPAR ATD-LBD tetramer in complex with glutamate and labelled CII – WT and mutant – can be found in Appendix F. A visual assessment of randomly selected equilibrated trajectories from each simulation set suggests that the dye bound at the N-terminus of CII subunits and/or lysine residues, is well-tolerated by the AMPAR-CII complex and does not lead to an unbinding of the toxin from the receptor within the timeframe of the simulation. Even the fully-labelled CII toxin with ten dye residues attached to its surface remained stable in its binding site throughout the simulation trajectory. This suggests that introducing mutations to the toxin in order to limit the label:protein ratio may be a step to consider in future investigations if after the labelling reaction the labelled toxin population consists of partially and fully-labelled toxin dimers. If labelling at some of the possible conjugation sites abolished the interaction between the toxin and AMPAR completely, perhaps less or even no mutations would be required to achieve predictable AMPAR labelling levels. Alternatively, if the labelling reaction efficiency is low, the majority of the toxin population after labelling may become labelled with only one or two dye molecules, again resulting in little to no need for genetic manipulation of the toxin in order to limit labelling.

The results of the MS analysis of a sample of WT CII toxin labelled with PA-JF 646 can be found in Section 3.3.1.3.

3.1.4 p53-MDM2

After running a full set of p53-MDM2 simulations, I plotted several quality control measures as described in Section 2.1.1.3. As seen in Figure 3.6, the potential energy and temperature of the simulated system, as well as the all-atom RMSD from the first frame of each trajectory all reach a plateau during the simulation time, together suggesting that the trajectories reached equilibrium and can therefore be used for further analyses (Section 3.2.1). For the purpose of downstream analyses, I decided to treat frames 50–200 (to the right of the grey dashed line in Figure 3.6 A, B, and C) as the equilibrated portion of the simulation as all three measures used to determine equilibration reach a plateau in this section across trajectories.

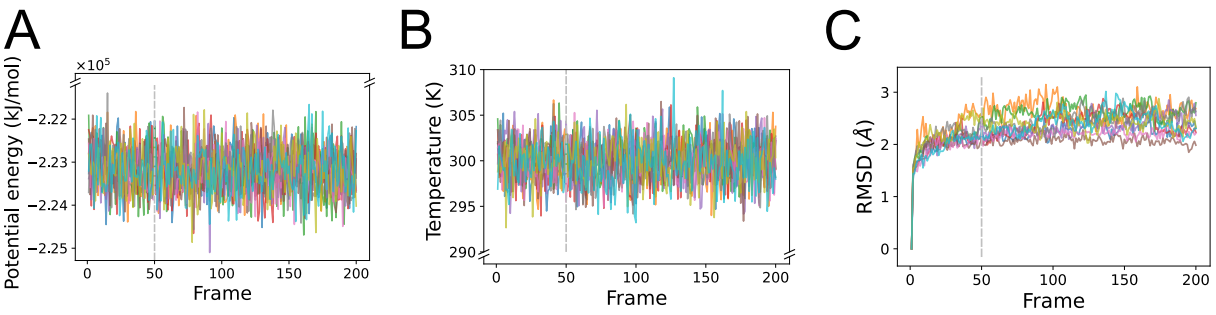

Figure 3.6: Quality control measures over the course of simulation – p53-MDM2 system. A. Potential energy. B. Temperature. C. RMSD. The grey vertical lines show Frame 50, which was taken as the beginning of the equilibrated portion of the simulations.

3.2 Network analysis

3.2.1 p53-MDM2

In order to investigate the interactions between p53 and MDM2, I performed computational alanine scanning on frames extracted from the equilibrated portion of the simulation trajectories, as described in Section 2.1.2, and applied NAppEd to the entire equilibrated portion of the trajectories as described in Section 2.1.3.2. The resulting meta-network plot is shown in Figure 3.7, together with selected network properties and counts of interaction types. The plots of each detected interaction type are shown in Figure 3.8.

The interaction network consists of one connected component (i.e. all nodes belong to one connected set), which is composed of 39 nodes (representing amino acid residues) and 88 edges between them (representing residue interactions). Of those 88, 7 edges represent interactions that are only present in one frame over the entire simulation set (weight 1), while 2 edges are present in the entire equilibrated portion of at least one simulation replicate (max_persistence 150) – a π-π stacking interaction between F19 of p53 and Y67 of MDM2, and a hydrogen

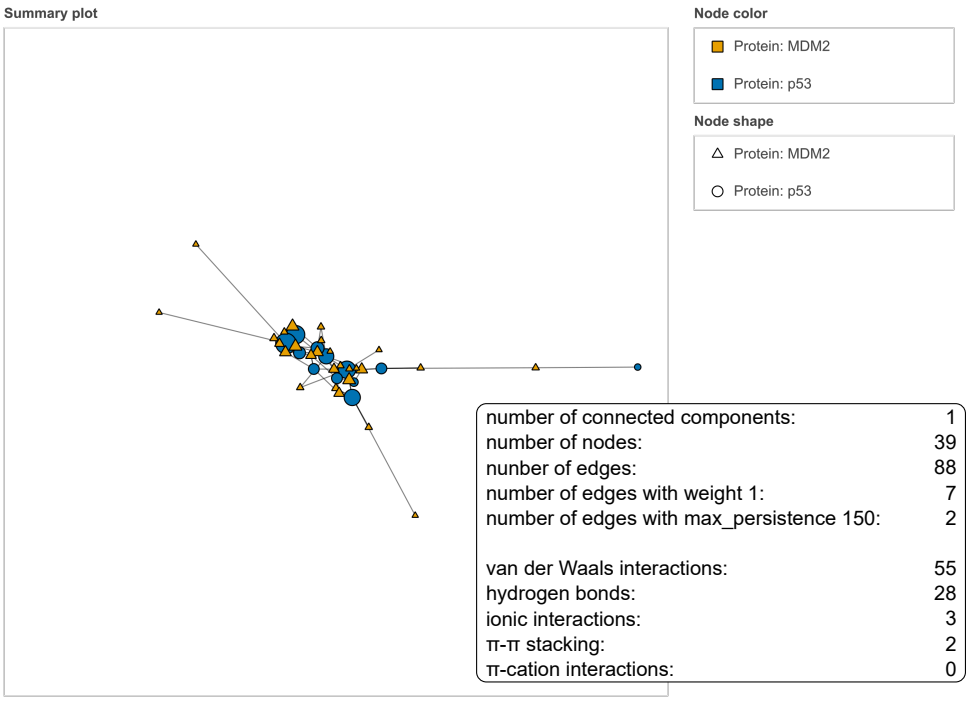

Figure 3.7: Meta-network of interactions between p53 and MDM2 with selected network properties and counts of interactions of each type shown.

bond between W23 of p53 and L54 of MDM2. The main interaction type in the network is van der Waals, followed by hydrogen bonds. The ionic interactions and π-π stacking are not as numerous in the network (Figure 3.7, Figure 3.8).

The results from computational alanine scanning and network analysis of the p53-MDM2 system (Figure 3.9 B) are generally in good agreement, and the top 4 residue set is the same for both analysis methods (as seen in Table 3.1). The top 5 residues according to the weighted degree ranking are shown on the p53-MDM2 system structure with their main interacting partners from MDM2 (Figure 3.9 A). Both of the interactions which showed very high persistence in at least one simulation replicate can be seen at the very top of the table (ranked 1 and 2 in both network analysis and alanine scanning terms).

The top-scoring p53 residues and their main MDM2 interactors (Table 3.1) agree well with data found in literature. The top three p53 residues – F19, W23, and L26 – had been identified as crucial for the interaction between p53 and MDM2 by structural, biochemical, and computational studies [239, 263, 252, 255, 264, 265] and the importance of the fourth ranked residue – L22 – has been established as well [252, 255]. A subset of the top MDM2 interactors have been highlighted as important for the interaction (V93, Y100 [255], H96 [265]). The significance of the hydrogen bond between p53's W23 and MDM2's L54 has also been underscored in several studies [239, 252, 264, 266]. Interestingly, the interaction between F19 and Y67, despite having appeared in literature before [265, 267], is not the main interaction described for p53 F19 – instead, the main interaction quoted in the studies is a hydrogen bond with Q72

[239, 252, 264, 266, 268]. This interaction is not absent from our p53-MDM2 interaction network; while it does not appear as the top interaction F19 engages in, it is still one of its main interactions (in fact, with weight 1168 and max_persistence 98, it is second or third from the top, depending on which measure is used to rank the interactions).

Table 3.1: Top 5 p53 interactors with MDM2. NA – network analysis. AS – Alanine Scanning

Rank (NA)	**Rank (AS)**	**Residue**	**Weighted degree (NA)**	**BUDE AlaScan score (AS)**	**Main interaction (NA)**	**Main interaction MDM2 partner**
1	2	F19	7207	18.2	π-π stacking	Y67
2	1	W23	3488	21.5	H-bond	L54
3	3	L26	2288	7.7	van der Waals	H96
4	4	L22	2231	4.0	van der Waals	V93
5	8	N29	2211	2.6	H-bond	Y100

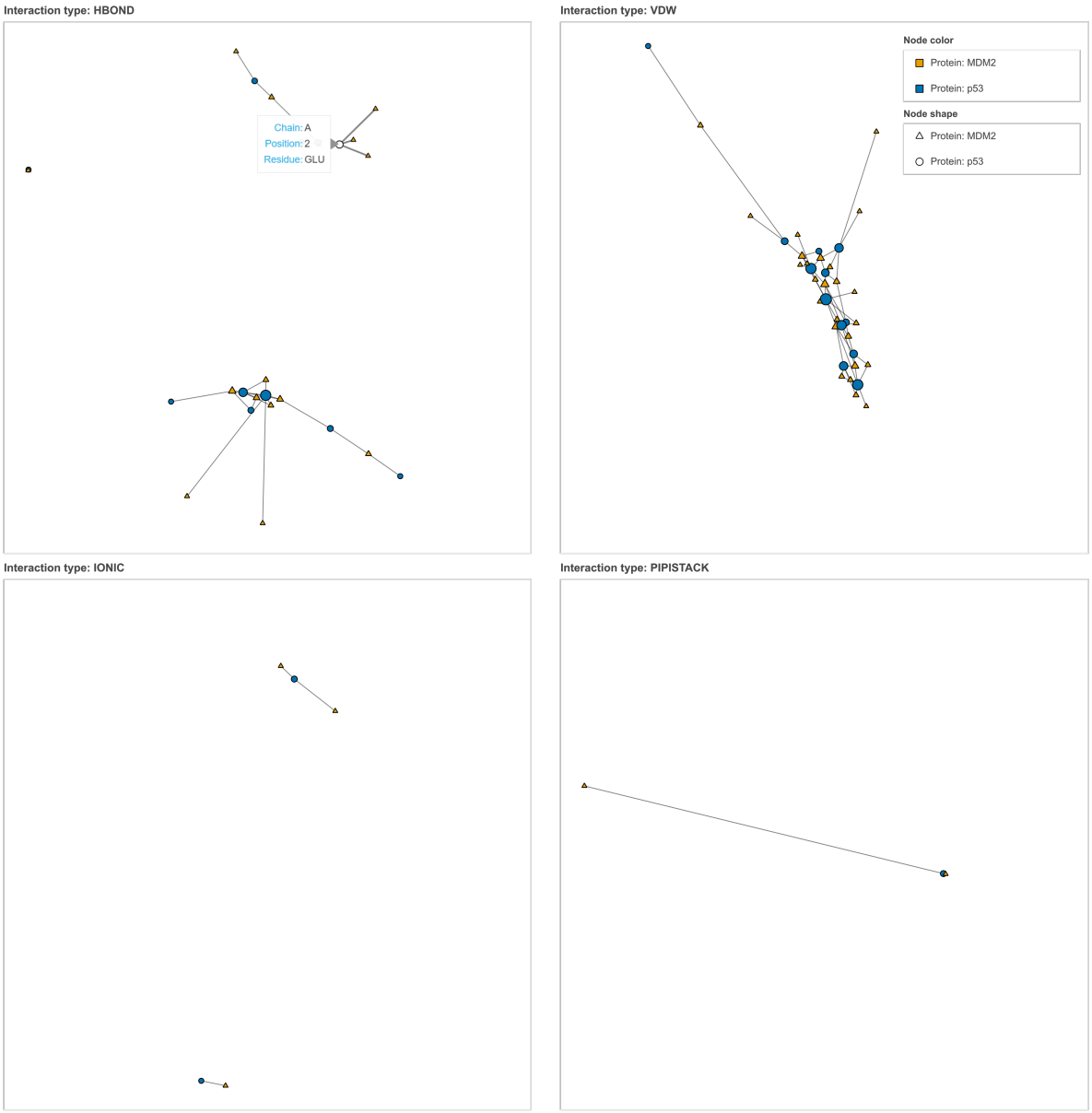

Figure 3.8: Meta-networks by interaction type for interactions between p53 and MDM2, showing also the information box which appears when the cursor is hovered over a node (A).

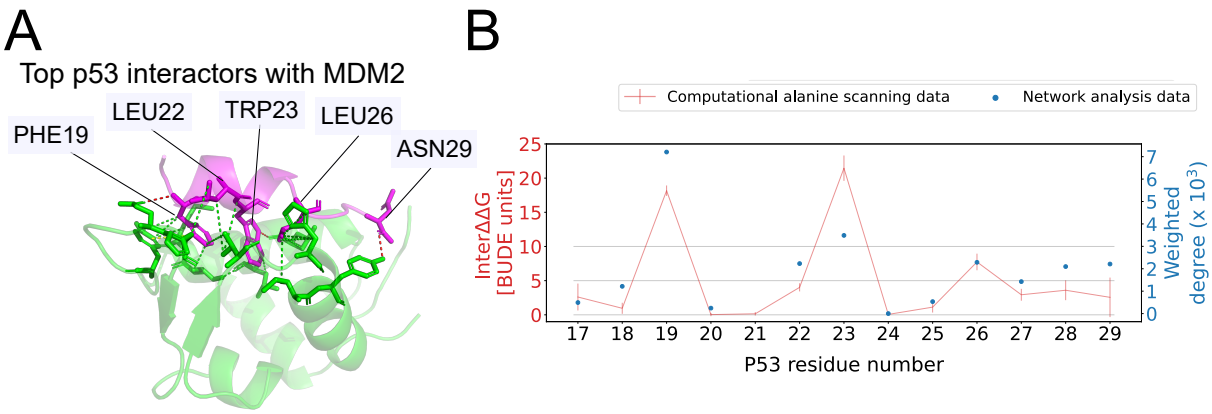

Figure 3.9: A. Top p53 residues interacting with MDM2. B. Weighted degree data from network analysis (blue) and $\Delta\Delta$G values (mean $\pm$ standard deviation) from BUDE alanine scanning (red) between p53 and MDM2. Grey lines indicate $\Delta\Delta$G values of 5 and 10 BUDE units (corresponding to 1 and 2 kcal/mol, respectively).

3.2.2 AMPAR GluA2 homotetramer in complex with WT CII

I performed computational alanine scanning on frames extracted from the equilibrated portion of the simulation trajectories, as described in Section 2.1.2 and applied NAppEd to the entire equilibrated portion of the trajectories as described in Section 2.1.3.2. I filtered the interactions to only include those between CII and AMPAR and isolated separate networks for CII interactions with the LBD and ATD layers of the receptor.

3.2.2.1 CII interactions with AMPAR LBDs

The meta-network summarising the interactions of CII with the LBD layer of AMPAR over the course of the simulation set is shown in Figure 3.10. The network is composed of 1 connected component, consisting of 168 nodes (residues) and 433 edges (interactions) between them. 51 of the edges represent interactions which are only present for one frame over the course of all simulation replicates (weight 1), while 10 of the edges represent interactions which were present for the length of the equilibrated portion of the simulation in at least one replicate (max_persistence of 150). The interaction network is dominated by van der Waals interactions and hydrogen bonds, with smaller contributions from ionic interactions, π-π stacking, and π-cation interactions.

The results of computational alanine scanning and network analysis of the interactions between CII and AMPAR LBDs (Figure 3.11 C) are in good agreement. The exception to this general trend is residue 86 in both CII subunits, which scores high in weighted degree (which summarises the number of interactions a residue forms with other residues throughout the simulation), but not in its computed energetic contribution to the overall interaction energy. This is an expected result, as residue 86 is an alanine and as such would not generate any energy difference when computationally replaced with an alanine residue.

I decided to investigate closer a subset of residues identified by network analysis as displaying the highest weighted degree scores. I ranked the residues included in the CII-LBD interaction network by weighted degree and plotted the ranking in a plot shown in Figure 3.11 B to determine a reasonable cut-off for number of residues to be included in the subset for further investigation (weighted degree results for top 20 residues can also be found in Table G.2 in Appendix G). Based on the plot, I selected the top 10 CII residues interacting with AMPAR LBDs (summarised in Figure 3.11 A).

The subset of 10 residues with the highest contributions to the interaction between CII and AMPAR LBDs according to NAppEd includes the same five residues from each CII toxin subunit – Gln37 (Q37), Glu48 (E48), Ile49 (I49), Tyr54 (Y54), and Ala86 (A86).

Compared to the results from alanine scanning, the top 10 (or even top 20) LBD interactors set identified by NAppEd does not contain F34, which ranked 5th/8th (for the two toxin sub-

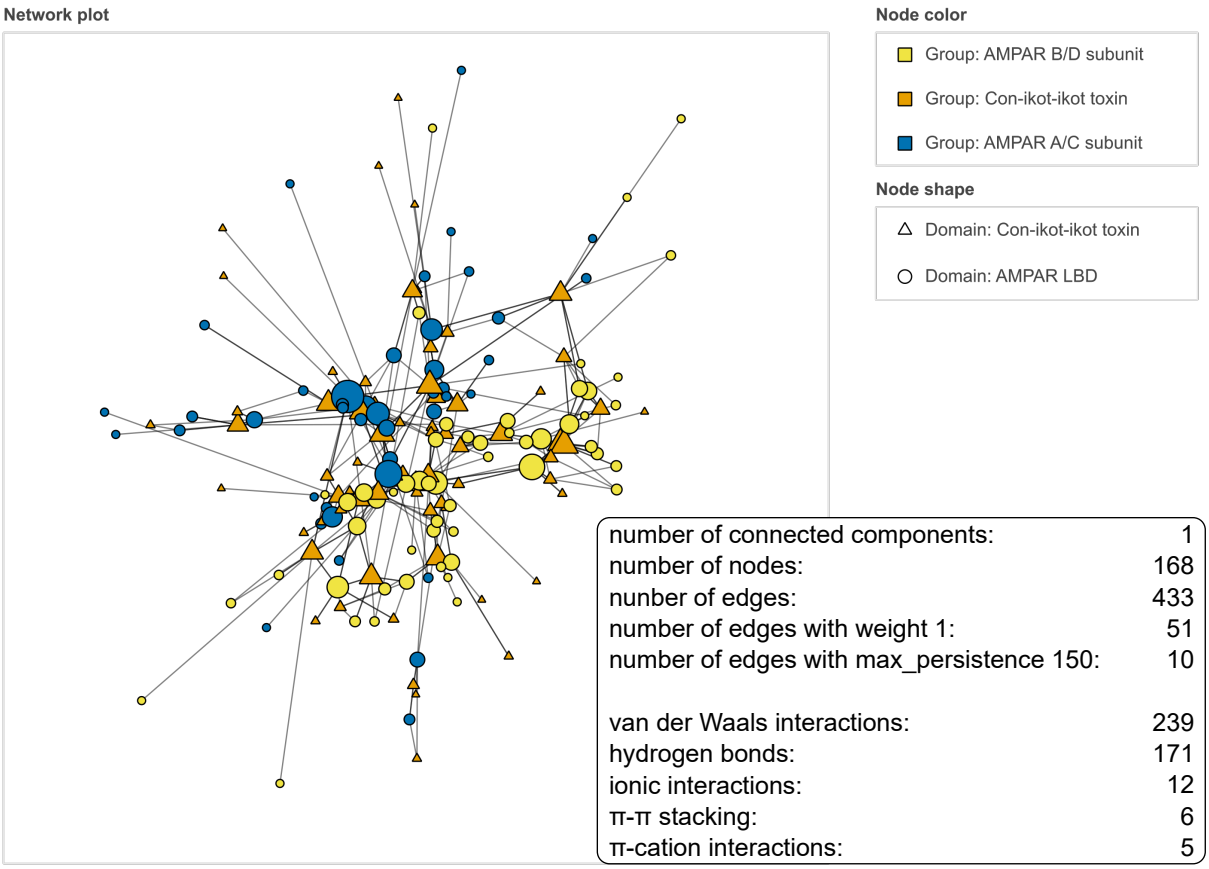

Figure 3.10: Meta-network of CII toxin interactions with the LBD layer of AMPAR. Box: selected meta-network properties and counts of each interaction type.

units) according to alanine scanning data (Tables G.1 and G.2). A factor which could contribute to the lack of F34 in the list of top LBD interactors by NAppEd is that in the dynamic system setting of the MD simulation, the interactions F34 engages in are typically relatively short-lived. The comparison of maximum persistence values for interactions formed by A86, E48, or Q37 with the values for interactions formed by F34 (Tables G.3, G.4, G.5, and G.6) reveals that while A86, E48, and Q37 all engage in some long-lived interactions (some of those lasting for the entire equilibrated portion of at least one simulation replicate, i.e. with max_persistence of 150), interactions formed by F34 exhibit low maximum persistence, ranging from 1 to 48 frames. This could explain why F34 could be ranked high based on its energy contributions detected by alanine scanning of a small number of frames, but not based on the number of interactions detected by the analysis of 50 times more frames with NAppEd.

My analysis recapitulates all three toxin residues previously identified as crucial to the interaction between the toxin and AMPAR – Q37, E48, and A86; and reveals novel interacting residues – I49 and Y54 – not recognised by the structural study. Interestingly, while the main interactors identified by NAppEd for E48 and A86 match those suggested based on the crystal structure (A/C subunit R660 for E48, and B/D subunit K752 for A86), the main interactors for

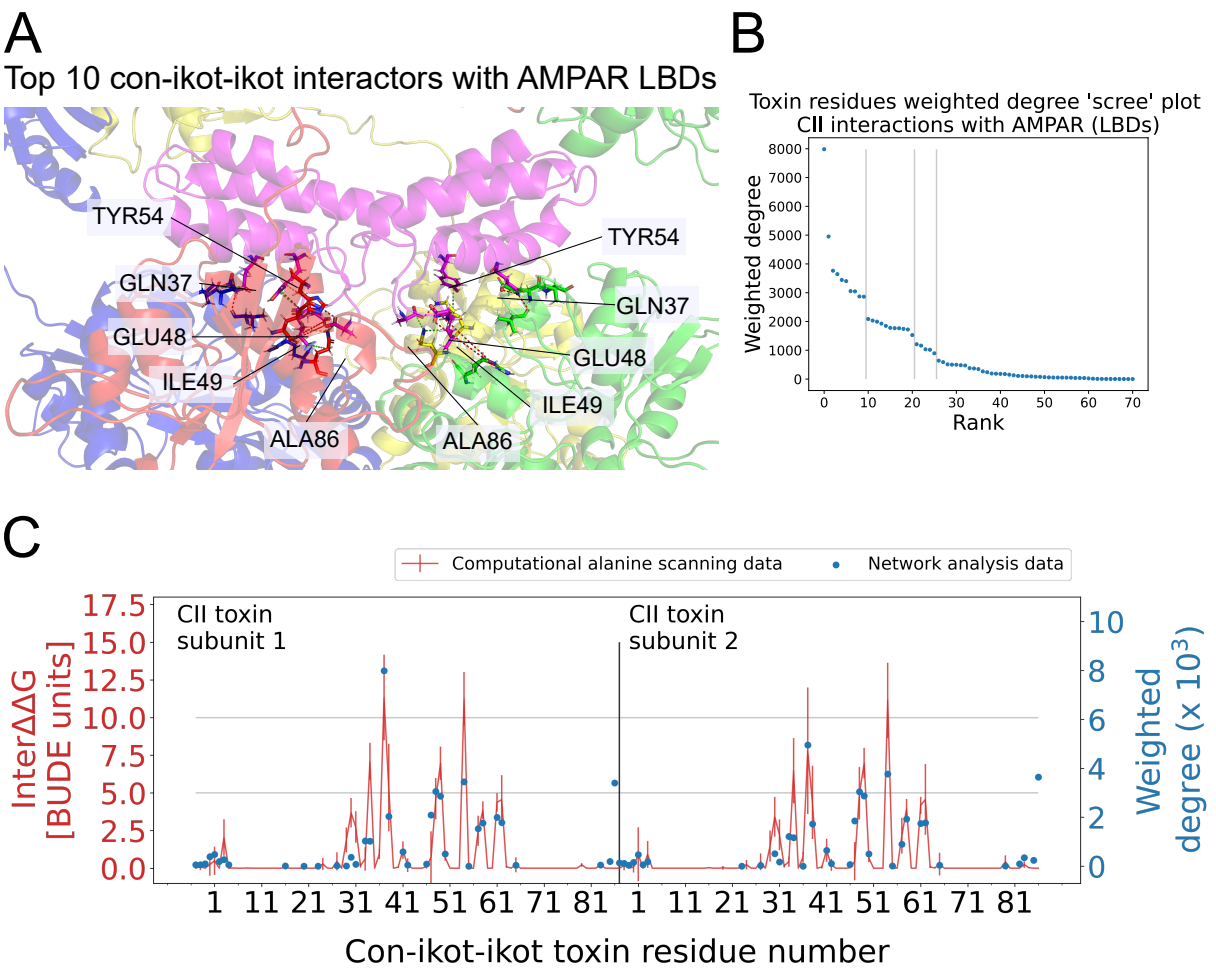

Figure 3.11: A. Top 10 CII residues interacting with the LBD layer of AMPAR. B. "Scree" plot indicating weighted degree ranking of all nodes (residues) in the CII-LBD network. C. Weighted degree data from network analysis (blue) and ΔΔG values (mean ± standard deviation) from BUDE alanine scanning (red) between CII and AMPAR LBDs. Grey lines indicate ΔΔG values of 5 and 10 BUDE units.

Q37 do not (while the crystal structure paper points at A/C subunit R453, the network analysis identifies E484 in subunit A and V481 in subunit C). Both AMPAR residues – E484 and V481 – are present in the 4U5C and 4U5D crystal structures [151] within close proximity to Q37, therefore they could have been identified as important contacts based on the crystal structures. It is possible that the dominance of their interactions with Q37 in the NAppEd analysis over those with R453 is the result of R453 and CII Q37 side chains positioning themselves in a position less favourable for the interaction between them during the course of the simulation. This idea seems to be supported by the maximum persistence values of 142-150 for both the Q37-E484 and Q37-V481 interactions, but only up to 71 for the interactions of Q37 with R453 (Table G.5).

In order to validate the findings of this analysis of interactions between CII and AMPAR LBDs, we decided to express and purify a CII mutant in which Y54 is mutated to alanine

(Y54A) as Y54 ranked high according to both alanine scanning and network analysis results. According to my results, this mutation would result in a weakened interaction between Y54A CII and AMPAR LBDs, which could lead to changes in the functional properties of the toxin. The results of experimental validation of my computational analysis are described in Section 3.3.

3.2.2.2 CII interactions with AMPAR ATDs

The meta-network summarising the interactions of CII with the ATD layer of AMPAR over the course of the simulation set is shown in Figure 3.12. The network is composed of 1 connected component, consisting of 103 nodes (residues) and 305 edges (interactions) between them. 35 of the edges represent interactions which are only present for one frame over the course of all simulation replicates (weight 1), while 5 of the edges represent interactions which were present for the length of the equilibrated portion of the simulation in at least one replicate (max_persistence of 150). Similarly to the network of CII interactions with the AMPAR LBDs, the interaction network is dominated by van der Waals interactions and hydrogen bonds, with smaller contributions of ionic interactions; however, in this case, no π-π stacking or π-cation interactions were detected.

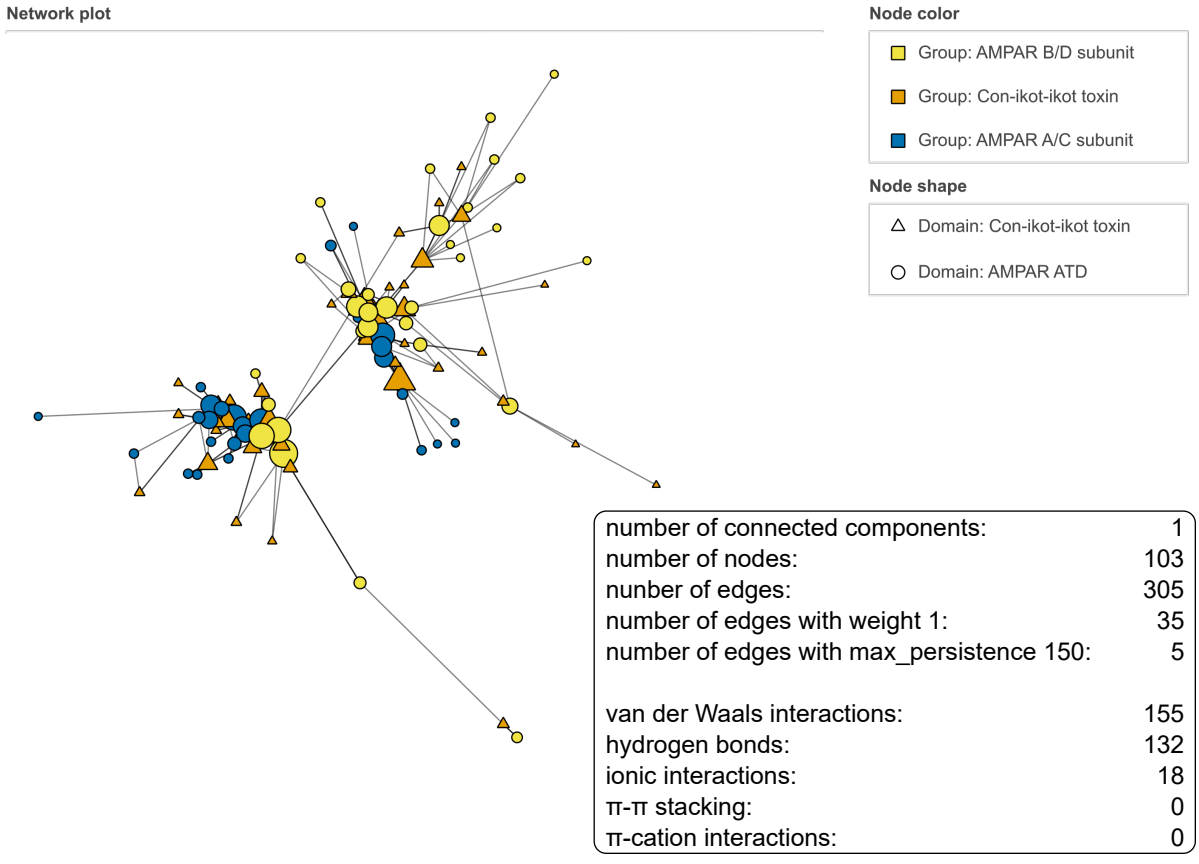

Figure 3.12: Meta-network of CII toxin interactions with the ATD layer of AMPAR. Box: selected meta-network properties and counts of each interaction type.

Similarly as in the case of CII interactions with AMPAR LBDs, the computational alanine scanning data and network analysis data show good agreement for CII interactions with AMPAR ATDs (Figure 3.13 C). As expected, the interactions with this domain layer are not as pronounced as those with the ligand-binding domain layer of the receptor, which can be seen by comparing Figures 3.13 C and 3.11 C, which were both plotted with the same scales on the y-axes.

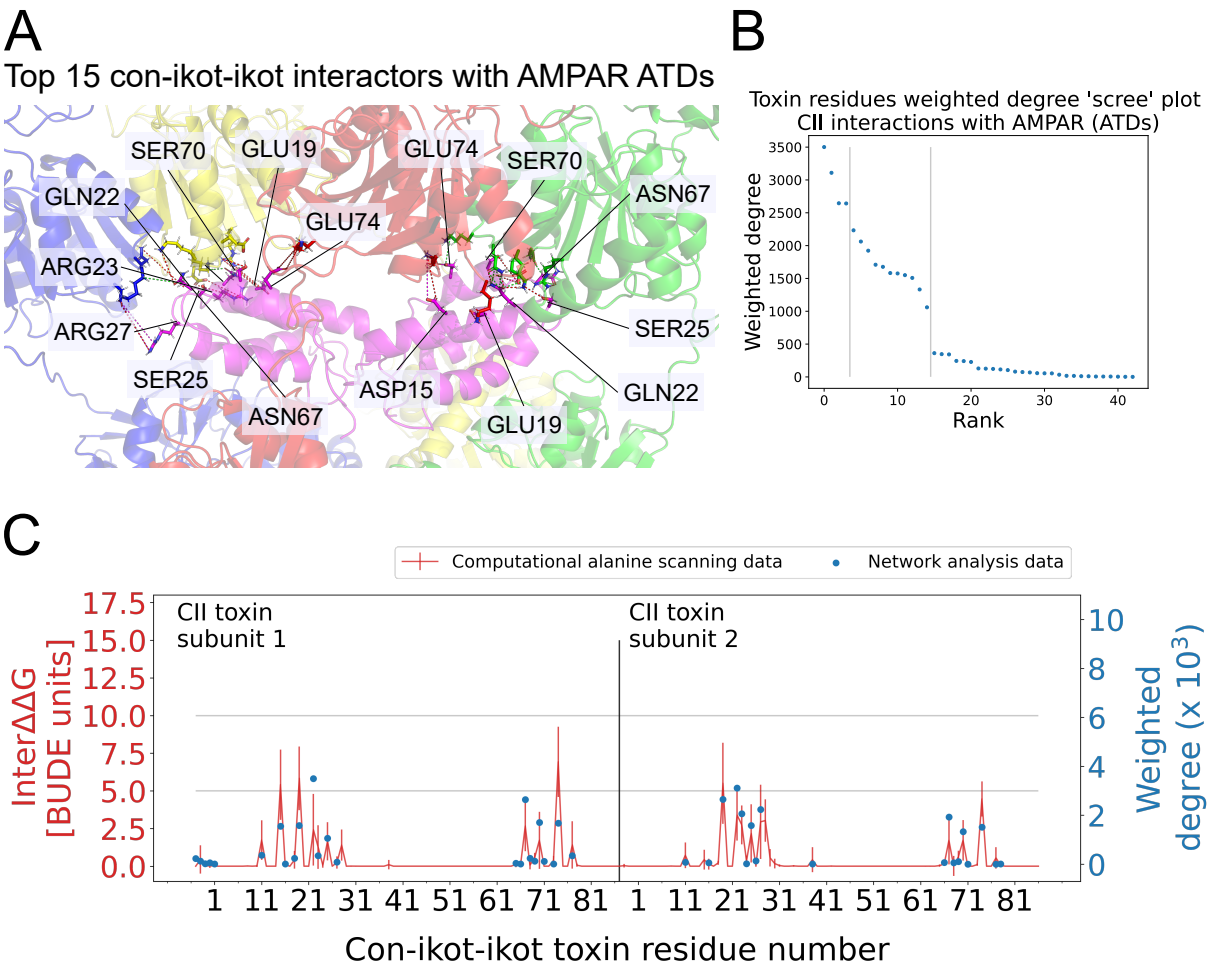

Figure 3.13: A. Top 15 CII residues interacting with the LBD layer of AMPAR. B. Scree plot indicating weighted degree ranking of all nodes (residues) in the CII-ATD network. C. Weighted degree data from network analysis (blue) and ΔΔG values (mean ± standard deviation) from BUDE alanine scanning (red) between CII and AMPAR ATDs. Grey lines indicate ΔΔG values of 5 and 10 BUDE units (corresponding to 1 and 2 kcal/mol, respectively).

As with the CII interactions with the AMPAR LBDs, I ranked the toxin residues included in the toxin-ATD interaction network by their weighted degree and selected the number of top residues to focus on based on the plot to be 15 (Figure 3.13). The top 15 interactors with AMPAR ATDs, when taking into account alanine scanning results (Table H.1), or network analysis (Table H.2) include mostly the same set of residues, though the ranking varies between the two methods, which may be in part due to the lack of interaction energy information in

NAppEd analyses, and/or due to the more dynamic system ”seen” by the NAppEd analysis as compared to alanine scanning. A residue which has ranked high by both methods is E19 (2/3 by alanine scanning and 3/10 by network analysis).

Interestingly, when considering the top CII interactors with AMPAR ATDs and their main interaction partners (Table H.2), it appears that overall, with the top 15 residues in this set, the toxin makes contacts with all four AMPAR subunits (A–D). This is a promising finding which could open up a door for the development of CII-based probes with specificity for different AMPAR subunit compositions.

Table 3.2 shows the main AMPAR ATD interactors (as seem in Table H.2) of the top 15 CII residues found to form interactions with this AMPA receptor domain layer. While some of these residues show high similarity between the GluA1-4 (D127, E181), others could be utilised for targeting with molecular probes (K128, K153). It is also important to remember that harnessing the interactions between CII toxin and AMPAR ATDs could involve multiple approaches, including shifting the main interaction hotspots to other residues, less conserved across AMPAR subunit types, while weakening/abolishing stronger interactions with residues which may be more conserved.

Construct	**Residues**						
GluA2 (rat/human)	**D127**	**K128**	**K153**	**Q155**	**E181**	**R187**	**K212**
GluA1 (rat)	Q	T	N	Q	E	L	I
GluA1 (human)	Q	K	N	Q	E	L	I
GluA3 (rat/human)	E	K	N	Q	D	R	R
GluA4 (rat/human)	N	C	G	H	D	K	K

Table 3.2: Conservation of the top interactors (AMPAR ATD residues) of the top 15 CII residues found to form interactions with AMPAR ATDs. GluA2 is shown on the top as it was the construct used in the simulations carried out for this thesis. Residue numbering according to 4U5D [151].

3.3 Experimental validation of computational analyses

3.3.1 Wild-type CII

3.3.1.1 Purification

The process of producing wild-type CII toxin involved four rounds of protein expression as described in Section 2.2.1 (48 l of main culture in total), each followed by a StrepTactin chromatography protocol (StrepTactin 1–4). Fractions from StrepTactin runs were pooled in two rounds (StrepTactin 1+2 and 3+4), and all the samples were pooled together into one sample

before applying the ion exchange and SEC protocols. All stages of protein purification were carried out as described in Section 2.2.2.

StrepTactin affinity chromatography

Figure 3.14 shows the chromatogram UV absorbance peaks over eluted volume (A) as well as SDS-PAGE gels of peak fractions from StrepTactin chromatography runs 1–4 (D–G). Peaks from chromatography runs 2–4 are in good agreement with each other and with those observed in previous purifications of WT CII in our lab, while the StrepTactin 1 peak seems to correspond to a different elution volume. In fact, the visual assessment of the 96-well plate in which fractions were collected, revealed that despite desired fraction volume set to 2 ml, only fractions C1 and later were full-volume fractions, while fractions A1–A12 appeared to be around 1/3 of the set volume, and fractions B1–B12 appeared to be around 1/2 of the set volume. Taking this into consideration (Figure 3.14 C), the amended peak (Figure 3.14 B) looks as expected.

Sample concentration and buffer exchange

StrepTactin 1 fractions B4–C12 and StrepTactin 2 fractions A1–A10 were pooled together and concentrated as described in section 2.2.2. The total volume of pooled fractions was ∼44 ml and the measured protein concentration was 1.0 mg/ml, resulting in a total protein content of 44 mg. Table 3.3 shows the measured protein concentration values for concentrate and flow-through following each spin in the process of concentrating the pooled fractions. The recovered concentrate volume was ∼2 ml, resulting in a total of 24 mg of protein in the concentrated fraction after all spins.

Table 3.3: Protein concentrations (mg/ml) in concentrate and flow-through after spins of pooled StrepTactin 1 and StrepTactin 2 fractions.

Spin	**Time** (min)	**Protein concentration (concentrate)** (mg/ml)	**Protein concentration (flow-through)** (mg/ml)	**Approximate flow-through volume** (ml)
1	15	1.1	0.3	8
2	25	1.5	0.4	11.5
3	15	1.8	0.4	6.5
4	25	3.1	0.5	8.5
5	15	5.6	0.5	4.5
6	25	12.0	0.6	2.5

Similarly, StrepTactin 3 and 4 fractions A3–B2 were pooled together and concentrated. The total volume of pooled fractions was ∼48 ml and the measured protein concentration was 1.4

A

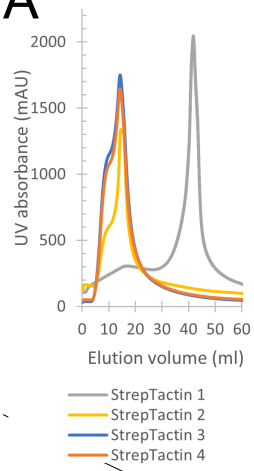

B

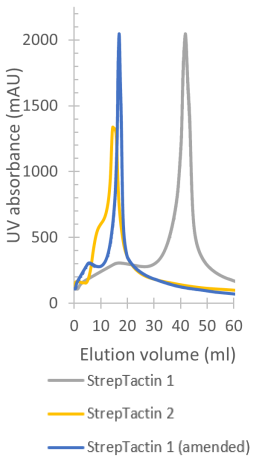

C

$$g(x) = \text{(amended peak)} \begin{cases} f(3x) & x < 8 \\ f(2x+8) & 8 \le x < 20 \\ f(x+28) & x \ge 20 \end{cases}$$

$$f(x) = \text{(original peak)} \begin{cases} g(x/3) & x < 24 \\ g((x/2)-4) & 24 \le x < 48 \\ g(x-28) & x \ge 48 \end{cases}$$

D

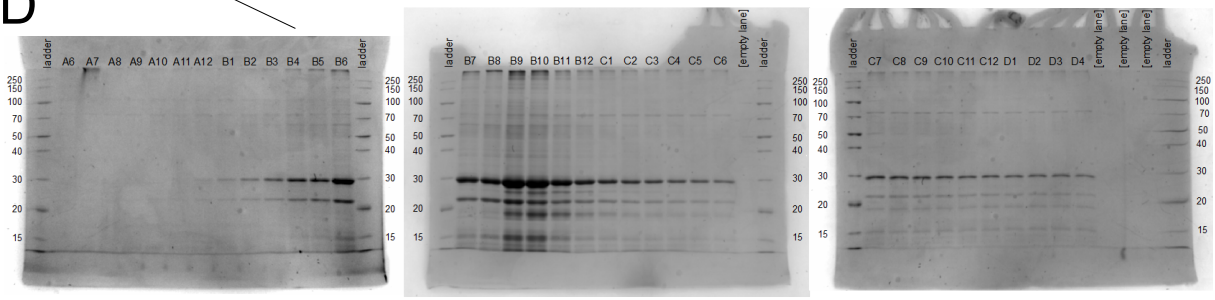

E

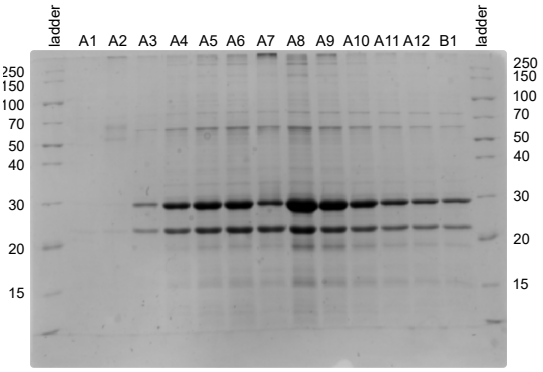

F

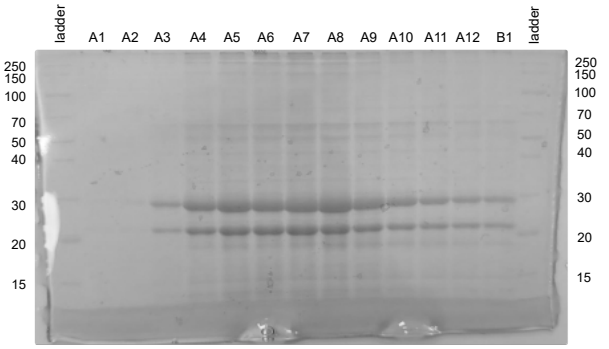

G

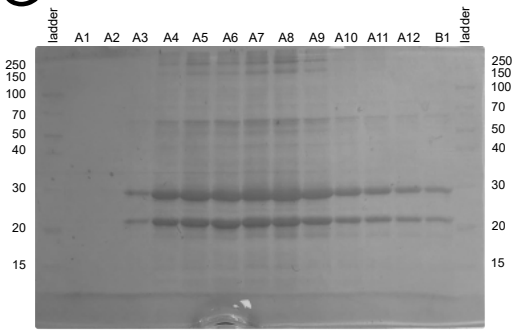

Figure 3.14: Wild-type CII purification. StrepTactin runs 1–4. A. Peak UV absorbance in all StrepTactin runs over eluted volume. B. StrepTactin 1 peak amended according to observed volumes of fractions A1–B12. StrepTactin 2 peak included for comparison. C. Relationship between UV absorbance trace in original vs amended StrepTactin 1 peak. D, E, F, G. SDS-PAGE gels of peak fractions from StrepTactin 1–4 (respectively).

mg/ml, resulting in a total protein content of 67.2 mg. Table 3.4 shows the measured protein concentration values for concentrate and flow-through following each spin in the process of concentrating the pooled fractions. The recovered concentrate volume was ∼1.5 ml, resulting in a total of 54.2 mg of protein in the concentrated fraction after all spins.

Table 3.4: Protein concentrations (mg/ml) in concentrate and flow-through after spins of pooled StrepTactin 3 and StrepTactin 4 fractions.

Spin	**Time** (min)	**Protein concentration (concentrate)** (mg/ml)	**Protein concentration (flow-through)** (mg/ml)	**Approximate flow-through volume** (ml)
1	15	1.7	0.1	7.5
2	25	2.1	0.1	9.5
3	15	2.7	0.1	5.5
4	25	3.9	0.1	8
5	15	5.5	0.1	4
6	25	11.4	0.1	6
7	25	36.1	0.2	3.5

Following the methanol precipitation and buffer exchange protocol, the protein concentration of the final 2 ml sample from StrepTactin 1+2 was 0.5 mg/ml (1 mg of protein), and the protein concentration of the final 2 ml sample from StrepTactin 3+4 was 0.6 mg/ml (1.2 mg of protein), resulting in a total of 2.2 mg of protein.

Ion exchange chromatography

Figure 3.15 shows the UV absorbance peak over eluted volume from ion exchange chromatography of wild-type CII (A) and a silver-stained SDS-PAGE gel of corresponding fractions. As reducing sample buffer was mistakenly used in place of non-reducing sample buffer, the observed bands would not represent dimeric CII, but rather CII monomers. However, the prominent bands are present at the correct molecular weight expected for monomeric CII (∼10 kDa).

Based on the chromatogram, I pooled fractions B10–B12 (elution volume 21–24 ml) and prepared the sample for size exclusion chromatography as described in Section 2.2.2. The measured protein concentration of the final ∼250 µl sample was 4 mg/ml, which corresponds to ∼1 mg of protein.

Size exclusion chromatography

Figure 3.16 shows the UV absorbance peak over eluted volume from the size exclusion chromatography of wild-type CII (A), as well as a silver-stained non-reducing SDS-PAGE gel of

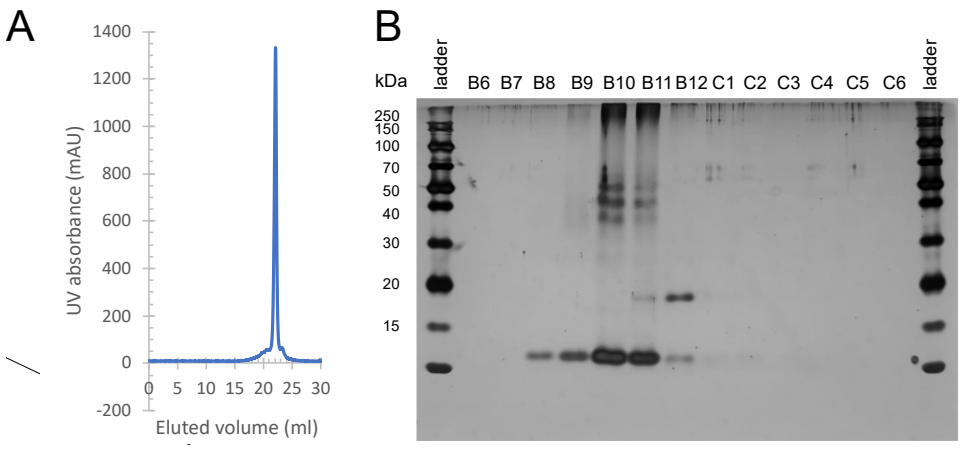

Figure 3.15: A. UV absorbance peak from WT CII ion exchange chromatography. B. Silver-stained SDS-PAGE gel of fractions corresponding to the UV absorbance peak. Reducing sample buffer was mistakenly used instead of non-reducing sample buffer, so the prominent band represents CII monomers.

fractions corresponding to the peak (B). The UV absorbance peak is in fact composed of the major peak centered around eluted volume 12 ml, and a much smaller peak to its right (i.e. at a lower eluted molecular weight). Based on the observations from previous purifications, we believe that the main peak corresponds to the dimeric CII. This is supported by the appearance of the major band in the non-reducing SDS-PAGE gel (indicated with magenta box in Figure 3.16 B), at eluted volumes which agree with the location of the main UV absorbance peaks in the chromatogram and expected molecular weight for CII dimer. As has been observed in previous purifications by our lab and others [151], despite the molecular weight of con-ikot-ikot being $\sim$20 kDa, it travels at a higher apparent molecular weight in SDS-PAGE, and the bands are not well-resolved but rather considerably smeared. The appearance of the presumed dimeric CII band in the SDS-PAGE gel (magenta box in Figure 3.16 B) is consistent with both of these observations.

I measured protein concentration in size exclusion chromatography fractions shown in Figure 3.16 B. The measured values can be found in Table 3.5 and as the volume of each fraction was 0.5 ml, the total protein across fractions B1–B4 (dimeric toxin peak fractions of high enough protein concentration that they could be used for downstream experiments) is around 413 µg, which is consistent with yields from previous purifications in our lab (40–100 µg per 12 l of bacterial culture [63]).

3.3.1.2 Functional characterisation

Following a successful purification of con-ikot-ikot, we tested its activity in macroscopic recordings as described in Section 2.2.4. The electrophysiology experiment confirmed the purified toxin's dose-dependent inhibition of AMPAR desensitization under prolonged exposure to full

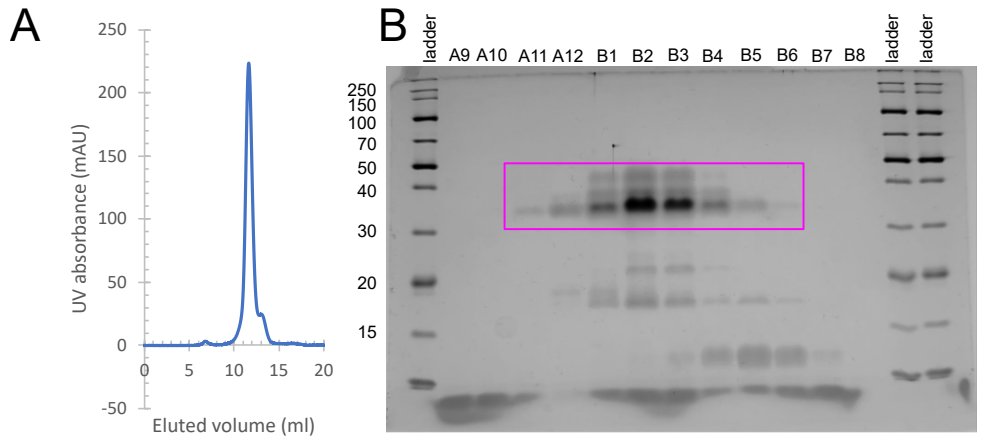

Figure 3.16: A. UV absorbance peak from WT CII size exclusion chromatography. B. Silver-stained non-reducing SDS-PAGE gel of fractions corresponding to the UV absorbance peak. Magenta box indicates the position of presumed CII dimer band.

Table 3.5: Protein concentrations (µg/ml) in WT CII toxin size exclusion chromatography fractions A9–B8.

Fraction number	**Protein concentration** (µg/ml)	**Fraction number**	**Protein concentration** (µg/ml)
A9	10	B3	259
A10	2	B4	102
A11	8	B5	26
A12	25	B6	46
B1	113	B7	14
B2	351	B8	4

agonist glutamate (Figure 3.17) with an EC_{50} of 1.7 $\pm$ 1 nM (n = 3–5 patches).

3.3.1.3 Labelling with fluorescent dye

Next, we were interested in labelling the purified WT CII toxin with one of the fluorescent dyes we want to use for super-resolution imaging in future applications, PA-JF 646. We carried out the labelling protocol as described in Section 2.2.3. We then prepared a sample for mass spectrometry validation of labelling as described in Section 2.2.3. When the labelled sample was retrieved from storage in the cold room, a yellow-orange precipitate could be observed at the bottom of the tube. Based on mass spectrometry analyses of previous purifications, we understand this precipitate to contain only the unbound dye and no protein. Therefore, I took care not to disturb the precipitate and only take up liquid from above it for further analysis.

Figure 3.18 and Table 3.6 show the results of the mass spectrometry analysis. Only 12% of the toxin present in the sample appears to be labelled and where labelling has occurred, the

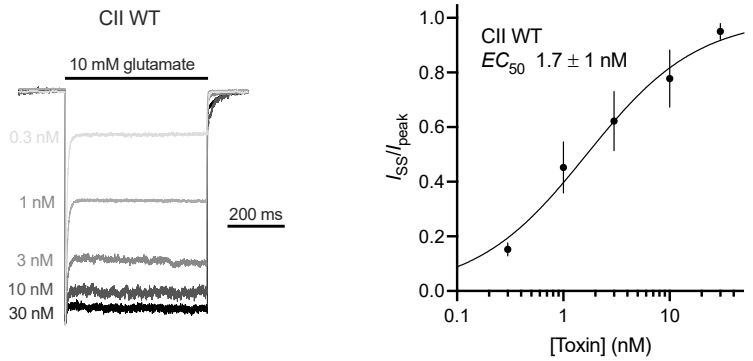

Figure 3.17: Left: GluA2 WT AMPA receptor current traces showing increasingly blocked desensitization as CII toxin concentration increases (0.3 nM – 30 nM). Right: dose-response curve of purified WT CII toxin. Activity of CII is expressed as desensitization block of GluA2 WT AMPA receptors (steady-state current (I_{ss}) over peak current (I_{peak})); n = 3–5 patches per concentration; error bars denote SEM.

dye:protein ratio was found to be 1:1 as only one peak representing toxin with substitutions is present and the mass difference between this peak and the fully-oxidised WT toxin peak points at only one copy of the dye bound to the protein.

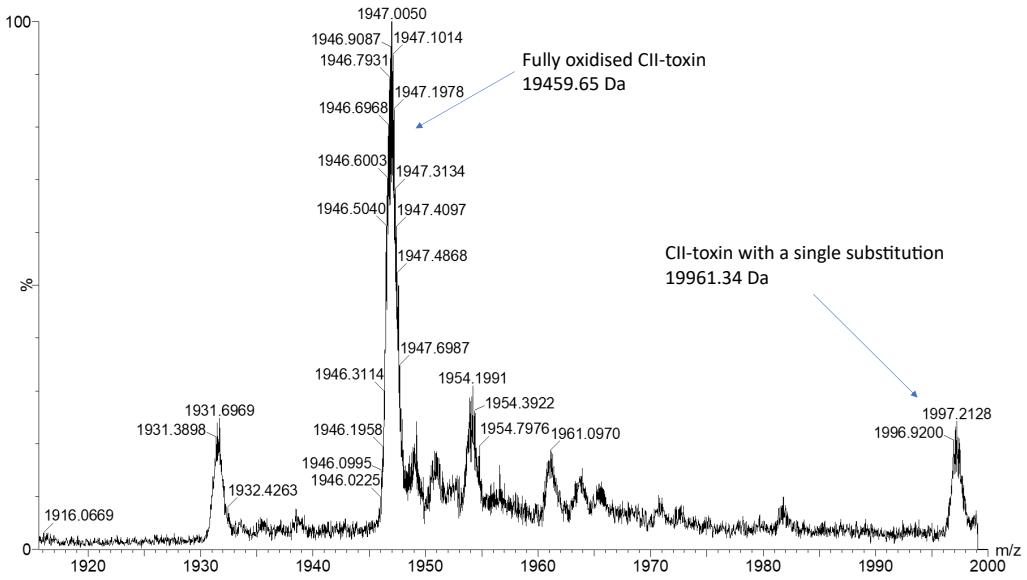

Figure 3.18: Mass spectrum of labelled WT CII toxin sample.

3.3.2 Y54A CII mutant

3.3.2.1 Purification

StrepTactin affinity chromatography

Figure 3.19 shows the chromatogram UV absorbance peaks over eluted volume (A) as well

Table 3.6: Mass spectrometry results – ratio of unlabelled vs labelled WCII toxin.

Protein	Area	Ratio
WT CII toxin (unlabelled)	20166.037	88%
WT CII toxin (labelled)	2673.029	12%

as SDS-PAGE gels of peak fractions from StrepTactin chromatography runs 1–4 (B–E). Peaks from all StrepTactin chromatography runs are in good agreement with each other and the appearance of the SDS-PAGE gels is similar to those of StrepTactin fractions from WT CII toxin purification (Figure 3.14 D–G).

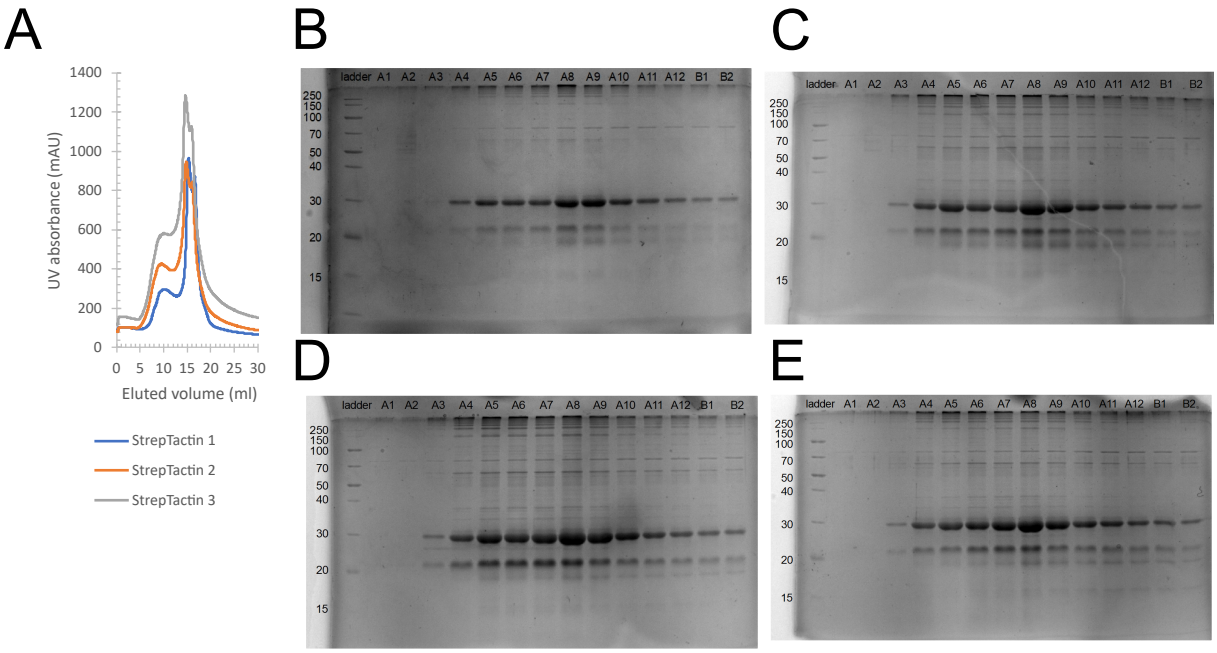

Figure 3.19: Y54A CII mutant StrepTactin runs 1–4. A. Peak UV absorbance in StrepTactin runs over eluted volume. B, C, D, E. SDS-PAGE gels of peak fractions from StrepTactin 1–4 (respectively).

Sample concentration and buffer exchange

StrepTactin 1+2 fractions A4–B2 were pooled together and concentrated for one round. The total volume of pooled fractions was 46 ml and the measured protein concentration was 0.4 mg/ml, resulting in a total protein content of 18.4 mg.

Similarly, StrepTactin 3+4 fractions A4–B2 were pooled together and concentrated for one round. The total volume of pooled fractions was 44 ml and the measured protein concentration was 0.8 mg/ml, resulting in a total protein content of 35.2 mg (53.6 mg in total between all StrepTactin 1–4 fractions A4–B2).

After the initial round of concentrating, all samples were pooled together and the process continued until the total volume of the concentrate was 3 ml.

Following the methanol precipitation and buffer exchange protocol, the protein concentration of the final 3 ml sample from StrepTactin 1–4 was 1.0 mg/ml, resulting in a total of 3 mg of protein.

Ion exchange chromatography

Figure 3.20 shows the UV absorbance peak over eluted volume from ion exchange chromatography of Y54A CII toxin mutant (A) and a silver-stained SDS-PAGE gel of corresponding fractions.

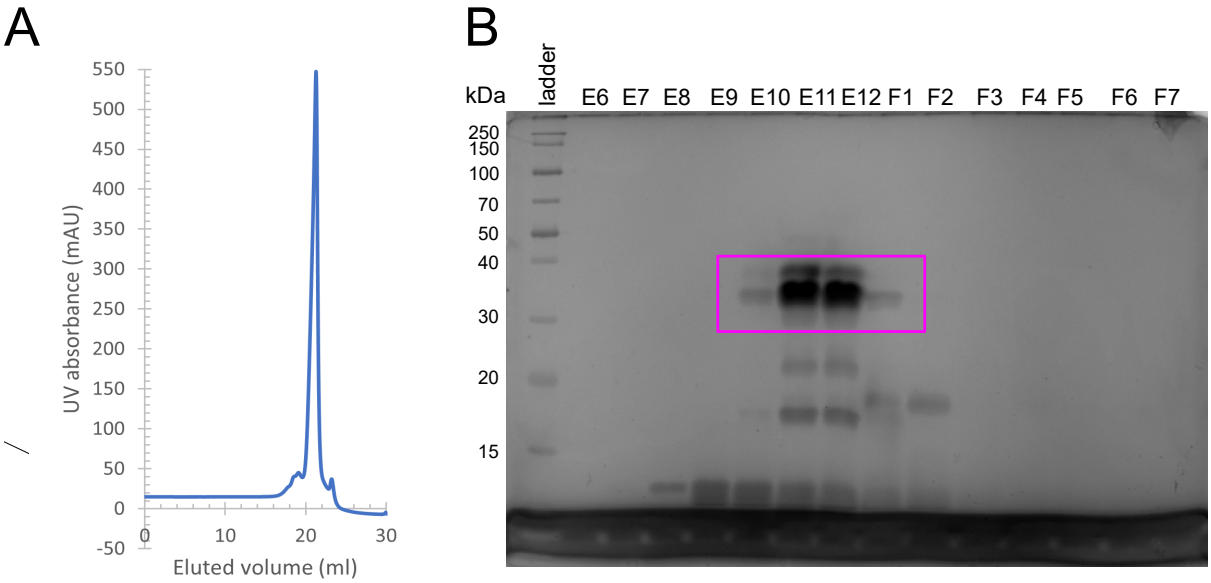

Figure 3.20: A. UV absorbance peak from Y54A CII ion exchange chromatography. B. Silver-stained non-reducing SDS-PAGE gel of fractions corresponding to the UV absorbance peak. Magenta box indicates presumed CII dimer band.

Based on the chromatogram, I pooled fractions E11–E12, exchanged buffer for SEC buffer, and concentrated them down to ∼300 µl and protein concentration of ∼ 3.5 mg. A 50 µ portion of this sample was used for labelling (see Section 3.3.2.3) and the rest was directly loaded onto the size exclusion chromatography column (see Section 3.3.2.1 below).

Size exclusion chromatography

Figure 3.21 shows the elution profile of unlabelled Y54A CII in size exclusion chromatography, as well as a silver-stained non-reducing SDS-PAGE gel of peak fractions. The presence of bands at the expected molecular weight for dimeric CII (which travels at a higher apparent molecular weight than its actual molecular weight of ∼20 kDa) confirms that our purification efforts were successful. The measured protein concentration values for fractions B1–B5 can be found in

Table 3.7.

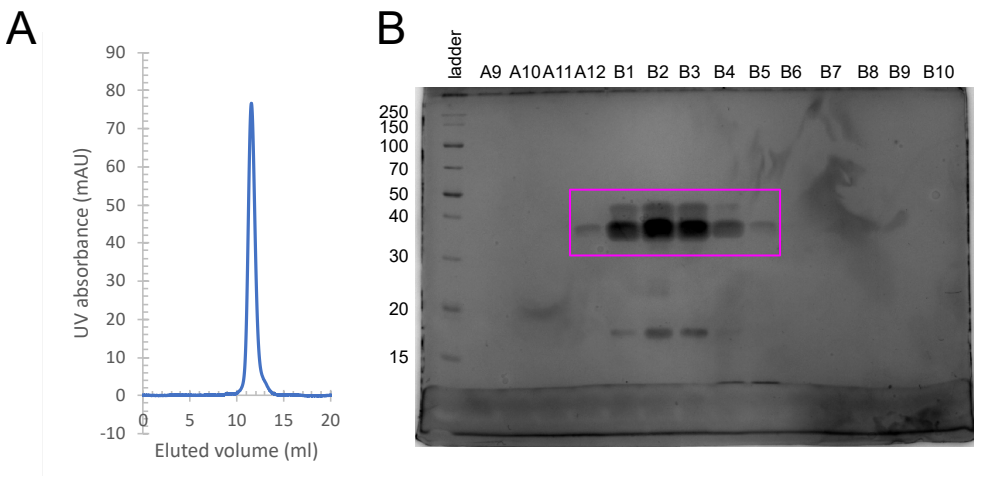

Figure 3.21: A. UV absorbance peak from unlabelled Y54A CII size exclusion chromatography. B. Silver-stained non-reducing SDS-PAGE gel of fractions corresponding to the UV absorbance peak. Magenta box indicates presumed CII dimer band.

Table 3.7: Protein concentrations (μg/ml) in Y54A CII toxin size exclusion chromatography fractions B1–B5.

Fraction number	**Protein concentration** (μg/ml)
B1	24
B2	113
B3	59
B4	8
B5	1

3.3.2.2 Functional characterisation

Following a successful purification of the Y54A CII mutant, we were interested in testing its activity and investigating whether there is any difference between the effect of WT vs mutant CII toxin on AMPAR. Electrophysiology experiments show that like wild-type CII, Y54A CII inhibits AMPAR desensitization in a dose-dependent manner (Figure 3.22 A). Comparing the dose-response curves of WT and mutant CII (Figure 3.22 B) reveals a slight right-shift, indicating that it is less potent than the wild-type toxin (EC_{50} of 1.7 $\pm$ 1 nM for WT CII *versus* EC_{50} of 5.1 $\pm$ 2 nM for Y54A CII mutant).

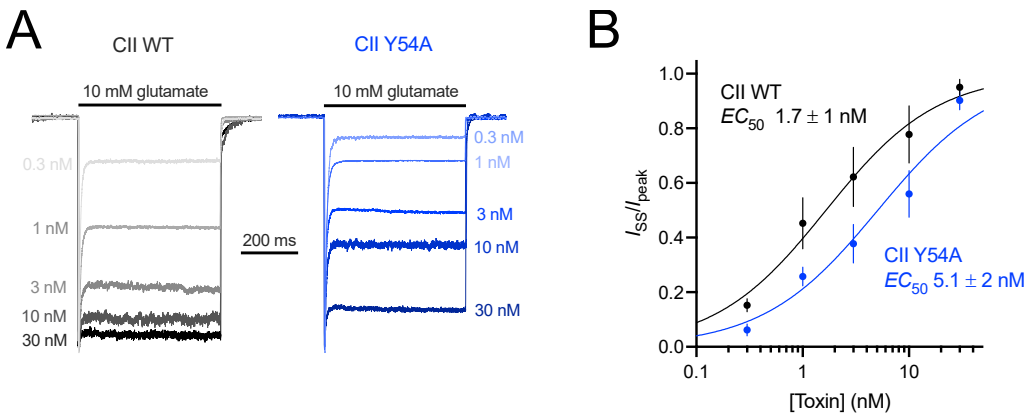

Figure 3.22: A. GluA2 WT AMPA receptor current traces showing increasingly blocked desensitization upon exposure to increasing concentrations of CII WT toxin (0.3 nM – 30 nM, black) or CII Y54A CII mutant (0.3 nM – 30 nM, blue). B. Dose-response curve of purified WT (black) and Y54A mutant (blue) CII toxin. Activity of CII is expressed as desensitization block of GluA2 WT AMPA receptors (steady-state current (I_{ss}) over peak current (I_{peak})); n = 3–5 patches per concentration; error bars denote SEM.

3.3.2.3 Labelling with fluorescent dye

Size exclusion chromatography

During the process of fluorescently labelling CII toxin with photoactivatable Janelia Fluor dyes (PA-JF 549 and PA-JF 646), removal of unbound dye remains a challenge due to the low protein concentration in the sample, as well as low sample volume. For this reason, we were interested in testing size-exclusion chromatography as a strategy for removal of unbound dye, as it is an already established step in the protocol for CII toxin purification. Due to the size difference between con-ikot-ikot the fluorescent dye, we expected the labelled protein to elute from the column early, followed by the dye at a higher elution volume. We tested this strategy by applying our Y54A CII sample labelled with PA-JF 646 as described in Section 2.2.3 to the size exclusion chromatography column and carrying out the protocol as previously with unlabelled samples.

While the protein concentration in the resulting fractions was too low for measurement, the presence of bands on the silver-stained non-reducing SDS-PAGE gel at the molecular weight corresponding to the CII dimer suggests that our strategy could be a viable method for removal of unbound fluorescent dye from the reaction mixture. We planned to continue investigating this avenue with samples containing more protein to confirm the feasibility and practicality of this approach.

However, several months after the purification process of the Y54A CII mutant was completed, we observed that the size exclusion chromatography column seemed to be irreversibly stained with an unidentified blue substance. PA-JF 646 is orange in DMSO- or water-based

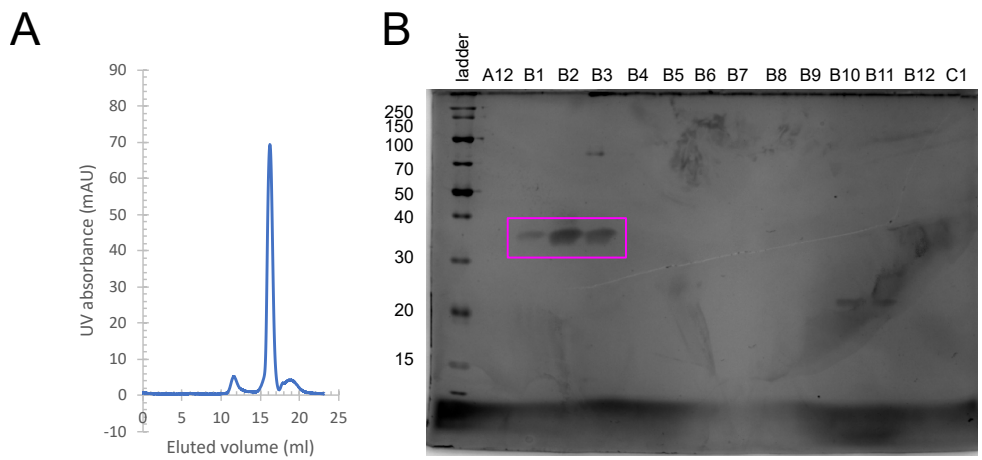

Figure 3.23: A. UV absorbance peak from PA-JF 549-labelled Y54A CII size exclusion chromatography. B. Silver-stained non-reducing SDS-PAGE gel of fractions corresponding to the UV absorbance peak. Magenta box indicates presumed CII dimer band.

solution when not photoactivated. Exposure to UV light (including long-term exposure to ambient levels of UV light) causes it to photoactivate and turn bright blue, therefore, we deduced that it bound to the column and failed to fully elute, only becoming visible after it has been exposed to enough UV light. This meant that despite promising early results, size exclusion chromatography is not suitable for removal of unbound dye from the fluorescent labelling reaction mixture.

Chapter 4

Discussion

4.1 AMPAR-CII MD simulation dataset

A large part of the project described in this thesis has been creating a dataset of MD simulations of AMPAR extracellular domains in complex with glutamate and con-ikot-ikot toxin. The dataset currently consists of fourteen sets of simulations of AMPAR GluA2 homotetramer extracellular domains in complex with WT or mutant CII toxin, unlabelled or labelled with a fluorescent dye at different positions; in addition to earlier simulations of more limited systems (AMPAR GluA2 LBDs in complex with CII).

It is important to recognise that there are limitations to the simulated models, as well as the trajectories obtained from MD simulations. Firstly, the all-atom model of the structure of the AMPAR-CII complex is by necessity imperfect. As there are no available crystal structures of the AMPAR-CII complex with glutamate bound inside the receptor's LBDs, the model is a hybrid of a crystal structure of partial-agonist-bound AMPAR in complex with CII [151], and soluble AMPAR LBD in complex with glutamate [60]. Only the extracellular domains of the receptor are included in the system and an artificial short linker is introduced in the LBD structure [60] (as the LBD is composed of two stretches of amino acids separated in sequence by the TMD M1–3, Figure 1.1 B). A number of residues or their side chains, missing from the original structures, were modelled in manually, including relatively long stretches of amino acids at the ATD–LBD linkers. Altogether, this means that any conclusions made based on the analysis of the MD simulation trajectories need to be made carefully to avoid ascribing importance to observations based on system preparation artifacts.

Further, as we were interested in investigating the interactions between an existing complex between the receptor and the toxin, the simulation length was chosen accordingly. However, other aspects of the interaction between the receptor and toxin which could be interesting to examine using simulations, such as the binding/unbinding of the toxin, would require simulations of longer timescales to be able to observe the events of interest. Especially in the case of

labelled toxin, examining the entry of the toxin into the space between the AMPAR ATDs and LBDs would be interesting. While our simulations suggest that even CII with all possible conjugation sites occupied by the fluorescent dye can be spatially accommodated within its binding site, the starting point of the simulation is a system where the labelled toxin already occupies the void between ATDs and LBDs. It is possible that fully labelled toxin would be prevented from entering this space due to the attached ten copies of fluorescent dye; however, determining this would require a different simulation set with a much longer simulation time to observe any binding events [269].

Another one of the general conclusions we have been able to draw from the analysis of the MD simulation trajectories has been that additional control could be obtained over the fluorescent labelling process by limiting the number of available dye conjugation sites via mutating lysine residues to alanine or arginine residues, similarly to the ”amine landscaping” strategy proposed for streptavidin to control its labelling due to issues related to ligand binding and fluorophore brightness [270]. The contributions of toxin lysine residues to the overall binding between CII and AMPAR are not among the highest of the toxin residues, therefore we believe that they could be mutated without majorly affecting the interactions between the toxin and the receptor. Importantly, the simulations of toxin mutants are based on an assumption that the mutated variants could be produced and would fold properly in the same way as the wild type toxin. If introducing the mutations resulted in changes in the structural properties of CII, they could change or even abolish binding between the toxin and AMPAR and any insights from our simulations would not apply to our understanding of the resulting receptor-toxin complex.

4.2 NAppEd – a new tool for residue interaction network analysis of MD simulation trajectories

NAppEd, the new tool for network analysis of residue interactions in MD simulation trajectories, offers an easy way to gain insights into the dynamic web of interactions between interacting protein partners. The tool is based on residue interaction detection with RING 3.0 [217] and can be used to visualise the network summarising multiple interaction types present throughout a set of simulations. This allows users to move away from reliance on static structures [205, 206] and towards dynamically behaving systems. While other tools are available for network analysis of MD trajectories with a focus on residue interactions [207, 208, 209, 210, 211, 212], their definitions of interactions are relatively simplistic (mostly distance-based, without distinguishing between interaction types) compared to those identified by RING 3.0 [217]. The tools which do consider interactions in a more complex way, taking into account the geometry and physicochemical properties of the amino-acids involved [212, 215], are either unavailable [212] or are

a way to efficiently generate networks but do not offer tools to analyse them [215].

With NApped, users can identify which residues and interactions make the largest contribution to the overall binding based on how much they engage in different interaction types detected by RING 3.0 [217], as shown in the analysis of the p53-MDM2 system. The main interactors highlighted by NAppEd were in good agreement with those suggested by alanine scanning and previously described in scientific literature. The insights into interaction partners and types of interaction a given residue engages in make it a useful complement to alanine scanning analysis, which summarises energetic contributions of residues to the overall binding energy, but does not include detailed descriptions of the interactions involved [252, 253].

The lack of interaction energy data in the results of analysis with NAppEd is a limitation which can lead to a potentially incorrect ranking of main residues contributing to interactions between protein partners. Another limitation of NAppEd is that multiple occurrences of the same interaction type between the same two residues in the same trajectory frame are only counted as one. This means that there is currently no intuitive way of estimating the energetic contribution of any one residue in a NAppEd interaction network based on the number of interactions of a certain type it forms and an average energy contribution from that interaction type. Interaction energy information is available in the RING output files used to construct interaction networks in NAppEd [217], so it is possible to incorporate this data into the analysis in the future and perform more direct comparisons of its results with alanine scanning results.

4.3 Network analysis of AMPAR-CII interactions with NAppEd

My analysis of interactions between AMPAR LBDs and CII using NAppEd and alanine scanning has recapitulated all three of the main toxin residues highlighted as interacting with AMPAR based on the crystal structure of the AMPAR-CII complex – Q37, E48, and A86 [151] – and highlighted additional residues – I49 and Y54 – with considerable contributions to the overall receptor-toxin interaction. The presence of A86, Q37, and E48 in this set of residues provides support for NAppEd as a useful tool for identifying important interactors between a pair of proteins in a complex, while finding additional residues that have an important role in the receptor-toxin interaction shows its utility in facilitating the generation of hypotheses about investigated residue interaction networks and their central players.

Another exciting new finding of my study of CII-AMPAR interactions using NAppEd is the first insight into interactions between CII and AMPAR ATD layer, suggesting that CII may be the first non-antibody AMPAR binder to make contacts with ATDs. The interactions are less pronounced than those the toxin makes with the receptor's LBD layer, as expected based on the crystal structure of the AMPAR-CII complex [151]. The toxin makes contacts with all four subunits (A–D) of the receptor at the ATD level, which opens up an opportunity to target

this domain layer. The amino-terminal domains are highly diverse between GluA1–4 subunit types (Figure 1.8), making them an attractive target for studies focused on developing probes that could bind AMPARs of specific subunit compositions. There is a clear need for tools with this property in the field, considering the wide variety of AMPAR subunit compositions [20] and the different spatio-temporal expression patterns [12], functional properties [16, 17], and interacting partners [271] of different AMPAR subunits. Being able to tag AMPARs based on what subunits they are composed of and identify their localisation and/or track their movements would bring novel insights into how the composition of AMPARs changes during development and synaptic plasticity and what rules govern the trafficking of different receptor subtypes. Moreover, selectively targetting specific sub-populations of AMPAR would be a significant step in drug development, especially given the limited therapeutic options currently approved for modulating AMPARs [118], as it would allow the modulation of only populations of AMPARs affected by disease-causing mutation [165], while the remaining AMPARs could retain their normal function.

4.4 Successful introduction of csCyDisCo into the expression protocol of CII

We were successful in the introduction of csCyDisCo [224] into the CII expression protocol. The introduction of an additional plasmid into the *E. coli* bacteria we used for protein expression was tolerated well and we were able to obtain functional purified WT CII toxin as in the previous purifications. Using the csCyDisCo system allowed us to use BL21 (DE3), a faster-growing bacterial *E. coli* strain than ORIGAMI, which was part of the original purification protocol [151]. Thanks to this, the time required for a full round of protein expression (from bacterial transformation to freezing collected bacterial pellets in liquid nitrogen) could be reduced from about a week to four days.

In line with previous findings regarding the expression of conotoxins using csCyDisCo [224, 225], we did not observe an increase in protein yield when expressing wild-type with csCyDisCo as compared to previous purifications; in fact, the yield we achieved was comparable to previous purifications done by our lab and others ($\sim$400 µg of purified protein from 48 l of bacterial culture in my purification versus 40–100 µg per 12 l previously [151]). However, it is important to note that as the purifications with and without csCyDisCo were not carried out in parallel but rather by different people in different places and at different times, we cannot draw strong conclusions about the differences in observed yields between the two conditions.

We observed an apparent difference in the appearance of the CII bands in SDS-PAGE gels of WT toxin size exclusion chromatography fractions, as compared with previous purifications by

our lab and others. The band typically appears considerably smeared towards higher apparent molecular weights in the gel. We observed less smearing and almost an appearance of several fainter bands at molecular weights close to the main band (Figure 3.16). This may be the effect of the csCyDisCo system components facilitating the proper folding and formation of correct disulfide bonds in the toxin, resulting in a more homogeneous population of toxin molecules, similar to the effect observed in another conotoxin, Conk-S3 when expressed with csCyDisCo [225]. Conk-S3 only contains two disulfide bonds, while CII contains 13, resulting in a much higher number of possible oxidation states, which could be responsible for the typical smeared appearance of the SDS-PAGE gel bands. Further testing is required to determine whether this is the case or if there is another explanation for the smeared appearance of the CII band and whether the change in its appearance in this purification can be reproduced in the future.

Another feature of the SDS-PAGE gels included in this thesis which would be interesting to explore further is the identity of the low molecular weight band in the gels of fractions from size exclusion chromatography of WT CII (Figure 3.16 B - fractions B4–B6). The apparent molecular weight the band appears at seems to correspond well to the monomeric CII (Figure 3.15 B), but the band could also represent a toxin degradation product and the CII monomer could be present in the same fractions as the dimer (lower molecular weight bands in lanes B1–B6). If the content of fractions B4–B6 was confirmed by mass spectrometry to be monomeric toxin, it would be interesting to test its binding and functional effect on AMPA receptors. Perhaps if inter-subunit disulfide bonds in the toxin could be removed by mutation of the appropriate cysteine residues, monomeric CII-based probes against AMPAR could be another avenue to pursue in the future.

The successful introduction of csCyDisCo into the expression protocol for CII toxin was confirmed by the toxin displaying normal activity [63] in terms of blocking AMPAR desensitization in the electrophysiology experiment.

A significant remaining challenge in the process of CII purification is the removal of fusion tag from the toxin. The toxin is fused with a Trx tag for solubility, followed by the StrepTag for affinity purification, and a HRV 3C protease cleavage site to cut off the tags from the toxin following the affinity purification step [151]. The Trx tag is close in size to the size of CII toxin monomer, while the StrepTag and protease cleavage site are each 8 amino acid residues long. Once cleaved, the tag needs to be removed in the process of toxin purification – this is currently achieved by methanol precipitation, which is also the step in the purification which results in the largest protein loss. The similar size of both cleavage products (target protein – CII toxin – and cleaved off tag) makes it impossible to tell from an SDS-PAGE gel of the resulting sample whether the tag has been removed or whether the sample is a mixture of both products.

One strategy that can be employed to avoid excessive protein loss and remove the tag while leaving the toxin in the sample could be the use of a second StrepTactin chromatography round

as a clean-up measure. The now-cleaved purification tag would attach to the column, while the toxin would be present in the flow-through, similarly as in the protocol used to purify conotoxin H-Vc7.2 [224]. Alternatively, if a different protease cleavage site was introduced between the Trx tag and StrepTag, initial purification of filtered cell lysate with a StrepTactin column could be followed by cutting off the Trx tag and a second StrepTactin column, where the toxin would now be bound to the resin and eluted in fractions. The subsequent cleavage of the StrepTag would produce two products of different sizes, which could be more easily separated in the remaining purification steps. The band appearing at the molecular weight of monomeric CII in the SDS-PAGE gels of StrepTactin fractions would then be easier to interpret in terms of its intensity and the identity of its contents.

4.5 Functional properties of the Y54A CII mutant

In order to validate the results of computational analyses, we purified a CII toxin mutant for the first time. We selected Y54 as the target for the mutation to alanine as it was one of the residues suggested by my NAppEd analysis as important for the interactions between CII and AMPAR LBDs, while not having been highlighted in literature based on the crystal structure of the AMPAR-CII complex [151]. We expected the Y54A CII variant to bind less strongly to AMPAR LBDs as a result of disrupting its side chain interactions, as in computational alanine scanning.

The electrophysiology results showed a right shift in the dose response curve with respect to the dose response curve of the WT toxin, indicating a lower potency of the Y54A variant, consistent with our expectations. The change in potency can be a result of the Y54A variant indeed binding to AMPAR with lower affinity than WT CII toxin, and/or inhibiting AMPAR desensitization to a lesser degree [272]. To distinguish between these two possibilities (or a combination of both), it would be useful to establish and optimise a protocol for assessing toxin binding to AMPAR without using its functional effect as a proxy. This would be especially important for possible future development of functionally silent toxin variants that could bind to AMPAR, but not block the receptor's desensitization. One method to test the K_d of such variants could be biolayer interferometry [273, 274].

4.6 Labelling of WT CII and Y54A CII mutant

During the course of my thesis project, I used the photoactivatable fluorescent dye PA-JF 646 to label purified WT CII and partially purified Y54A CII variant. The labelling of WT toxin was confirmed with mass spectrometry, which suggested that about 12% of the toxin present in the sample has been labelled, and that the labelling has occurred at a 1:1 dye:toxin ratio. This

means that WT CII toxin could be used as a fluorescent AMPAR-specific marker without the need for ”amine landscaping” [270] to optimise the degree of labelling, given that according to my simulation results, the dye can be accommodated at any of the conjugation sites of the toxin. The 1:1 ratio of dye to toxin would mean a 1:1 ratio of dye to CII-labelled AMPAR in experimental applications of the toxin-based AMPAR probe, which could be important for its use in quantitative super-resolution studies [275, 276, 277]. We were not able to test the labelled Y54A CII variant with mass spectrometry due to an insufficient amount of labelled protein recovered.

When labelling the Y54A CII variant, we tested size exclusion chromatography as a method of unbound dye removal from the labelling reaction mixture, as it was already a part of the toxin purification protocol and in principle should be an effective way of separating the toxin from the smaller-sized fluorescent dye also present in the sample. Despite early promising results, it appears that the dye did not fully elute from the chromatography column’s resin, which makes this technique not appropriate for our needs.

Chapter 5

Conclusion

This thesis describes the work I have carried out to use computational methods to investigate the interactions between con-ikot-ikot and AMPAR. I have produced an MD simulation dataset containing simulations of the extracellular domains of homotetrameric GluA2 AMPA receptor in complex with glutamate and WT CII, as well as several CII mutant variants, with or without fluorescent dye attached at various positions.

The development of the new tool for residue interaction network analysis of MD simulation trajectories – NAppEd – has allowed me to gain new insights into the interactions of the toxin with the LBD layer of the AMPA receptor and revealed novel interactions with the ATD layer. While I developed NAppEd for the analysis of this specific system, its performance in identifying interacting residues and their main interactions in the complex formed between p53 and MDM2 shows its utility in the analysis of MD simulation trajectories of any protein complex where the residue interactions are of interest.

I used the insights from computational analyses – both with NAppEd and alanine scanning – to design a CII toxin mutant, Y54A, which according to my data should bind less strongly to the AMPA receptor due to the removal of Y54, which has been highlighted as one of the CII residues with high contributions to its interaction with AMPAR. Experimental data have shown that the Y54A CII variant exhibits lower potency in blocking AMPAR desensitization than the WT toxin, validating the results of the computational analyses. This shows that MD simulations can be a useful source of information that can be used for the design of variants of proteins such as CII, which require considerable time and resources to purify and achieve very low yields.

5.1 Further work

The work described in this thesis has been the initial effort in the closer investigation of the interactions between con-ikot-ikot and AMPAR with the aim of utilising the insights from the analyses in the development of AMPAR-specific tools. Some of the insights from the analysis

could be further built upon both in the immediate future of the project and in the longer term; and aspects of the computational and experimental procedures could be improved for better performance.

5.1.1 Experimental procedures

On the technical side of the experimental part of the project, the protocol for the purification of CII and its mutants could be improved to produce more toxin more efficiently. Firstly, it would be useful to determine the thermal stability of con-ikot-ikot. If the toxin proved to be highly heat-resistant (as, for example, conotoxin H-Vc7.2 [224]), an addition of a boiling step in the purification process could be considered to efficiently remove non-temperature-resistant components from the sample. As discussed in Section 4.4, improvements could be made to how the cleaved fusion tag is removed from the toxin sample.

Further, alternative options for fluorescent labelling of the toxin could be explored in the absence of a suitable method for removal of unbound fluorescent dye following the labelling reaction (see Section 4.6). One such alternative strategy to consider could be site-specific labelling at the N-terminus using sortase A, a bacterial enzyme involved in cell wall biosynthesis, during which it anchors proteins to the bacterial cell wall [278]. The requirement for this reaction, boasting yields in excess of 90% [278], is a stretch of 1–5 glycine (G) or 2–5 alanine (A) residues at the target protein's N-terminus, sufficiently exposed to allow the enzyme's access to it for labelling. This is already present in the toxin in the form of the four amino acid stretch left at the N-terminus after the HRV 3C protease cleavage. One of the disadvantages of this labelling strategy is that the fact that a method for removing the enzyme from the reaction mixture with minimal loss of toxin would have to be introduced into the protocol – a solution could be the use of immobilised sortase A [279]. Moreover, as the fluorescent component of the reaction would have to be a peptide of a specific sequence recognised by sortase, the linkage error of the resulting fluorescently labelled CII-based probe would be increased by the length of the peptide designed for this purpose (at least six amino acid residues long [278]).

5.1.2 Computational work

We envision NAppEd as a tool not just for the one-time analysis of CII contacts with AMPAR, but rather as a general tool for hypothesis generation about residue interaction networks and main interacting residues in MD simulation trajectories of protein complexes. Hence, it would be useful to continue working on the NAppEd code in order to expand the information available from the network analysis, for example by incorporating interaction energy data into the building of the network, or by updating it to use RING 4.0 [216] than RING 3.0 [217] for the detection of interactions in order to include non-protein interaction partners, which cannot be

processed with RING 3.0. We plan to make the code publicly available so any researcher interested in using our analysis can easily access it, but it would also be beneficial to create a web application which users who are not as familiar with using code could still use to analyse and visualise their residue interaction networks.

Additionally, it would be interesting to analyse simulations of the GluA1212 heterotetramer extracellular domains in complex with WT con-ikot-ikot and analyse them using NAppEd in order to compare the toxin-receptor interactions between this system and the GluA2 homotetramer-based system. Focusing in particular on any potential differences in interactions between the toxin and GluA1 and GluA2 subunit in position A/C of the receptor could help direct the design of toxin-based probes or toxin-inspired peptide binders towards specificity for different AMPAR subunit compositions.

5.1.3 Con-ikot-ikot toxin variants and related probes

In terms of building on the results from my work, it would be interesting to express, purify, and functionally characterise more CII toxin mutants. Mutating more of the residues highlighted by NAppEd and alanine scanning as important for the toxin's interactions with AMPARs would further validate the computational results. The mutants' potencies and/or binding affinities for the interaction with AMPAR could then be compared not only to those the wild-type toxin, but also between variants, yielding additional information about the relative contributions of mutated residues to the binding to AMPAR. Further, using monomeric toxin as a label for AMPAR could be an interesting avenue to explore, and removing inter-subunit disulfide bonds by mutating the appropriate cysteines, and subsequently characterising the properties of the resulting mutant, would be a good starting point for this investigation.

In the longer term, it will be an interesting development to design functionally silent CII-based probes, which would bind to AMPARs, but would not block the receptors' desensitization. This will have to be connected with an adoption and optimization of an appropriate assay to assess the binding of the toxin to the receptors without relying on its functional effects as a proxy, e.g. using biolayer interferometry [273, 274].

Drawing from the CII interactions with the ATD layer of the AMPA receptor, illuminated by my analysis with NAppEd, it would be worth pursuing the idea of harnessing these new-found contacts with the aim of producing AMPAR-specific probes capable of targetting specific subunit compositions. There is a clear need in the field for binders targeting specific AMPAR populations, both for research purposes and for potential therapeutic applications, therefore it is exciting to imagine the insights from this work contributing to what could be the first AMPAR subunit composition-specific probe.

Another important development of the con-ikot-ikot work will be to use the insights from the analysis of my MD simulations to inform the design of small *de novo* peptides which

could target the AMPAR ATD or LBD layer for scientific research and potential drug development [167, 168]. These small peptides would have an obvious advantage over the CII toxin in that they could be easily chemically synthesised, unlike CII, which is too large. Similarly as the toxin, they could then be fluorescently labelled and used for super-resolution studies of AMPAR.

Finally, a natural direction for the development of this project is to test the labelled WT CII and any other CII-based and CII-inspired probes in imaging experiments, with synaptosomes, cultured neurons, and brain slices as the imaged samples. Optimal labelling conditions, such as toxin solution concentration, will have to be determined based on the results of the experiments. It will be interesting to compare the labelling with toxin to conventional antibody-based labelling and in the longer term, gain insights about AMPAR nanoscale organisation at the synapse and their trafficking in and out of the synaptic sites.

Appendix A

Summary of MD simulations of the AMPAR-CII system

Table A.1: Details of the MD simulations of the AMPAR-CII simulated systems. Rows coloured orange represent simulations prepared by summer project students: Jana Hennelova and Manaal Shah. TO - truncated octahedron

AMPAR component (all tetramer)	**CII component**	**Fluorescent dye position**	**Ions**	**Total atoms**	Size of solvation box (Å)
ATD_LBD	wild-type	-	12 K^+	291310	(TO) 185.369 x 185.369 x 185.369
ATD_LBD	wild-type	G-3, K10, K30, K65, K77	22 K^+	290387	(TO) 185.333 x 185.333 x 185.333
ATD_LBD	K10R K30R K77R	-	12 K^+	291265	(TO) 185.404 x 185.404 x 185.404
ATD_LBD	K10R K30R K77R	K65	14 K^+	291057	(TO) 185.402 x 185.402 x 185.402
ATD_LBD	K10R K30R K77R	G-3	14 K^+	291240	(TO) 185.424 x 185.424 x 185.424

ATD_LBD	K10R K30R K77R	G-3, K65	16 K^+	290975	(TO) 185.426 x 185.426 x 185.426
ATD_LBD	K10A K30A K77A	-	18 K^+	291172	(TO) 185.369 x 185.369 x 185.369
ATD_LBD	K10A K30A K77A	G-3	20 K^+	291490	(TO) 185.370 x 185.370 x 185.370
ATD_LBD	K10A K30A K77A	K65	20 K^+	290850	(TO) 185.357 x 185.357 x 185.357
ATD_LBD	K10A K30A K77A	G-3, K65	22 K^+	290666	(TO) 185.358 x 185.358 x 185.358
ATD_LBD	K10R K30R K65R K77R	-	12 K^+	291260	(TO) 185.404 x 185.404 x 185.404
ATD_LBD	K10R K30R K65R K77R	G-3	14 K^+	291229	(TO) 185.424 x 185.424 x 185.424
ATD_LBD	K10A K30A K65A K77A	-	20 K^+	291174	(TO) 185.369 x 185.369 x 185.369
ATD_LBD	K10A K30A K65A K77A	G-3	22 K^+	291014	(TO) 185.372 x 185.372 x 185.372

Appendix B

Sources of residue conformations in the GluA2 ATD-LBD-Glu-CII simulated system

The tables below show the sources from which residues in the GluA2 AMPAR ATD-LBD model were taken. Residues in black come from the 4U5D model [151], residues in red were not present in the original sequence and were modelled in manually, residues in green (forming the ATD-LBD linkers) were modelled in manually as they were not resolved in the structure, and residues in apricot come from the 1FTJ model [60].

Residues whose side chains were not resolved in the 4U5D structure are highlighted according to the structure used to model in the missing side chains: in pink for 4U5C [151], green for 3KG2 [9], and cyan for 5VHY [227]. Residues highlighted in yellow are those whose missing side chain conformations were modelled according to the lowest energy score in the PyMOL Mutagenesis wizard. The numbering starts at 6 in order to follow the original numbering of 4U5D (until residues L383 and P384).

Subunit A

```
     NSIQIGGLFPRGADQEYSAFRVGMVQFSTSEFRLTPHIDNLEVAN   50
SFAVTNAFCSQFSRGVYAIFGFYDKKSVNTITSFCGTLHVSFITPSFPTD  100
GTHPFVIQMRPDLKGALLSLIEYYQWDKFAYLYDSDRGLSTLQAVLDSAA  150
EKKWQVTAINVGNINNDKKDETYRSLFQDLELKGERRVILDCERDKVNDI  200
VDQVITIGKHVKGYHYIIANLGFTDGDLLKIQFGGAEVSGFQIVDYDDSL  250
VSKFIERWSTLEEKEYPGAHTATIKYTSALTYDAVQVMTEAFRNLRKQRI  300
EISRRGNAGDCLANPAVPWGQGVEIERALKQVQVEGLSGNIKFDQNGKRI  350
NYTINIMELKTNGPRKIGYWSEVDKMVVTLTELPSGDDTSGLEQKTVVVT  400
TILESPYVMMKKNHEMLEGNERYEGYCVDLAAEIAKHCGFKYKLTIVGDG  450
KYGARDADTKIWNGMVGELVYGKADIAIAPLTITLVREEVIDFSKPFMSL  500
GISIMIKKGTPIESAEDLSKQTEIAYGTLDSGSTKEFFRRSKIAVFDKMW  550
TYMRSAEPSVFVRTTAEGVARVRKSKGKYAYLLESTMNEYIEQRKPCDTM  600
KVGGNLDSKGYGIATPKGSSLGNAVNLAVLKLNEQGLLDKLKNKWWYDKG  650
EC
```

Subunit B

```
     NSIQIGGLFPRGADQEYSAFRVGMVQFSTSEFRLTPHIDNLEVAN   50
SFAVTNAFCSQFSRGVYAIFGFYDKKSVNTITSFCGTLHVSFITPSFPTD  100
GTHPFVIQMRPDLKGALLSLIEYYQWDKFAYLYDSDRGLSTLQAVLDSAA  150
EKKWQVTAINVGNINNDKKDETYRSLFQDLELKGERRVILDCERDKVNDI  200
VDQVITIGKHVKGYHYIIANLGFTDGDLLKIQFGGAEVSGFQIVDYDDSL  250
VSKFIERWSTLEEKEYPGAHTATIKYTSALTYDAVQVMTEAFRNLRKQRI  300
EISRRGNAGDCLANPAVPWGQGVEIERALKQVQVEGLSGNIKFDQNGKRI  350
NYTINIMELKTNGPRKIGYWSEVDKMVVTLTELPSGDDTSGLEQKTVVVT  400
TILESPYVMMKKNHEMLEGNERYEGYCVDLAAEIAKHCGFKYKLTIVGDG  450
KYGARDADTKIWNGMVGELVYGKADIAIAPLTITLVREEVIDFSKPFMSL  500
GISIMIKKGTPIESAEDLSKQTEIAYGTLDSGSTKEFFRRSKIAVFDKMW  550
TYMRSAEPSVFVRTTAEGVARVRKSKGKYAYLLESTMNEYIEQRKPCDTM  600
KVGGNLDSKGYGIATPKGSSLGNAVNLAVLKLNEQGLLDKLKNKWWYDKG  650
EC
```

Subunit C

```
     NSIQIGGLFPRGADQEYSAFRVGMVQFSTSEFRLTPHIDNLEVAN   50
SFAVTNAFCSQFSRGVYAIFGFYDKKSVNTITSFCGTLHVSFITPSFPTD  100
GTHPFVIQMRPDLKGALLSLIEYYQWDKFAYLYDSDRGLSTLQAVLDSAA  150
EKKWQVTAINVGNINNDKKDETYRSLFQDLELKGERRVILDCERDKVNDI  200
VDQVITIGKHVKGYHYIIANLGFTDGDLLKIQFGGAEVSGFQIVDYDDSL  250
VSKFIERWSTLEEKEYPGAHTATIKYTSALTYDAVQVMTEAFRNLRKQRI  300
EISRRGNAGDCLANPAVPWGQGVEIERALKQVQVEGLSGNIKFDQNGKRI  350
NYTINIMELKTNGPRKIGYWSEVDKMVVTLTELPSGDDTSGLEQKTVVVT  400
TILESPYVMMKKNHEMLEGNERYEGYCVDLAAEIAKHCGFKYKLTIVGDG  450
KYGARDADTKIWNGMVGELVYGKADIAIAPLTITLVREEVIDFSKPFMSL  500
GISIMIKKGTPIESAEDLSKQTEIAYGTLDSGSTKEFFRRSKIAVFDKMW  550
TYMRSAEPSVFVRTTAEGVARVRKSKGKYAYLLESTMNEYIEQRKPCDTM  600
KVGGNLDSKGYGIATPKGSSLGNAVNLAVLKLNEQGLLDKLKNKWWYDKG  650
EC
```

Subunit D

```
     NSIQIGGLFPRGADQEYSAFRVGMVQFSTSEFRLTPHIDNLEVAN   50
SFAVTNAFCSQFSRGVYAIFGFYDKKSVNTITSFCGTLHVSFITPSFPTD  100
GTHPFVIQMRPDLKGALLSLIEYYQWDKFAYLYDSDRGLSTLQAVLDSAA  150
EKKWQVTAINVGNINNDKKDETYRSLFQDLELKGERRVILDCERDKVNDI  200
VDQVITIGKHVKGYHYIIANLGFTDGDLLKIQFGGAEVSGFQIVDYDDSL  250
VSKFIERWSTLEEKEYPGAHTATIKYTSALTYDAVQVMTEAFRNLRKQRI  300
EISRRGNAGDCLANPAVPWGQGVEIERALKQVQVEGLSGNIKFDQNGKRI  350
NYTINIMELKTNGPRKIGYWSEVDKMVVTLTELPSGDDTSGLEQKTVVVT  400
TILESPYVMMKKNHEMLEGNERYEGYCVDLAAEIAKHCGFKYKLTIVGDG  450
KYGARDADTKIWNGMVGELVYGKADIAIAPLTITLVREEVIDFSKPFMSL  500
GISIMIKKGTPIESAEDLSKQTEIAYGTLDSGSTKEFFRRSKIAVFDKMW  550
TYMRSAEPSVFVRTTAEGVARVRKSKGKYAYLLESTMNEYIEQRKPCDTM  600
KVGGNLDSKGYGIATPKGSSLGNAVNLAVLKLNEQGLLDKLKNKWWYDKG  650
EC
```

Appendix C

PA-JF549 partial charges

Table C.1 shows the atoms modified in the process of adding fluorescent dye PA-JF549 to the simulated system, along with the corresponding assigned partial charges. The names of atoms in the dye molecule and amino acids can be found in Figure C.1.

Table C.1: Modified atoms and corresponding assigned partial charges. Asterisks mark atoms which were assigned a charge slightly varying from that in the .mol2 file from which the rest of the charges were taken.

Labelled glycine		**Labelled lysine**	
Atom name	Assigned charge	Atom name	Assigned charge
glycine N	-0.550900	lysine NZ	-0.565900
glycine CA	0.039000	lysine CD	-0.107400
glycine HA2	0.104200	lysine CG	-0.073400
glycine HA3	0.104200	dye O1	-0.233200
dye O2	-0.583100	dye O2	-0.596100
dye C11	-0.047300	dye O3	-0.572300
dye C12	-0.064000	dye C09	-0.198500
dye C14	0.692900*	dye C14	0.65580*
dye C26	-0.142600	dye C17	-0.198500
dye C27	-0.073000	dye C28	-0.125000
dye C28	-0.119000		

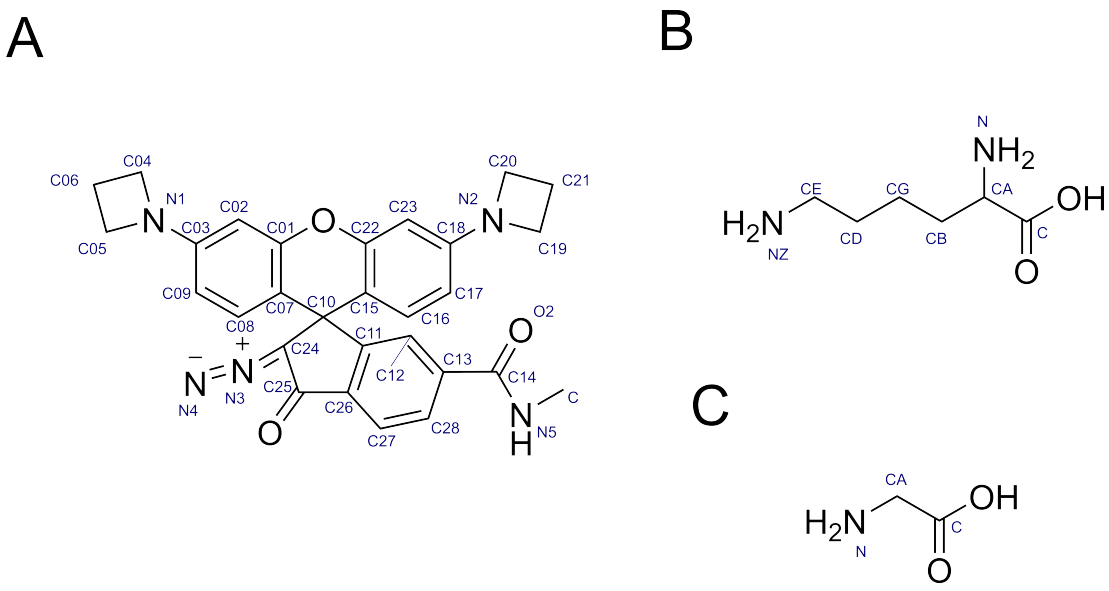

Figure C.1: Names assigned to atoms in PA-JF549 fluorescent dye (A) lysine residue (B) and glycine residue (C).

Appendix D

Sequence alignment of GluA1 and GluA2

I carried out a pairwise sequence alignment of the rat *Rattus norvegicus* GluA1 and GluA2 AMPAR subunits using the EMBOSS Needle pairwise sequence alignment tool [230] (Figure D.1). The sequences were found to share 67% identity and 80.6% similarity to each other. I used this sequence alignment to introduce relevant amino acid substitutions to the A and C subunits of my previously built GluA2 homotetrameric ATD-LBD model in order to turn it into a GluA1A2A1A2 heterotetramer model.

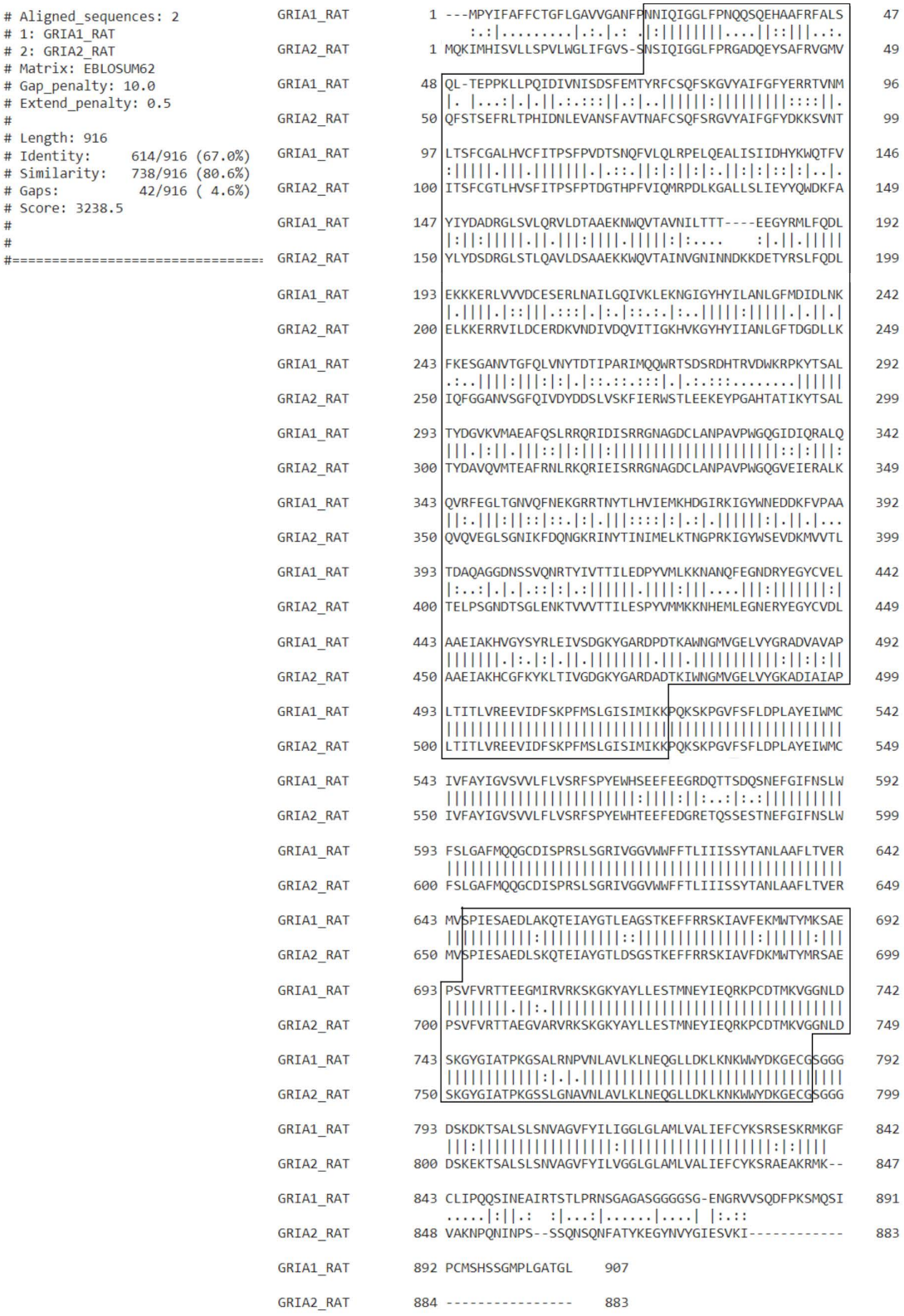

Figure D.1: Pairwise sequence alignment of rat (*Rattus norvegicus*) GluA1 vs GluA2 AMPAR subunits. Black boxes surround sequence regions that are included in the GluA1A2A1A2 hetero-tetramer ATD-LBD model I built.

Appendix E

AMPAR GluA2 ATD-LBD-Glu-CII system – CII lysine mutants

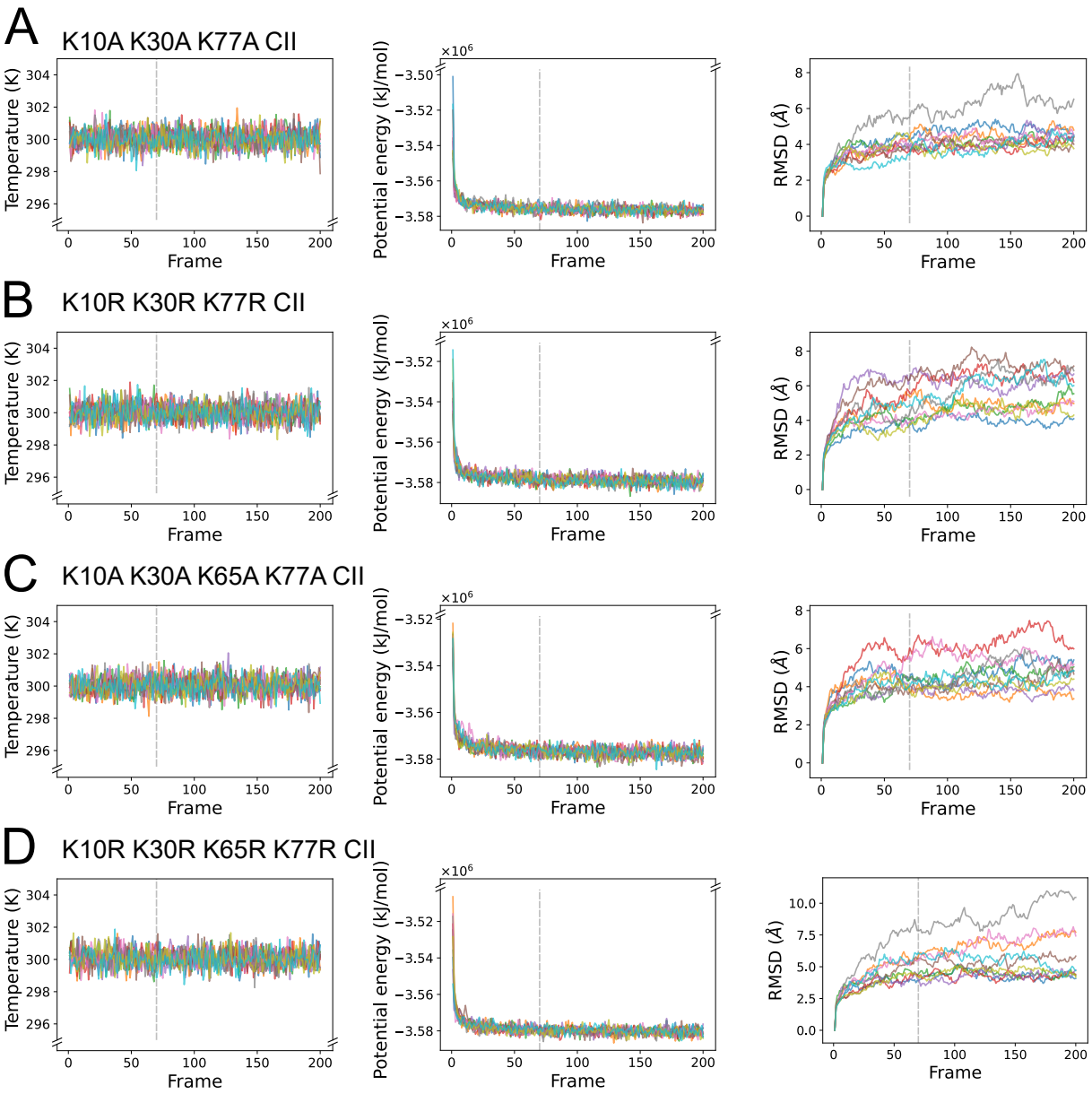

Figure E.1: Quality control measures (potential energy, temperature, and RMSD) over the course of simulation – GluA2 homotetramer ATD-LBD-Glu-CII system with CII variants: A. triple lysine-to-alanine mutant K10A K30A K77A CII. B. triple lysine-to-arginine mutant K10R K30R K77R CII. C. quadruple lysine-to-alanine mutant K10A K30A K65A K77A CII. D. quadruple lysine-to-arginine mutant K10R K30R K65R K77R CII. The grey vertical lines show Frame 70, which was taken as the beginning of the equilibrated portion of the simulations.

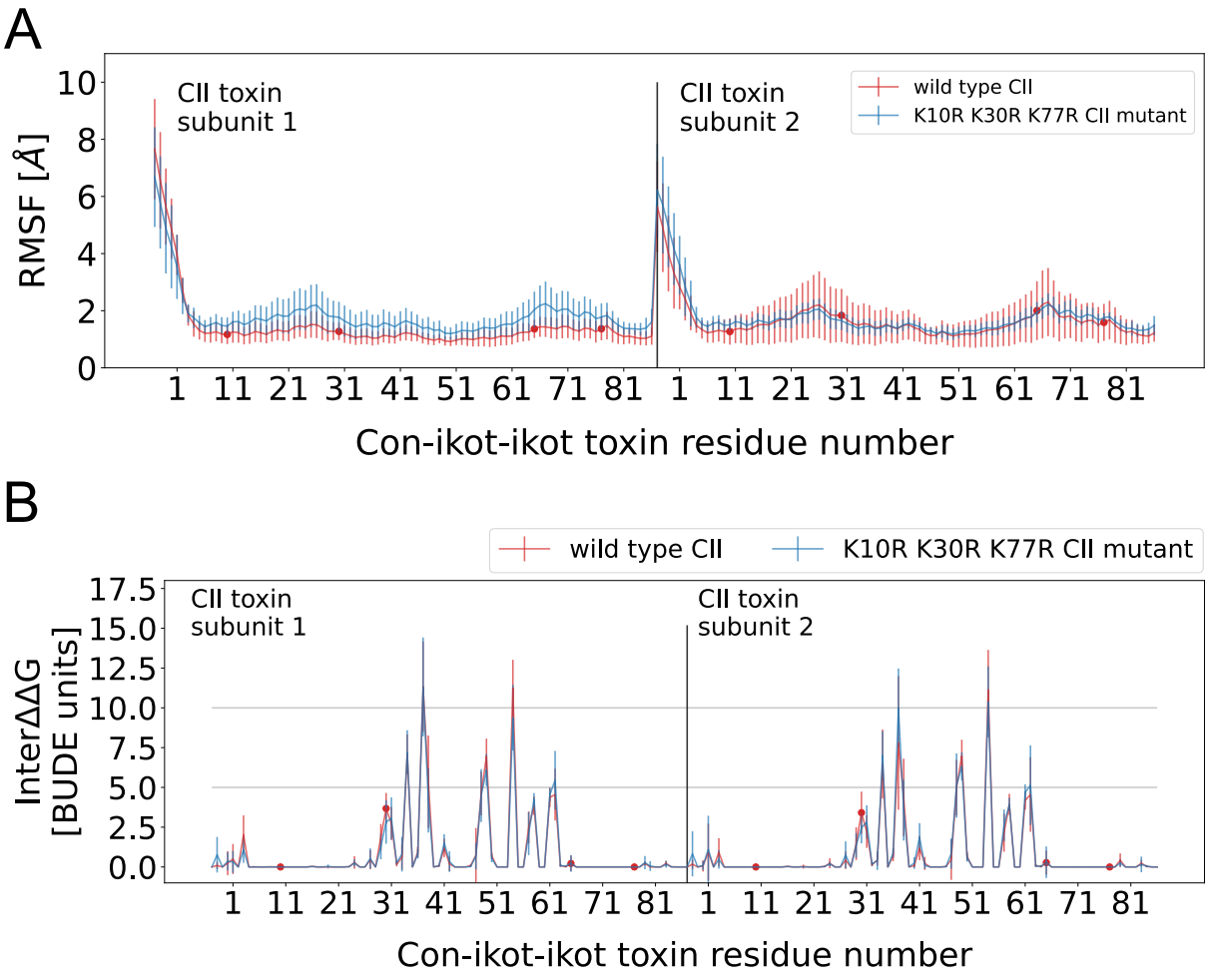

Figure E.2: Results of RMSF per residue (A) and alanine scanning (B) analyses for WT CII toxin (red) and the triple lysine-to-arginine mutant K10R K30R K77R (blue). Results shown as mean ± standard deviation.

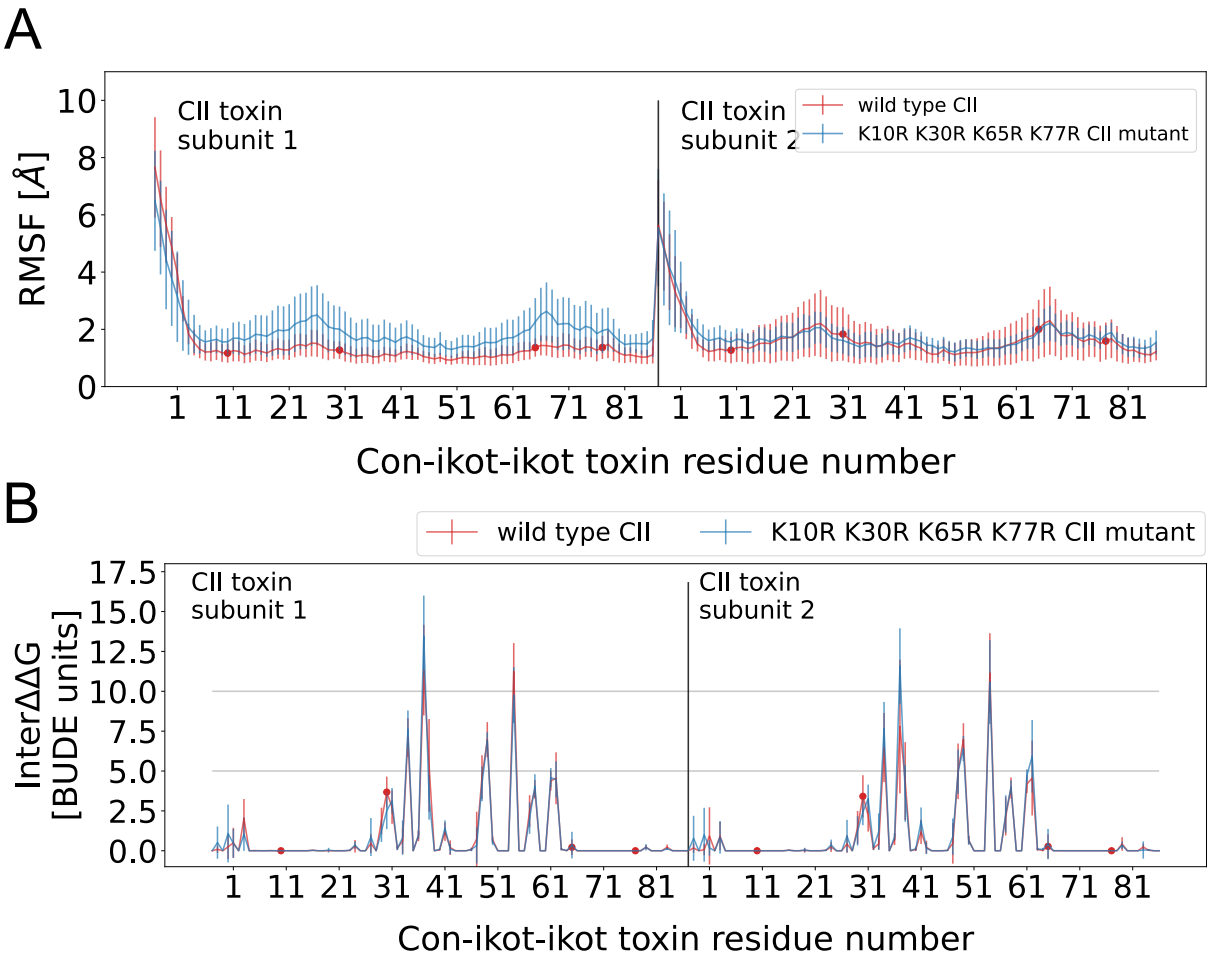

Figure E.3: Results of RMSF per residue (A) and alanine scanning (B) analyses for WT CII toxin (red) and the quadruple lysine-to-arginine mutant K10R K30R K65R K77R (blue). Results shown as mean ± standard deviation.

Appendix F

AMPAR GluA2 ATD-LBD-Glu-Cll system – labelled WT and mutant Cll

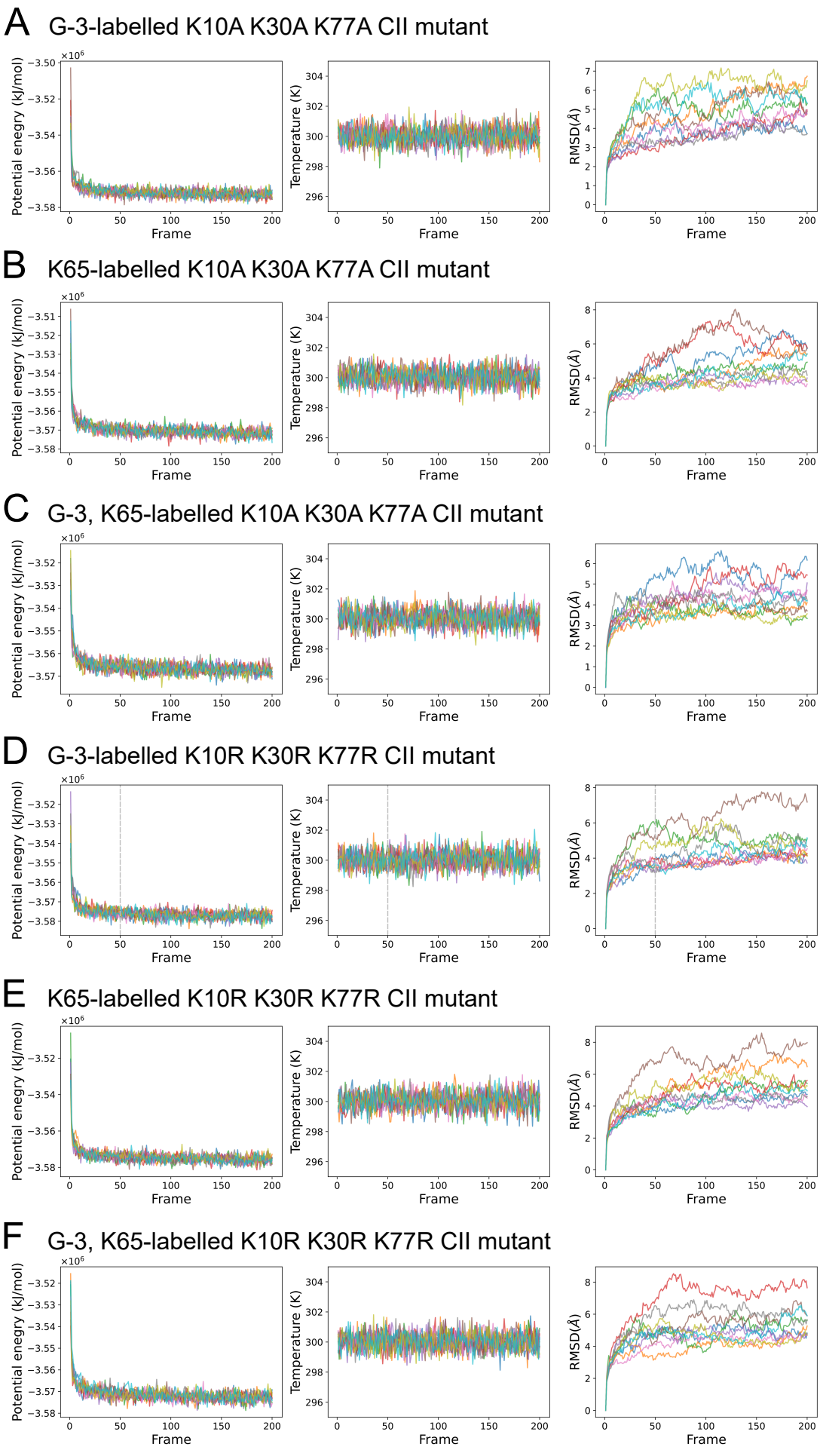

Figure F.1: Quality control measures (potential energy, temperature, and RMSD) over the course of simulation – GluA2 homotetramer ATD-LBD-Glu-CII system with labelled triple lysine CII mutants.

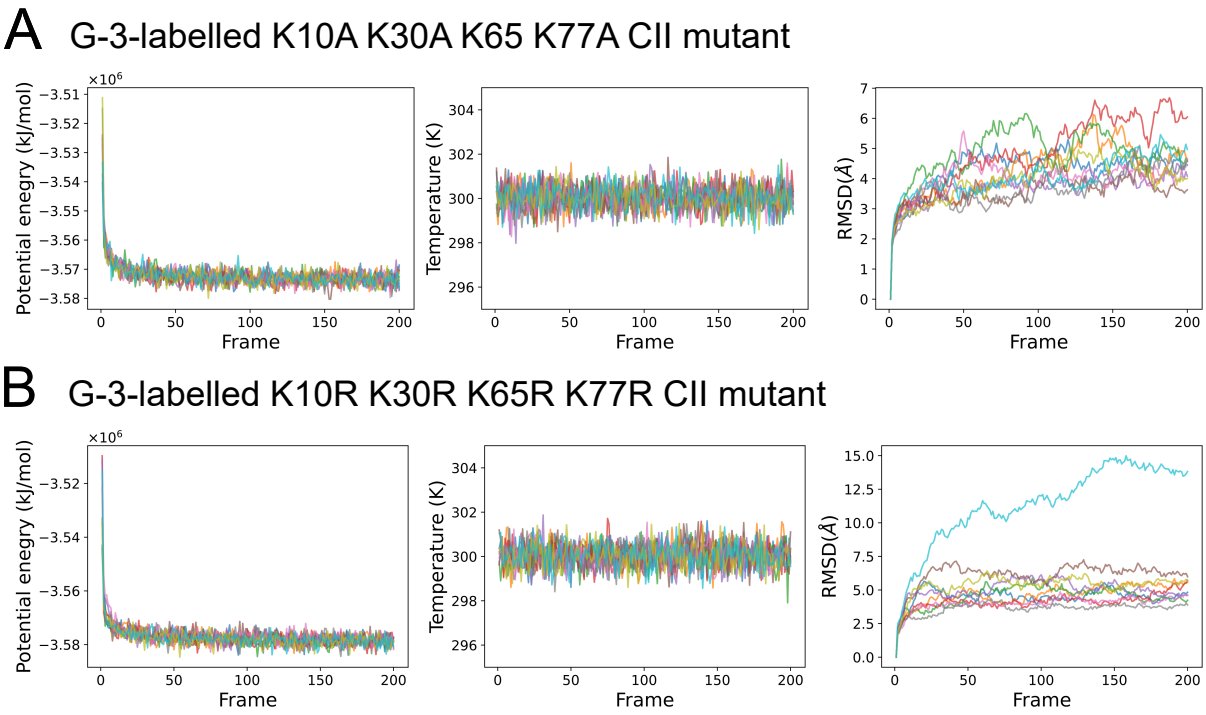

Figure F.2: Quality control measures (potential energy, temperature, and RMSD) over the course of simulation – GluA2 homotetramer ATD-LBD-Glu-CII system with labelled quadruple lysine CII mutants.

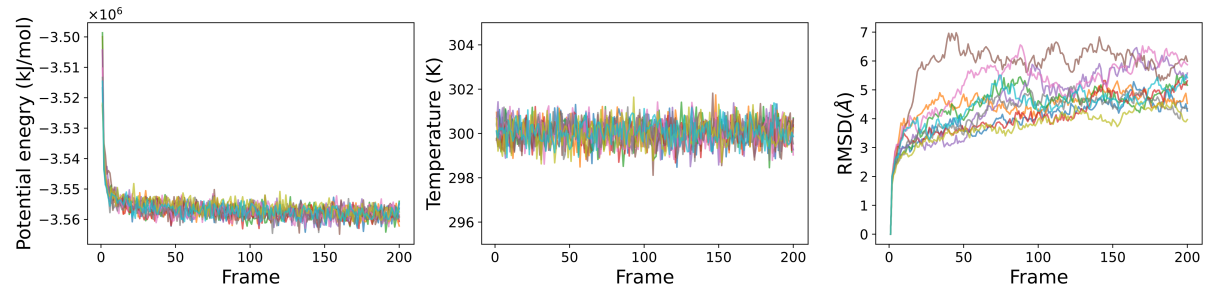

Figure F.3: Quality control measures (potential energy, temperature, and RMSD) over the course of simulation – GluA2 homotetramer ATD-LBD-Glu-CII system with fully labelled WT CII - labelled at G-3, K10, K30, K65, and K77.

Appendix G

CII toxin interactions with AMPAR LBDs

Table G.1: Results of BUDE alanine scanning - top 20 CII residues interacting with AMPAR LBDs.

Rank	Residue	Subunit	BUDE AlaScan score	Rank	Residue	Subunit	BUDE AlaScan score
1	Q37	subunit 1	11.3	11	E48	subunit 1	4.6
2	Y54	subunit 1	11.2	12	R62	subunit 2	4.6
3	Y54	subunit 2	11.1	13	R62	subunit 1	4.5
4	Q37	subunit 2	7.8	14	I61	subunit 1	4.4
5	F34	subunit 1	7.1	15	E38	subunit 2	4.4
6	I49	subunit 2	7.0	16	I61	subunit 2	4.2
7	I49	subunit 1	7.0	17	M58	subunit 2	3.9
8	F34	subunit 2	6.5	18	M58	subunit 1	3.9
9	E38	subunit 1	5.4	19	K30	subunit 1	3.7
10	E48	subunit 2	5.0	20	K30	subunit 2	3.4

Table G.2: Results of NAppEd network analysis - top 20 CII residues interacting with AMPAR LBDs. Numbering of AMPAR residues is in line with numbering in PDB 4U5D [151]. * Residues marked with an asterisk are not present in the 4U5D structure as it was obtained using a different GluA2 isoform than the 1FTJ structure, which was used for building the AMPAR LBD tetramer system.

Rank	**Residue**	**Subunit**	**Weighted degree**	**Main interaction type**	**Main interaction partner (subunit)**
1	Q37	subunit 1	7983	H-bond	E487 (A)
2	Q37	subunit 2	4953	H-bond	V484 (C)
3	Y54	subunit 2	3765	van der Waals	K752 (B)
4	A86	subunit 2	3645	H-bond	K752 (B)
5	Y54	subunit 1	3444	van der Waals	K752 (D)
6	A86	subunit 1	3401	H-bond	K752 (D)
7	E48	subunit 1	3055	H-bond	R660 (A)
8	E48	subunit 2	3045	H-bond	R660 (C)
9	I49	subunit 2	2870	van der Waals	E755 (B)
10	I49	subunit 1	2862	van der Waals	Q756 (D)
11	N47	subunit 1	2085	H-bond	Q756 (D)
12	E38	subunit 1	2033	ionic	K458 (A)
13	I61	subunit 1	1994	van der Waals	N744* (D)
14	M58	subunit 2	1927	van der Waals	A745* (B)
15	N47	subunit 1	1848	van der Waals	K663 (C)
16	R62	subunit 1	1781	van der Waals	L742 (D)
17	R62	subunit 2	1768	van der Waals	L742 (B)
18	M58	subunit 1	1764	van der Waals	A745* (D)
19	I61	subunit 2	1743	van der Waals	N744* (B)
20	E38	subunit 2	1723	ionic	K458 (C)

Table G.3: Interactions of CII A86 with AMPAR LBDs from analysis with NAppEd, ranked according to weight (number of frames a given interaction is present in).

CII toxin residue	Toxin subunit	AMPAR residue	AMPAR subunit	Interaction type	Weight	Max_persistence
A86	1	K752	D	H-bond	1143	150
A86	2	K752	B	H-bond	1024	150
A86	2	Q756	B	van der Waals	946	48
A86	1	Q756	D	van der Waals	934	44
A86	1	Q756	D	H-bond	758	150
A86	2	Q756	B	H-bond	527	121
A86	1	H435	D	van der Waals	401	27
A86	2	H435	B	van der Waals	334	11
A86	2	H435	B	H-bond	284	80
A86	2	K663	C	H-bond	256	83
A86	2	K752	B	van der Waals	116	7
A86	2	K663	C	van der Waals	110	12
A86	1	K752	D	van der Waals	72	3
A86	1	K663	C	H-bond	37	7
A86	1	H435	D	H-bond	21	5
A86	2	K434	B	H-bond	17	6
A86	1	K663	C	van der Waals	17	4
A86	2	L758*	B	van der Waals	17	3
A86	1	K434	D	H-bond	9	6
A86	2	I664	C	van der Waals	8	3
A86	1	K663	A	H-bond	7	2
A86	2	K434	B	van der Waals	6	2
A86	1	L758*	D	van der Waals	1	1
A86	1	K434	D	van der Waals	1	1

Table G.4: Interactions of CII E48 with AMPAR LBDs from analysis with NAppEd, ranked according to weight (number of frames a given interaction is present in).

CII toxin residue	Toxin subunit	AMPAR residue	AMPAR subunit	Interaction type	Weight	Max_persistence
E48	2	R660	C	H-bond	1173	146
E48	1	R660	A	H-bond	940	150
E48	2	R660	C	ionic	795	106
E48	1	R660	A	ionic	605	81
E48	1	R661	A	van der Waals	474	9
E48	1	K663	A	H-bond	424	85
E48	1	K663	A	ionic	422	104
E48	2	R661	C	van der Waals	355	9
E48	2	R660	C	van der Waals	207	7
E48	2	R453	C	H-bond	161	68
E48	2	R661	C	H-bond	118	33
E48	1	R660	A	van der Waals	112	5
E48	2	R453	C	ionic	68	64
E48	1	K663	A	van der Waals	60	5
E48	2	K663	C	H-bond	54	13
E48	2	K663	C	ionic	53	13
E48	2	V484	C	van der Waals	30	8
E48	1	R661	A	H-bond	18	15
E48	2	R661	C	ionic	13	7
E48	2	K663	C	van der Waals	13	3
E48	2	R453	C	van der Waals	4	1
E48	2	A455	C	van der Waals	1	1

Table G.5: Interactions of CII Q37 with AMPAR LBDs from analysis with NAppEd, ranked according to weight (number of frames a given interaction is present in).

CII toxin residue	Toxin subunit	AMPAR residue	AMPAR subunit	Interaction type	Weight	Max_persistence
Q37	1	E487	A	H-bond	1466	150
Q37	1	V484	A	H-bond	1414	150
Q37	1	E487	A	van der Waals	1289	35
Q37	1	V488	A	van der Waals	935	27
Q37	2	V484	C	H-bond	844	142
Q37	1	V484	A	van der Waals	831	19
Q37	2	E487	C	H-bond	739	150
Q37	2	E487	C	van der Waals	691	46
Q37	1	R453	A	H-bond	684	71
Q37	1	W460	A	van der Waals	681	26
Q37	2	V488	C	van der Waals	625	19
Q37	2	V484	C	van der Waals	586	19
Q37	2	R453	C	H-bond	561	31
Q37	1	R453	A	van der Waals	492	35
Q37	2	R453	C	van der Waals	373	12
Q37	2	W460	C	van der Waals	287	17
Q37	1	W460	A	H-bond	173	11
Q37	2	K458	C	van der Waals	82	13
Q37	2	K458	C	H-bond	76	20
Q37	2	W460	C	H-bond	69	7
Q37	2	L483	C	H-bond	9	1
Q37	2	L483	C	van der Waals	1	1

Table G.6: Interactions of CII F34 with AMPAR LBDs from analysis with NAppEd, ranked according to weight (number of frames a given interaction is present in).

CII toxin residue	Toxin subunit	AMPAR residue	AMPAR subunit	Interaction type	Weight	Max_persistence
F34	1	V488	A	van der Waals	602	9
F34	2	V488	C	van der Waals	384	9
F34	2	W460	C	π-π stacking	239	48
F34	1	V468	A	van der Waals	226	10
F34	2	W460	C	van der Waals	166	16
F34	2	V468	C	van der Waals	138	4
F34	2	K458	C	van der Waals	57	15
F34	1	E487	A	H-bond	53	3
F34	1	W460	A	van der Waals	48	6
F34	1	W460	A	π-π stacking	46	4
F34	2	K738	C	van der Waals	41	9
F34	2	K458	C	H-bond	38	26
F34	2	E487	C	van der Waals	37	4
F34	2	K458	C	π-cation	32	15
F34	1	Y469	A	π-π stacking	24	3
F34	2	E487	C	H-bond	14	1
F34	2	R453	C	van der Waals	13	4
F34	1	R453	A	H-bond	7	2
F34	1	R453	A	van der Waals	4	2
F34	1	R453	A	π-cation	3	1
F34	1	K738	A	van der Waals	3	1
F34	1	Y469	A	van der Waals	2	1
F34	2	Y469	C	π-π stacking	2	1
F34	2	Y469	C	van der Waals	1	1

Appendix H

CII toxin interactions with AMPAR ATDs

Table H.1: Results of BUDE alanine scanning - top 20 CII residues interacting with AMPAR ATDs.

Rank	Residue	Subunit	BUDE AlaScan score	Rank	Residue	Subunit	BUDE AlaScan score
1	E74	subunit 1	6.9	11	Q22	subunit 1	2.4
2	E19	subunit 1	5.8	12	S25	subunit 2	2.2
3	E19	subunit 2	5.5	13	E11	subunit 1	1.7
4	D15	subunit 1	5.4	14	S70	subunit 2	1.7
5	E74	subunit 2	4.5	15	S70	subunit 1	1.7
6	Q22	subunit 2	3.4	16	N67	subunit 2	1.7
7	E28	subunit 2	3.0	17	S25	subunit 1	1.7
8	R27	subunit 2	2.9	18	K77	subunit 1	1.4
9	R23	subunit 2	2.7	19	E28	subunit 1	1.4
10	N67	subunit 1	2.7	20	R23	subunit 1	1.3

Table H.2: Results of NAppEd network analysis - top 20 CII residues interacting with AMPAR ATDs. AMPAR residue numbers in line with numbering of 4U5D [151].

Rank	**Residue**	**Subunit**	**Weighted degree**	**Main interaction type**	**Main interaction partner (subunit)**
1	Q22	subunit 1	3501	van der Waals	K128 (A)
2	Q22	subunit 2	3109	van der Waals	K128 (D)
3	E19	subunit 2	2645	H-bond	R187 (D)
4	N67	subunit 1	2642	van der Waals	R187 (A)
5	R27	subunit 2	2233	H-bond	D127 (C)
6	R23	subunit 2	2062	H-bond	D127 (D)
7	N67	subunit 2	1923	van der Waals	K153 (C)
8	S70	subunit 1	1709	H-bond	D127 (A)
9	E74	subunit 1	1677	van der Waals	K153 (A)
10	E19	subunit 1	1582	H-bond	K153 (B)
11	S25	subunit 2	1576	H-bond	Q155 (C)
12	D15	subunit 1	1550	ionic	K128 (B)
13	E74	subunit 2	1508	H-bond	K212 (B)
14	S70	subunit 2	1332	H-bond	E181 (D)
15	S25	subunit 1	1060	H-bond	K128 (A)
16	E11	subunit 1	362	H-bond	K128 (B)
17	R23	subunit 1	347	H-bond	E181 (A)
18	K77	subunit 1	343	H-bond	K183 (B)
19	N18	subunit 1	244	H-bond	Q155 (B)
20	S68	subunit 1	241	van der Waals	D127 (A)

List of abbreviations

(R,R)-2B *N*,*N*'-[biphenyl-4,4'-diyldi(2*R*)propane-2,1-diyl]dipropane-2-sulfonamide

3DMTR three-dimensional missense tolerance ratio

ABD agonist-binding domain

ACE acetyl

AD Alzheimer's disease

AMPA α-amino-3-hydroxy-5-methyl-4-isoxazolepropionic acid

AMPAR AMPA receptor

ATD amino-terminal domain

CaMKII calcium/calmodulin-dependent kinase II

CII con-ikot-ikot

CKAMP cysteine-knot AMPA receptor modulating protein

CNIH cornichon homolog

CTD carboxy-terminal domain

CTZ cyclothiazide

DLG4 discs large homolog 4

DMSO dimethyl sulfoxide

EAAT excitatory amino acid transporter

EDTA ethylenediaminetetraacetic acid

FBS Fetal Bovine Serum

FW 5-fluorowillardiine, 2-amino-3-(5-fluoro-2,4-dioxopyrimidin-1-yl)propanoic acid

GABA gamma aminobutyric acid

GFP green fluorescent protein

GSG1L germline-specific gene 1-like

GSH glutathione

HEK Human embryonic kidney

HEPES 4-(2-hydroxyethyl)-1-piperazineethanesulfonic acid

HRV Human Rhinovirus

iGluR ionotropic glutamate receptor

IPTG isopropyl β-D-1-thiogalactopyranoside

IRES internal ribosome entry site

KA kainate, (3S,4S)-3-(carboxymethyl)-4-(prop-1-en-2-yl)-L-proline

LBD ligand-binding domain

LRRTM2 leucine repeat rich transmembrane neuronal 2

LTD long-term depression

MD molecular dynamics

MEM Minimum Essential Medium

MS mass spectrometry

MTR missense tolerance ratio

MWCO molecular weight cut-off

NAppEd Network Analysis of protein-protein interactions - Edinburgh

NBQX 2,3-dioxo-6-nitro-1,2,3,4-tetrahydrobenzo[*f*]quinoxaline-7-sulfonamide

NHS *N*-hydroxysuccinimide

NMDA *N*-methyl-D-aspartic acid

NMDAR NMDA receptor

NME *N*-methyl amide

NMR nuclear magnetic resonance

NTD N-terminal domain

PME Particle mesh Ewald

Prrt1 proline-rich transmembrane protein 1

PSD postsynaptic density

PSD-95 postsynaptic density protein 95

PSP PreScission Protease

RIN residue interaction network

RING Residue Interaction Network Generator

RMSD root mean square deviation

RMSF root mean square fluctuation

RPM rotations per minute

SAP-90 synapse-associated protein 90

SDS-PAGE sodium dodecyl sulfate - polyacrylamide gel electrophoresis

SEM standard error of the mean

SynDIG4 synapse differentiation-induced gene 4

TARP transmembrane AMPAR regulatory protein

TMD transmembrane domain

TOF Time of Flight

Trx thioredoxin

vdW van der Waals

WT wild-type

Bibliography

[1] K. Araki, H. Meguro, E. Kushiya, C. Takayama, Y. Inoue, and M. Mishina, "Selective Expression of the Glutamate Receptor Channel δ2 Subunit in Cerebellar Purkinje Cells," *Biochemical and Biophysical Research Communications*, vol. 197, pp. 1267–1276, Dec. 1993.

[2] M. Yamazaki, K. Araki, A. Shibata, and M. Mishina, "Molecular cloning of a cDNA encoding a novel member of the mouse glutamate receptor channel family," *Biochemical and Biophysical Research Communications*, vol. 183, pp. 886–892, Mar. 1992. Publisher: Biochem Biophys Res Commun.

[3] H. Lomeli, R. Sprengel, D. J. Laurie, G. Köhr, A. Herb, P. H. Seeburg, and W. Wisden, "The rat delta-1 and delta-2 subunits extend the excitatory amino acid receptor family," *FEBS Letters*, vol. 315, pp. 318–322, Jan. 1993.

[4] E. Carrillo, C. U. Gonzalez, V. Berka, and V. Jayaraman, "Delta glutamate receptors are functional glycine- and D-serine–gated cation channels in situ," *Science Advances*, vol. 7, p. eabk2200, Dec. 2021. Publisher: American Association for the Advancement of Science.

[5] M. Itoh, L. Piot, L. Mony, P. Paoletti, and M. Yuzaki, "Lack of evidence for direct ligand-gated ion channel activity of GluD receptors," *Proceedings of the National Academy of Sciences*, vol. 121, p. e2406655121, July 2024. Publisher: Proceedings of the National Academy of Sciences.

[6] K. B. Hansen, L. P. Wollmuth, D. Bowie, H. Furukawa, F. S. Menniti, A. I. Sobolevsky, G. T. Swanson, S. A. Swanger, I. H. Greger, T. Nakagawa, C. J. McBain, V. Jayaraman, C.-M. Low, M. L. Dell'Acqua, J. S. Diamond, C. R. Camp, R. E. Perszyk, H. Yuan, and S. F. Traynelis, "Structure, Function, and Pharmacology of Glutamate Receptor Ion Channels," *Pharmacological Reviews*, vol. 73, pp. 298–487, Oct. 2021.

[7] M. Fossati, N. Assendorp, O. Gemin, S. Colasse, F. Dingli, G. Arras, D. Loew, and C. Charrier, "Trans-Synaptic Signaling through the Glutamate Receptor Delta-1 Medi-

ates Inhibitory Synapse Formation in Cortical Pyramidal Neurons," *Neuron*, vol. 104, pp. 1081–1094.e7, Dec. 2019. Publisher: Elsevier.

[8] L. Piot, C. Heroven, S. Bossi, J. Zamith, T. Malinauskas, C. Johnson, D. Wennagel, D. Stroebel, C. Charrier, A. R. Aricescu, L. Mony, and P. Paoletti, "GluD1 binds GABA and controls inhibitory plasticity," *Science*, vol. 382, pp. 1389–1394, Dec. 2023. Publisher: American Association for the Advancement of Science.

[9] A. I. Sobolevsky, M. P. Rosconi, and E. Gouaux, "X-ray structure, symmetry and mechanism of an AMPA-subtype glutamate receptor," *Nature*, vol. 462, pp. 745–756, Dec. 2009.

[10] B. Sommer, K. Keinänen, T. A. Verdoorn, W. Wisden, N. Burnashev, A. Herb, M. Kohler, T. Takagi, B. Sakmann, and P. H. Seeburg, "Flip and Flop: A Cell-Specific Functional Switch in Glutamate-Operated Channels of the CNS," *Science*, vol. 249, pp. 1580–1585, Sept. 1990. Publisher: American Association for the Advancement of Science.

[11] B. Sommer, M. Köhler, R. Sprengel, and P. H. Seeburg, "RNA editing in brain controls a determinant of ion flow in glutamate-gated channels," *Cell*, vol. 67, pp. 11–19, Oct. 1991.

[12] J. Schwenk, D. Baehrens, A. Haupt, W. Bildl, S. Boudkkazi, J. Roeper, B. Fakler, and U. Schulte, "Regional diversity and developmental dynamics of the AMPA-receptor proteome in the mammalian brain," *Neuron*, vol. 84, pp. 41–54, Oct. 2014.

[13] G. T. Swanson, S. K. Kamboj, and S. G. Cull-Candy, "Single-Channel Properties of Recombinant AMPA Receptors Depend on RNA Editing, Splice Variation, and Subunit Composition," *The Journal of Neuroscience*, vol. 17, pp. 58–69, Jan. 1997.

[14] N. G. Carlson, J. Howard, L. C. Gahring, and S. W. Rogers, "RNA editing (Q/R site) and flop/flip splicing of AMPA receptor transcripts in young and old brains," *Neurobiology of Aging*, vol. 21, pp. 599–606, July 2000.

[15] Y. Kawahara, K. Ito, H. Sun, M. Ito, I. Kanazawa, and S. Kwak, "Regulation of glutamate receptor RNA editing and ADAR mRNA expression in developing human normal and Down's syndrome brains," *Developmental Brain Research*, vol. 148, pp. 151–155, Jan. 2004.

[16] N. Burnashev, H. Monyer, P. H. Seeburg, and B. Sakmann, "Divalent ion permeability of AMPA receptor channels is dominated by the edited form of a single subunit," *Neuron*, vol. 8, pp. 189–198, Jan. 1992.

[17] M. Hollmann, M. Hartley, and S. Heinemann, "Ca2+ Permeability of KA-AMPA—Gated Glutamate Receptor Channels Depends on Subunit Composition," *Science*, vol. 252, pp. 851–853, May 1991. Publisher: American Association for the Advancement of Science.

[18] K. M. Partin, M. W. Fleck, and M. L. Mayer, "AMPA Receptor Flip/Flop Mutants Affecting Deactivation, Desensitization, and Modulation by Cyclothiazide, Aniracetam, and Thiocyanate," *The Journal of Neuroscience*, vol. 16, pp. 6634–6647, Nov. 1996.

[19] K. M. Partin, D. Bowie, and M. L. Mayer, "Structural determinants of allosteric regulation in alternatively spliced AMPA receptors," *Neuron*, vol. 14, pp. 833–843, Apr. 1995.

[20] Y. Zhao, S. Chen, A. C. Swensen, W.-J. Qian, and E. Gouaux, "Architecture and subunit arrangement of native AMPA receptors elucidated by cryo-EM," *Science*, vol. 364, pp. 355–362, Apr. 2019.

[21] G. H. Diering and R. L. Huganir, "The AMPA Receptor Code of Synaptic Plasticity," *Neuron*, vol. 100, pp. 314–329, Oct. 2018. Publisher: Elsevier.

[22] P. M. Matthews, A. Pinggera, D. Kampjut, and I. H. Greger, "Biology of AMPA receptor interacting proteins - From biogenesis to synaptic plasticity," *Neuropharmacology*, vol. 197, p. 108709, Oct. 2021.

[23] W. D. Leuschner and W. Hoch, "Subtype-specific Assembly of α-Amino-3-hydroxy-5-methyl-4-isoxazole Propionic Acid Receptor Subunits Is Mediated by Their N-terminal Domains *," *Journal of Biological Chemistry*, vol. 274, pp. 16907–16916, June 1999. Publisher: Elsevier.

[24] J. F. Watson, H. Ho, and I. H. Greger, "Synaptic transmission and plasticity require AMPA receptor anchoring via its N-terminal domain," *eLife*, vol. 6, Mar. 2017. Publisher: eLife Sciences Publications Ltd.

[25] T. Möykkynen, S. K. Coleman, A. Semenov, and K. Keinänen, "The N-terminal domain modulates α-amino-3-hydroxy-5-methyl-4-isoxazolepropionic acid (AMPA) receptor desensitization," *The Journal of Biological Chemistry*, vol. 289, pp. 13197–13205, May 2014.

[26] E. A. Golubeva, M. I. Lavrov, E. V. Radchenko, and V. A. Palyulin, "Diversity of AMPA Receptor Ligands: Chemotypes, Binding Modes, Mechanisms of Action, and Therapeutic Effects," *Biomolecules*, vol. 13, p. 56, Dec. 2022.

[27] T. Honoré, J. Lauridsen, and P. Krogsgaard-Larsen, "The Binding of [3H]AMPA, a Structural Analogue of Glutamic Acid, to Rat Brain Membranes," *Journal of Neurochemistry*, vol. 38, no. 1, pp. 173–178, 1982. _eprint: https://onlinelibrary.wiley.com/doi/pdf/10.1111/j.1471-4159.1982.tb10868.x.

[28] M. J. Sheardown, E. Nielsen, A. J. Hansen, P. Jacobsen, and T. Honoré, "2,3-Dihydroxy-6-nitro-7-sulfamoyl-benzo(F)quinoxaline: a Neuroprotectant for Cerebral Ischemia," *Science*, vol. 247, pp. 571–574, Feb. 1990. Publisher: American Association for the Advancement of Science.

[29] A. S. Leonard, M. A. Davare, M. C. Horne, C. C. Garner, and J. W. Hell, "SAP97 Is Associated with the α-Amino-3-hydroxy-5-methylisoxazole-4-propionic Acid Receptor GluR1 Subunit *," *Journal of Biological Chemistry*, vol. 273, pp. 19518–19524, July 1998. Publisher: Elsevier.

[30] H. Dong, P. Zhang, I. Song, R. S. Petralia, D. Liao, and R. L. Huganir, "Characterization of the Glutamate Receptor-Interacting Proteins GRIP1 and GRIP2," *Journal of Neuroscience*, vol. 19, pp. 6930–6941, Aug. 1999. Publisher: Society for Neuroscience Section: ARTICLE.

[31] Y. Serulle, S. Zhang, I. Ninan, D. Puzzo, M. McCarthy, L. Khatri, O. Arancio, and E. B. Ziff, "A GluR1-cGKII Interaction Regulates AMPA Receptor Trafficking," *Neuron*, vol. 56, pp. 670–688, Nov. 2007.

[32] A. P. Burada, R. Vinnakota, and J. Kumar, "Cryo-EM structures of the ionotropic glutamate receptor GluD1 reveal a non-swapped architecture," *Nature Structural & Molecular Biology*, vol. 27, pp. 84–91, Jan. 2020. Publisher: Nature Publishing Group.

[33] A. P. Burada, R. Vinnakota, and J. Kumar, "The architecture of GluD2 ionotropic delta glutamate receptor elucidated by cryo-EM," *Journal of Structural Biology*, vol. 211, p. 107546, Aug. 2020.

[34] D. Zhang, J. Ivica, J. M. Krieger, H. Ho, K. Yamashita, I. Stockwell, R. Baradaran, O. Cais, and I. H. Greger, "Structural mobility tunes signalling of the GluA1 AMPA glutamate receptor," *Nature*, vol. 621, pp. 877–882, Sept. 2023. Publisher: Nature Publishing Group.

[35] L. Chen, D. M. Chetkovich, R. S. Petralia, N. T. Sweeney, Y. Kawasaki, R. J. Wenthold, D. S. Bredt, and R. A. Nicoll, "Stargazin regulates synaptic targeting of AMPA receptors by two distinct mechanisms," *Nature*, vol. 408, pp. 936–943, Dec. 2000. Publisher: Nature Publishing Group.

[36] S. Tomita, L. Chen, Y. Kawasaki, R. S. Petralia, R. J. Wenthold, R. A. Nicoll, and D. S. Bredt, "Functional studies and distribution define a family of transmembrane AMPA receptor regulatory proteins," *The Journal of Cell Biology*, vol. 161, pp. 805–816, May 2003.

[37] J. Schwenk, N. Harmel, G. Zolles, W. Bildl, A. Kulik, B. Heimrich, O. Chisaka, P. Jonas, U. Schulte, B. Fakler, and N. Klöcker, "Functional Proteomics Identify Cornichon Proteins as Auxiliary Subunits of AMPA Receptors," *Science*, vol. 323, pp. 1313–1319, Mar. 2009. Publisher: American Association for the Advancement of Science.

[38] J. von Engelhardt, V. Mack, R. Sprengel, N. Kavenstock, K. W. Li, Y. Stern-Bach, A. B. Smit, P. H. Seeburg, and H. Monyer, "CKAMP44: A Brain-Specific Protein Attenuating Short-Term Synaptic Plasticity in the Dentate Gyrus," *Science*, vol. 327, pp. 1518–1522, Mar. 2010. Publisher: American Association for the Advancement of Science.

[39] J. Schwenk, N. Harmel, A. Brechet, G. Zolles, H. Berkefeld, C. S. Müller, W. Bildl, D. Baehrens, B. Hüber, A. Kulik, N. Klöcker, U. Schulte, and B. Fakler, "High-Resolution Proteomics Unravel Architecture and Molecular Diversity of Native AMPA Receptor Complexes," *Neuron*, vol. 74, pp. 621–633, May 2012. Publisher: Elsevier.

[40] L. Matt, L. M. Kirk, G. Chenaux, D. J. Speca, K. R. Puhger, M. C. Pride, M. Qneibi, T. Haham, K. E. Plambeck, Y. Stern-Bach, J. L. Silverman, J. N. Crawley, J. W. Hell, and E. Díaz, "SynDIG4/Prrt1 Is Required for Excitatory Synapse Development and Plasticity Underlying Cognitive Function," *Cell Reports*, vol. 22, pp. 2246–2253, Feb. 2018. Publisher: Elsevier.

[41] S. Tomita, H. Adesnik, M. Sekiguchi, W. Zhang, K. Wada, J. R. Howe, R. A. Nicoll, and D. S. Bredt, "Stargazin modulates AMPA receptor gating and trafficking by distinct domains," *Nature*, vol. 435, pp. 1052–1058, June 2005.

[42] T. P. McGee, C. Bats, M. Farrant, and S. G. Cull-Candy, "Auxiliary Subunit GSG1L Acts to Suppress Calcium-Permeable AMPA Receptor Function," *The Journal of Neuroscience: The Official Journal of the Society for Neuroscience*, vol. 35, pp. 16171–16179, Dec. 2015.

[43] A. S. Kato, M. B. Gill, M. T. Ho, H. Yu, Y. Tu, E. R. Siuda, H. Wang, Y.-W. Qian, E. S. Nisenbaum, S. Tomita, and D. S. Bredt, "Hippocampal AMPA Receptor Gating Controlled by Both TARP and Cornichon Proteins," *Neuron*, vol. 68, pp. 1082–1096, Dec. 2010. Publisher: Elsevier.

[44] M. B. Gill, A. S. Kato, M. F. Roberts, H. Yu, H. Wang, S. Tomita, and D. S. Bredt, "Cornichon-2 Modulates AMPA Receptor–Transmembrane AMPA Receptor Regulatory Protein Assembly to Dictate Gating and Pharmacology," *Journal of Neuroscience*, vol. 31, pp. 6928–6938, May 2011. Publisher: Society for Neuroscience Section: Articles.

[45] C. Bats, L. Groc, and D. Choquet, "The Interaction between Stargazin and PSD-95 Regulates AMPA Receptor Surface Trafficking," *Neuron*, vol. 53, pp. 719–734, Mar. 2007. Publisher: Elsevier.

[46] P. Opazo, S. Labrecque, C. M. Tigaret, A. Frouin, P. W. Wiseman, P. De Koninck, and D. Choquet, "CaMKII triggers the diffusional trapping of surface AMPARs through phosphorylation of stargazin," *Neuron*, vol. 67, pp. 239–252, July 2010.

[47] D. Nair, E. Hosy, J. D. Petersen, A. Constals, G. Giannone, D. Choquet, and J.-B. Sibarita, "Super-Resolution Imaging Reveals That AMPA Receptors Inside Synapses Are Dynamically Organized in Nanodomains Regulated by PSD95," *Journal of Neuroscience*, vol. 33, pp. 13204–13224, Aug. 2013. Publisher: Society for Neuroscience Section: Articles.

[48] H. D. MacGillavry, Y. Song, S. Raghavachari, and T. A. Blanpied, "Nanoscale Scaffolding Domains within the Postsynaptic Density Concentrate Synaptic AMPA Receptors," *Neuron*, vol. 78, pp. 615–622, May 2013. Publisher: Elsevier.

[49] R. M. Vaidya, J. Zhang, D. Nall, Y. Lee, E. C. Kim, D. Ma, F. Huang, H. Nonaka, S. Kiyonaka, I. Hamachi, H. J. Chung, and P. R. Selvin, "Nanoscale organization is changed in native, surface AMPARs by mouse brain region and tauopathy," July 2024. Pages: 2024.07.22.604547 Section: New Results.

[50] J. Peukes, C. Lovatt, C. Leistner, J. Boulanger, D. R. Morado, M. J. Fuller, W. Kukulski, F. Zhu, N. H. Komiyama, J. A. Briggs, S. G. Grant, and R. A. Frank, "The molecular infrastructure of glutamatergic synapses in the mammalian forebrain," *eLife*, vol. 13, Oct. 2024. Publisher: eLife Sciences Publications Limited.

[51] A.-H. Tang, H. Chen, T. P. Li, S. R. Metzbower, H. D. MacGillavry, and T. A. Blanpied, "A trans-synaptic nanocolumn aligns neurotransmitter release to receptors," *Nature*, vol. 536, pp. 210–214, Aug. 2016. Publisher: Nature Publishing Group.

[52] J. F. Watson, A. Pinggera, H. Ho, and I. H. Greger, "AMPA receptor anchoring at CA1 synapses is determined by N-terminal domain and TARP $\gamma 8$ interactions," *Nature Communications*, vol. 12, p. 5083, Aug. 2021. Publisher: Nature Publishing Group.

[53] A. M. Ramsey, A.-H. Tang, T. A. LeGates, X.-Z. Gou, B. E. Carbone, S. M. Thompson, T. Biederer, and T. A. Blanpied, "Subsynaptic positioning of AMPARs by LRRTM2 controls synaptic strength," *Science Advances*, vol. 7, p. eabf3126, Aug. 2021.

[54] K. Liouta, M. Lubas, V. Venugopal, J. Chabbert, C. Jeannière, C. Diaz, M. Munier, B. Tessier, S. Claverol, A. Favereaux, M. Sainlos, J. de Wit, M. Letellier, O. Thoumine, and I. Chamma, "LRRTM2 controls presynapse nano-organization and AMPA receptor sub-positioning through Neurexin-binding interface," *Nature Communications*, vol. 15, p. 8807, Oct. 2024. Publisher: Nature Publishing Group.

[55] M. Mondin, V. Labrousse, E. Hosy, M. Heine, B. Tessier, F. Levet, C. Poujol, C. Blanchet, D. Choquet, and O. Thoumine, "Neurexin-Neuroligin Adhesions Capture Surface-Diffusing AMPA Receptors through PSD-95 Scaffolds," *Journal of Neuroscience*, vol. 31, pp. 13500–13515, Sept. 2011. Publisher: Society for Neuroscience Section: Articles.

[56] B. Zuber, I. Nikonenko, P. Klauser, D. Muller, and J. Dubochet, "The mammalian central nervous synaptic cleft contains a high density of periodically organized complexes," *Proceedings of the National Academy of Sciences of the United States of America*, vol. 102, pp. 19192–19197, Dec. 2005. Publisher: National Academy of Sciences.

[57] Z. Martinez-Lozada and A. Ortega, "Milestone Review: Excitatory amino acid transporters – Beyond their expected function," *Journal of Neurochemistry*, vol. 165, no. 4, pp. 457–466, 2023. _eprint: https://onlinelibrary.wiley.com/doi/pdf/10.1111/jnc.15809.

[58] J. W. Olney, V. Rhee, and O. L. Ho, "Kainic acid: a powerful neurotoxic analogue of glutamate," *Brain Research*, vol. 77, pp. 507–512, Sept. 1974.

[59] J. D. Clements, R. A. J. Lester, G. Tong, C. E. Jahr, and G. L. Westbrook, "The Time Course of Glutamate in the Synaptic Cleft," *Science*, vol. 258, pp. 1498–1501, Nov. 1992. Publisher: American Association for the Advancement of Science.

[60] N. Armstrong and E. Gouaux, "Mechanisms for Activation and Antagonism of an AMPA-Sensitive Glutamate Receptor: Crystal Structures of the GluR2 Ligand Binding Core," *Neuron*, vol. 28, pp. 165–181, Oct. 2000.

[61] M. L. Prieto and L. P. Wollmuth, "Gating Modes in AMPA Receptors," *Journal of Neuroscience*, vol. 30, pp. 4449–4459, Mar. 2010. Publisher: Society for Neuroscience Section: Articles.

[62] C. L. Yuan, E. Y. Shi, J. Srinivasan, C. P. Ptak, R. E. Oswald, and L. M. Nowak, "Modulation of AMPA Receptor Gating by the Anticonvulsant Drug, Perampanel," *ACS Medic-*

inal Chemistry Letters, vol. 10, pp. 237–242, Mar. 2019. Publisher: American Chemical Society.

[63] J. Baranovic, S. Braunbeck, N. Zaki, S. Minniberger, M. Chebli, and A. J. Plested, "The action of Con-ikot-ikot toxin on single AMPA-type glutamate receptors," *Journal of General Physiology*, vol. 154, p. e202112912, Apr. 2022.

[64] C. Rosenmund, Y. Stern-Bach, and C. F. Stevens, "The Tetrameric Structure of a Glutamate Receptor Channel," *Science*, vol. 280, pp. 1596–1599, June 1998. Publisher: American Association for the Advancement of Science.

[65] W. Zhang, Y. Cho, E. Lolis, and J. R. Howe, "Structural and Single-Channel Results Indicate That the Rates of Ligand Binding Domain Closing and Opening Directly Impact AMPA Receptor Gating," *Journal of Neuroscience*, vol. 28, pp. 932–943, Jan. 2008. Publisher: Society for Neuroscience Section: Articles.

[66] M. V. Yelshanskaya, D. S. Patel, C. M. Kottke, M. G. Kurnikova, and A. I. Sobolevsky, "Opening of glutamate receptor channel to subconductance levels," *Nature*, vol. 605, pp. 172–178, May 2022. Publisher: Nature Publishing Group.

[67] Y. Sun, R. Olson, M. Horning, N. Armstrong, M. Mayer, and E. Gouaux, "Mechanism of glutamate receptor desensitization," *Nature*, vol. 417, no. 6886, pp. 245–253, 2002. Publisher: Nature.

[68] J. Gonzalez, M. Du, K. Parameshwaran, V. Suppiramaniam, and V. Jayaraman, "Role of dimer interface in activation and desensitization in AMPA receptors," *Proceedings of the National Academy of Sciences*, vol. 107, pp. 9891–9896, May 2010. Publisher: Proceedings of the National Academy of Sciences.

[69] E. C. Twomey, M. V. Yelshanskaya, R. A. Grassucci, J. Frank, and A. I. Sobolevsky, "Structural Bases of Desensitization in AMPA Receptor-Auxiliary Subunit Complexes," *Neuron*, vol. 94, pp. 569–580.e5, May 2017. Publisher: Elsevier.

[70] H. Anwar, X. Li, D. Bucher, and F. Nadim, "Functional roles of short-term synaptic plasticity with an emphasis on inhibition," *Current Opinion in Neurobiology*, vol. 43, pp. 71–78, Apr. 2017.

[71] S. J. Martin, P. D. Grimwood, and R. G. M. Morris, "Synaptic Plasticity and Memory: An Evaluation of the Hypothesis," *Annual Review of Neuroscience*, vol. 23, pp. 649–711, Mar. 2000. Publisher: Annual Reviews.

[72] S. Martin and R. Morris, "New life in an old idea: The synaptic plasticity and memory hypothesis revisited," *Hippocampus*, vol. 12, no. 5, pp. 609–636, 2002. _eprint: https://onlinelibrary.wiley.com/doi/pdf/10.1002/hipo.10107.

[73] T. Takeuchi, A. J. Duszkiewicz, and R. G. M. Morris, "The synaptic plasticity and memory hypothesis: encoding, storage and persistence," *Philosophical Transactions of the Royal Society B: Biological Sciences*, vol. 369, p. 20130288, Jan. 2014.

[74] R. A. Nicoll and D. Schmitz, "Synaptic plasticity at hippocampal mossy fibre synapses," *Nature Reviews Neuroscience*, vol. 6, pp. 863–876, Nov. 2005. Publisher: Nature Publishing Group.

[75] L. Nowak, P. Bregestovski, P. Ascher, A. Herbet, and A. Prochiantz, "Magnesium gates glutamate-activated channels in mouse central neurones," *Nature*, vol. 307, pp. 462–465, Feb. 1984.

[76] M. L. Mayer, G. L. Westbrook, and P. B. Guthrie, "Voltage-dependent block by Mg2+ of NMDA responses in spinal cord neurones," *Nature*, vol. 309, pp. 261–263, May 1984. Publisher: Nature Publishing Group.

[77] A. B. MacDermott, M. L. Mayer, G. L. Westbrook, S. J. Smith, and J. L. Barker, "NMDA-receptor activation increases cytoplasmic calcium concentration in cultured spinal cord neurones," *Nature*, vol. 321, pp. 519–522, May 1986. Publisher: Nature Publishing Group.

[78] P. Ascher and L. Nowak, "The role of divalent cations in the N-methyl-D-aspartate responses of mouse central neurones in culture.," *The Journal of Physiology*, vol. 399, no. 1, pp. 247–266, 1988. _eprint: https://onlinelibrary.wiley.com/doi/pdf/10.1113/jphysiol.1988.sp017078.

[79] A. Barria, V. Derkach, and T. Soderling, "Identification of the Ca2+/Calmodulin-dependent Protein Kinase II Regulatory Phosphorylation Site in the α-Amino-3-hydroxyl-5-methyl4-isoxazole-propionate-type Glutamate Receptor*," *Journal of Biological Chemistry*, vol. 272, pp. 32727–32730, Dec. 1997.

[80] S. Tomita, V. Stein, T. J. Stocker, R. A. Nicoll, and D. S. Bredt, "Bidirectional Synaptic Plasticity Regulated by Phosphorylation of Stargazin-like TARPs," *Neuron*, vol. 45, pp. 269–277, Jan. 2005.

[81] V. Derkach, A. Barria, and T. R. Soderling, "Ca2+/calmodulin-kinase II enhances channel conductance of α-amino-3-hydroxy-5-methyl-4-isoxazolepropionate type glutamate

receptors," *Proceedings of the National Academy of Sciences*, vol. 96, pp. 3269–3274, Mar. 1999. Publisher: Proceedings of the National Academy of Sciences.

[82] A. S. Kristensen, M. A. Jenkins, T. G. Banke, A. Schousboe, Y. Makino, R. C. Johnson, R. Huganir, and S. F. Traynelis, "Mechanism of Ca2+/calmodulin-dependent kinase II regulation of AMPA receptor gating," *Nature Neuroscience*, vol. 14, pp. 727–735, June 2011.

[83] I. Stockwell, J. F. Watson, and I. H. Greger, "Tuning synaptic strength by regulation of AMPA glutamate receptor localization," *BioEssays*, vol. 46, no. 7, p. 2400006, 2024. _eprint: https://onlinelibrary.wiley.com/doi/pdf/10.1002/bies.202400006.

[84] S. H. Shi, Y. Hayashi, R. S. Petralia, S. H. Zaman, R. J. Wenthold, K. Svoboda, and R. Malinow, "Rapid spine delivery and redistribution of AMPA receptors after synaptic NMDA receptor activation," *Science*, vol. 284, pp. 1811–1816, June 1999. Publisher: American Association for the Advancement of Science.

[85] K. Plant, K. A. Pelkey, Z. A. Bortolotto, D. Morita, A. Terashima, C. J. McBain, G. L. Collingridge, and J. T. R. Isaac, "Transient incorporation of native GluR2-lacking AMPA receptors during hippocampal long-term potentiation," *Nature Neuroscience*, vol. 9, pp. 602–604, May 2006. Publisher: Nature Publishing Group.

[86] K. M. Franks, C. F. Stevens, and T. J. Sejnowski, "Independent Sources of Quantal Variability at Single Glutamatergic Synapses," *Journal of Neuroscience*, vol. 23, pp. 3186–3195, Apr. 2003. Publisher: Society for Neuroscience Section: ARTICLE.

[87] K. T. Haas, B. Compans, M. Letellier, T. M. Bartol, D. Grillo-Bosch, T. J. Sejnowski, M. Sainlos, D. Choquet, O. Thoumine, and E. Hosy, "Pre-post synaptic alignment through neuroligin-1 tunes synaptic transmission efficiency," *eLife*, vol. 7, p. e31755, July 2018. Publisher: eLife Sciences Publications, Ltd.

[88] L. P. Savtchenko and D. A. Rusakov, "Moderate AMPA receptor clustering on the nanoscale can efficiently potentiate synaptic current," *Philosophical Transactions of the Royal Society B: Biological Sciences*, vol. 369, p. 20130167, Jan. 2014. Publisher: Royal Society.

[89] B. Compans, D. Choquet, and E. Hosy, "Review on the role of AMPA receptor nano-organization and dynamic in the properties of synaptic transmission," *Neurophotonics*, vol. 3, p. 041811, Nov. 2016.

[90] R. C. Carroll, D. V. Lissin, M. v. Zastrow, R. A. Nicoll, and R. C. Malenka, "Rapid redistribution of glutamate receptors contributes to long-term depression in hippocam-

pal cultures," *Nature Neuroscience*, vol. 2, pp. 454–460, May 1999. Publisher: Nature Publishing Group.

[91] J. Baranovic, "AMPA receptors in the synapse: Very little space and even less time," *Neuropharmacology*, vol. 196, p. 108711, Sept. 2021. Publisher: Pergamon.

[92] P. Opazo and D. Choquet, "A three-step model for the synaptic recruitment of AMPA receptors," *Molecular and Cellular Neuroscience*, vol. 46, pp. 1–8, Jan. 2011.

[93] A. J. Borgdorff and D. Choquet, "Regulation of AMPA receptor lateral movements," *Nature*, vol. 417, pp. 649–653, June 2002. Publisher: Nature Publishing Group.

[94] H. Adesnik, R. A. Nicoll, and P. M. England, "Photoinactivation of Native AMPA Receptors Reveals Their Real-Time Trafficking," *Neuron*, vol. 48, pp. 977–985, Dec. 2005.

[95] M. Heine, L. Groc, R. Frischknecht, J.-C. Béïque, B. Lounis, G. Rumbaugh, R. L. Huganir, L. Cognet, and D. Choquet, "Surface Mobility of Postsynaptic AMPARs Tunes Synaptic Transmission," *Science*, vol. 320, pp. 201–205, Apr. 2008. Publisher: American Association for the Advancement of Science.

[96] A. C. Penn, C. L. Zhang, F. Georges, L. Royer, C. Breillat, E. Hosy, J. D. Petersen, Y. Humeau, and D. Choquet, "Hippocampal LTP and contextual learning require surface diffusion of AMPA receptors," *Nature*, vol. 549, pp. 384–388, Sept. 2017. Publisher: Nature Publishing Group.

[97] P. Opazo, M. Sainlos, and D. Choquet, "Regulation of AMPA receptor surface diffusion by PSD-95 slots," *Current Opinion in Neurobiology*, vol. 22, pp. 453–460, June 2012.

[98] A. Constals, A. C. Penn, B. Compans, E. Toulmé, A. Phillipat, S. Marais, N. Retailleau, A. S. Hafner, F. Coussen, E. Hosy, and D. Choquet, "Glutamate-Induced AMPA Receptor Desensitization Increases Their Mobility and Modulates Short-Term Plasticity through Unbinding from Stargazin," *Neuron*, vol. 85, pp. 787–803, Feb. 2015. Publisher: Cell Press.

[99] K. L. Dürr, L. Chen, R. A. Stein, R. De Zorzi, I. M. Folea, T. Walz, H. S. Mchaourab, and E. Gouaux, "Structure and Dynamics of AMPA Receptor GluA2 in Resting, Pre-Open, and Desensitized States," *Cell*, vol. 158, pp. 778–792, Aug. 2014. Publisher: Cell Press.

[100] J. R. Meyerson, J. Kumar, S. Chittori, P. Rao, J. Pierson, A. Bartesaghi, M. L. Mayer, and S. Subramaniam, "Structural mechanism of glutamate receptor activation and desensitization," *Nature*, vol. 514, pp. 328–334, Oct. 2014. Publisher: Nature Publishing Group.

[101] J. García-Nafría, B. Herguedas, J. F. Watson, and I. H. Greger, "The dynamic AMPA receptor extracellular region: a platform for synaptic protein interactions," *The Journal of Physiology*, vol. 594, no. 19, pp. 5449–5458, 2016. _eprint: https://onlinelibrary.wiley.com/doi/pdf/10.1113/JP271844.

[102] J. Ivica, N. Kejzar, H. Ho, I. Stockwell, V. Kuchtiak, A. M. Scrutton, T. Nakagawa, and I. H. Greger, "Proton-triggered rearrangement of the AMPA receptor N-terminal domains impacts receptor kinetics and synaptic localization," *Nature Structural & Molecular Biology*, vol. 31, pp. 1601–1613, Oct. 2024. Publisher: Nature Publishing Group.

[103] L. Ning, R. Shen, B. Xie, Y. Jiang, X. Geng, and W. Dong, "AMPA receptors in Alzheimer disease: Pathological changes and potential therapeutic targets," *Journal of Neuropathology & Experimental Neurology*, vol. 83, pp. 895–906, Nov. 2024.

[104] T. Hanada, "Ionotropic Glutamate Receptors in Epilepsy: A Review Focusing on AMPA and NMDA Receptors," *Biomolecules*, vol. 10, p. 464, Mar. 2020. Number: 3 Publisher: Multidisciplinary Digital Publishing Institute.

[105] T. Eiro, T. Miyazaki, M. Hatano, W. Nakajima, T. Arisawa, Y. Takada, K. Kimura, A. Sano, K. Nakano, T. Mihara, Y. Takayama, N. Ikegaya, M. Iwasaki, A. Hishimoto, Y. Noda, T. Miyazaki, H. Uchida, H. Tani, N. Nagai, T. Koizumi, S. Nakajima, M. Mimura, N. Matsuda, K. Kanai, K. Takahashi, H. Ito, Y. Hirano, Y. Kimura, R. Matsumoto, A. Ikeda, and T. Takahashi, "Dynamics of AMPA receptors regulate epileptogenesis in patients with epilepsy," *Cell Reports Medicine*, vol. 4, p. 101020, May 2023.

[106] W. XiangWei, R. E. Perszyk, N. Liu, Y. Xu, S. Bhattacharya, G. H. Shaulsky, C. Smith-Hicks, A. Fatemi, A. E. Fry, K. Chandler, T. Wang, J. Vogt, J. S. Cohen, A. R. Paciorkowski, A. Poduri, Y. Zhang, S. Wang, Y. Wang, Q. Zhai, F. Fang, J. Leng, K. Garber, S. J. Myers, R.-T. Jauss, K. L. Park, T. A. Benke, J. R. Lemke, H. Yuan, Y. Jiang, and S. F. Traynelis, "Clinical and functional consequences of GRIA variants in patients with neurological diseases," *Cellular and Molecular Life Sciences*, vol. 80, p. 345, Nov. 2023.

[107] V. Salpietro, C. L. Dixon, H. Guo, O. D. Bello, J. Vandrovcova, S. Efthymiou, R. Maroofian, G. Heimer, L. Burglen, S. Valence, E. Torti, M. Hacke, J. Rankin, H. Tariq, E. Colin, V. Procaccio, P. Striano, K. Mankad, A. Lieb, S. Chen, L. Pisani, C. Bettencourt, R. Männikkö, A. Manole, A. Brusco, E. Grosso, G. B. Ferrero, J. Armstrong-Moron, S. Gueden, O. Bar-Yosef, M. Tzadok, K. G. Monaghan, T. Santiago-Sim, R. E. Person, M. T. Cho, R. Willaert, Y. Yoo, J.-H. Chae, Y. Quan, H. Wu, T. Wang, R. A. Bernier, K. Xia, A. Blesson, M. Jain, M. M. Motazacker, B. Jaeger, A. L. Schneider, K. Boysen, A. M. Muir, C. T. Myers, R. H. Gavrilova, L. Gunderson, L. Schultz-Rogers, E. W. Klee,

D. Dyment, M. Osmond, M. Parellada, C. Llorente, J. Gonzalez-Peñas, A. Carracedo, A. Van Haeringen, C. Ruivenkamp, C. Nava, D. Heron, R. Nardello, M. Iacomino, C. Minetti, A. Skabar, A. Fabretto, M. Raspall-Chaure, M. Chez, A. Tsai, E. Fassi, M. Shinawi, J. N. Constantino, R. De Zorzi, S. Fortuna, F. Kok, B. Keren, D. Bonneau, M. Choi, B. Benzeev, F. Zara, H. C. Mefford, I. E. Scheffer, J. Clayton-Smith, A. Macaya, J. E. Rothman, E. E. Eichler, D. M. Kullmann, and H. Houlden, "AMPA receptor GluA2 subunit defects are a cause of neurodevelopmental disorders," *Nature Communications*, vol. 10, p. 3094, July 2019. Publisher: Nature Publishing Group.

[108] B. Davies, L. A. Brown, O. Cais, J. Watson, A. J. Clayton, V. T. Chang, D. Biggs, C. Preece, P. Hernandez-Pliego, J. Krohn, A. Bhomra, S. R. F. Twigg, A. Rimmer, A. Kanapin, The WGS500 Consortium, A. Sen, Z. Zaiwalla, G. McVean, R. Foster, P. Donnelly, J. C. Taylor, E. Blair, D. Nutt, A. R. Aricescu, I. H. Greger, S. N. Peirson, J. Flint, and H. C. Martin, "A point mutation in the ion conduction pore of AMPA receptor GRIA3 causes dramatically perturbed sleep patterns as well as intellectual disability," *Human Molecular Genetics*, vol. 26, pp. 3869–3882, Oct. 2017.

[109] V. Ismail, L. G. Zachariassen, A. Godwin, M. Sahakian, S. Ellard, K. L. Stals, E. Baple, K. Tatton Brown, N. Foulds, G. Wheway, M. O. Parker, S. M. Lyngby, M. G. Pedersen, J. Desir, A. Bayat, M. Musgaard, M. Guille, A. S. Kristensen, and D. Baralle, "Identification and functional evaluation of GRIA1 missense and truncation variants in individuals with ID: An emerging neurodevelopmental syndrome," *The American Journal of Human Genetics*, vol. 109, pp. 1217–1241, July 2022. Publisher: Cell Press.

[110] T. Chiyonobu, S. Hayashi, K. Kobayashi, M. Morimoto, Y. Miyanomae, A. Nishimura, A. Nishimoto, C. Ito, I. Imoto, T. Sugimoto, Z. Jia, J. Inazawa, and T. Toda, "Partial tandem duplication of GRIA3 in a male with mental retardation," *American Journal of Medical Genetics Part A*, vol. 143A, no. 13, pp. 1448–1455, 2007. _eprint: https://onlinelibrary.wiley.com/doi/pdf/10.1002/ajmg.a.31798.

[111] Y. Wu, A. C. Arai, G. Rumbaugh, A. K. Srivastava, G. Turner, T. Hayashi, E. Suzuki, Y. Jiang, L. Zhang, J. Rodriguez, J. Boyle, P. Tarpey, F. L. Raymond, J. Nevelsteen, G. Froyen, M. Stratton, A. Futreal, J. Gecz, R. Stevenson, C. E. Schwartz, D. Valle, R. L. Huganir, and T. Wang, "Mutations in ionotropic AMPA receptor 3 alter channel properties and are associated with moderate cognitive impairment in humans," *Proceedings of the National Academy of Sciences*, vol. 104, pp. 18163–18168, Nov. 2007. Publisher: Proceedings of the National Academy of Sciences.

[112] M. Trivisano, M. E. Santarone, A. Micalizzi, A. Ferretti, M. L. Dentici, A. Novelli, F. Vigevano, and N. Specchio, "GRIA3 missense mutation is cause of an x-linked developmental and epileptic encephalopathy," *Seizure*, vol. 82, pp. 1–6, Nov. 2020.

[113] J. O. McNamara, J. H. Eubanks, J. D. McPherson, J. J. Wasmuth, G. A. Evans, and S. F. Heinemann, "Chromosomal localization of human glutamate receptor genes," *Journal of Neuroscience*, vol. 12, pp. 2555–2562, July 1992. Publisher: Society for Neuroscience Section: Articles.

[114] S. Petrovski, Q. Wang, E. L. Heinzen, A. S. Allen, and D. B. Goldstein, "Genic Intolerance to Functional Variation and the Interpretation of Personal Genomes," *PLOS Genetics*, vol. 9, p. e1003709, Aug. 2013. Publisher: Public Library of Science.

[115] J. Traynelis, M. Silk, Q. Wang, S. F. Berkovic, L. Liu, D. B. Ascher, D. J. Balding, and S. Petrovski, "Optimizing genomic medicine in epilepsy through a gene-customized approach to missense variant interpretation," *Genome Research*, vol. 27, pp. 1715–1729, Oct. 2017. Company: Cold Spring Harbor Laboratory Press Distributor: Cold Spring Harbor Laboratory Press Institution: Cold Spring Harbor Laboratory Press Label: Cold Spring Harbor Laboratory Press Publisher: Cold Spring Harbor Lab.

[116] R. E. Perszyk, A. S. Kristensen, P. Lyuboslavsky, and S. F. Traynelis, "Three-dimensional missense tolerance ratio analysis," *Genome Research*, vol. 31, pp. 1447–1461, Aug. 2021. Company: Cold Spring Harbor Laboratory Press Distributor: Cold Spring Harbor Laboratory Press Institution: Cold Spring Harbor Laboratory Press Label: Cold Spring Harbor Laboratory Press Publisher: Cold Spring Harbor Lab.

[117] B. Rinaldi, A. Bayat, L. G. Zachariassen, J.-H. Sun, Y.-H. Ge, D. Zhao, K. Bonde, L. H. Madsen, I. A. A. Awad, D. Bagiran, A. Sbeih, S. M. Shah, S. El-Sayed, S. M. Lyngby, M. G. Pedersen, C. Stenum-Berg, L. C. Walker, I. Krey, A. Delahaye-Duriez, L. T. Emrick, K. Sully, C. N. Murali, L. C. Burrage, J. A. Plaud Gonzalez, M. Parnes, J. Friedman, B. Isidor, J. Lefranc, S. Redon, D. Heron, C. Mignot, B. Keren, M. Fradin, C. Dubourg, S. Mercier, T. Besnard, B. Cogne, W. Deb, C. Rivier, D. Milani, M. F. Bedeschi, C. Di Napoli, F. Grilli, P. Marchisio, S. Koudijs, D. Veenma, E. Argilli, S. A. Lynch, P. Y. B. Au, F. E. Ayala Valenzuela, C. Brown, D. Masser-Frye, M. Jones, L. Patron Romero, W. L. Li, E. Thorpe, L. Hecher, J. Johannsen, J. Denecke, V. McNiven, A. Szuto, E. Wakeling, V. Cruz, V. Sency, H. Wang, J. Piard, F. Kortüm, T. Herget, T. Bierhals, A. Condell, B. Ben-Zeev, S. Kaur, J. Christodoulou, A. Piton, C. Zweier, C. Kraus, A. Micalizzi, M. Trivisano, N. Specchio, G. Lesca, R. S. Møller, Z. Tümer, M. Musgaard, B. Gerard, J. R. Lemke, Y. S. Shi, and A. S. Kristensen, "Gain-of-function

and loss-of-function variants in GRIA3 lead to distinct neurodevelopmental phenotypes," *Brain*, vol. 147, pp. 1837–1855, May 2024.

[118] M. A. Rogawski and T. Hanada, "Preclinical pharmacology of perampanel, a selective non-competitive AMPA receptor antagonist," *Acta Neurologica Scandinavica*, vol. 127, no. s197, pp. 19–24, 2013. _eprint: https://onlinelibrary.wiley.com/doi/pdf/10.1111/ane.12100.

[119] Y. S. Chan, R. Chi, F. Cheung, L. Xia, . Jack, H. Wong, T. B. Ng, and W. Y. Chan, "Snake venom toxins: toxicity and medicinal applications," *Applied Microbiology and Biotechnology*, vol. 100, no. 14, pp. 6165–6181, 2016.

[120] Z. Xia, D. He, Y. Wu, H. F. Kwok, and Z. Cao, "Scorpion venom peptides: Molecular diversity, structural characteristics, and therapeutic use from channelopathies to viral infections and cancers," *Pharmacological Research*, vol. 197, p. 106978, Nov. 2023.

[121] N. J. Saez, S. Senff, J. E. Jensen, S. Y. Er, V. Herzig, L. D. Rash, and G. F. King, "Spider-Venom Peptides as Therapeutics," *Toxins*, vol. 2, pp. 2851–2871, Dec. 2010. Number: 12 Publisher: Molecular Diversity Preservation International.

[122] W. E. Bjørn-Yoshimoto, I. B. L. Ramiro, M. Yandell, J. M. McIntosh, B. M. Olivera, L. Ellgaard, and H. Safavi-Hemami, "Curses or Cures: A Review of the Numerous Benefits Versus the Biosecurity Concerns of Conotoxin Research," *Biomedicines*, vol. 8, p. 235, Aug. 2020. Number: 8 Publisher: Multidisciplinary Digital Publishing Institute.

[123] K. d. C. F. Bordon, C. T. Cologna, E. C. Fornari-Baldo, E. L. Pinheiro-Júnior, F. A. Cerni, F. G. Amorim, F. A. P. Anjolette, F. A. Cordeiro, G. A. Wiezel, I. A. Cardoso, I. G. Ferreira, I. S. d. Oliveira, J. Boldrini-França, M. B. Pucca, M. A. Baldo, and E. C. Arantes, "From Animal Poisons and Venoms to Medicines: Achievements, Challenges and Perspectives in Drug Discovery," *Frontiers in Pharmacology*, vol. 11, July 2020. Publisher: Frontiers.

[124] S. Bowersox, T. Gadbois, T. Singh, M. Pettus, Y. Wang, and R. Luther, "Selective N-type neuronal voltage-sensitive calcium channel blocker, SNX-111, produces spinal antinociception in rat models of acute, persistent and neuropathic pain," *The Journal of pharmacology and experimental therapeutics*, vol. 279, pp. 1243–9, Jan. 1997.

[125] D. A. Scott, C. E. Wright, and J. A. Angus, "Actions of intrathecal ω-conotoxins CVID, GVIA, MVIIA, and morphine in acute and neuropathic pain in the rat," *European Journal of Pharmacology*, vol. 451, pp. 279–286, Sept. 2002.

[126] J. A. DeBin, J. E. Maggio, and G. R. Strichartz, "Purification and characterization of chlorotoxin, a chloride channel ligand from the venom of the scorpion," *The American Journal of Physiology*, vol. 264, pp. C361–369, Feb. 1993.

[127] "Study Details | Chimeric Antigen Receptor (CAR) T Cells With a Chlorotoxin Tumor-Targeting Domain for the Treatment of MMP2+ Recurrent or Progressive Glioblastoma | ClinicalTrials.gov."

[128] O. Castañeda, V. Sotolongo, A. M. Amor, R. Stöcklin, A. J. Anderson, A. L. Harvey, \. Engström, C. Wernstedt, and E. Karlsson, "Characterization of a potassium channel toxin from the Caribbean sea anemone *Stichodactyla helianthus*," *Toxicon*, vol. 33, pp. 603–613, May 1995.

[129] X. Wang, G. Li, J. Guo, Z. Zhang, S. Zhang, Y. Zhu, J. Cheng, L. Yu, Y. Ji, and J. Tao, "Kv1.3 Channel as a Key Therapeutic Target for Neuroinflammatory Diseases: State of the Art and Beyond," *Frontiers in Neuroscience*, vol. 13, p. 1393, Jan. 2020.

[130] K. Kalman, M. W. Pennington, M. D. Lanigan, A. Nguyen, H. Rauer, V. Mahnir, K. Paschetto, W. R. Kem, S. Grissmer, G. A. Gutman, E. P. Christian, M. D. Cahalan, R. S. Norton, and K. G. Chandy, "ShK-Dap22, a potent Kv1.3-specific immunosuppressive polypeptide," *The Journal of Biological Chemistry*, vol. 273, pp. 32697–32707, Dec. 1998.

[131] S. B. Long, X. Tao, E. B. Campbell, and R. MacKinnon, "Atomic structure of a voltage-dependent K+ channel in a lipid membrane-like environment," *Nature*, vol. 450, pp. 376–382, Nov. 2007. Publisher: Nature Publishing Group.

[132] M. H. Rashid and S. Kuyucak, "Affinity and Selectivity of ShK Toxin for the Kv1 Potassium Channels from Free Energy Simulations," *The Journal of Physical Chemistry B*, vol. 116, pp. 4812–4822, Apr. 2012. Publisher: American Chemical Society.

[133] M. H. Rashid, G. Heinzelmann, R. Huq, R. B. Tajhya, S. C. Chang, S. Chhabra, M. W. Pennington, C. Beeton, R. S. Norton, and S. Kuyucak, "A Potent and Selective Peptide Blocker of the Kv1.3 Channel: Prediction from Free-Energy Simulations and Experimental Confirmation," *PLoS ONE*, vol. 8, p. e78712, Nov. 2013. Publisher: Public Library of Science.

[134] C. Beeton, H. Wulff, S. Singh, S. Botsko, G. Crossley, G. A. Gutman, M. D. Cahalan, M. Pennington, and K. G. Chandy, "A novel fluorescent toxin to detect and investigate Kv1.3 channel up-regulation in chronically activated T lymphocytes," *The Journal of Biological Chemistry*, vol. 278, pp. 9928–9937, Mar. 2003.

[135] M. H. Rashid and S. Kuyucak, "Free energy simulations of binding of HsTx1 toxin to Kv1 potassium channels: The basis of Kv1.3/Kv1.1 selectivity," *Journal of Physical Chemistry B*, vol. 118, pp. 707–716, Jan. 2014. Publisher: American Chemical Society.

[136] M. H. Rashid, R. Huq, M. R. Tanner, S. Chhabra, K. K. Khoo, R. Estrada, V. Dhawan, S. Chauhan, M. W. Pennington, C. Beeton, S. Kuyucak, and R. S. Norton, "A potent and Kv1.3-selective analogue of the scorpion toxin HsTX1 as a potential therapeutic for autoimmune diseases," *Scientific Reports*, vol. 4, pp. 1–9, Mar. 2014. Publisher: Nature Publishing Groups.

[137] B. Lebrun, R. Romi-Lebrun, M. F. Martin-Eauclaire, A. Yasuda, M. Ishiguro, Y. Oyama, O. Pongs, and T. Nakajima, "A four-disulphide-bridged toxin, with high affinity towards voltage-gated K+ channels, isolated from Heterometrus spinnifer (Scorpionidae) venom.," *Biochemical Journal*, vol. 328, pp. 321–327, Nov. 1997.

[138] I. Regaya, C. Beeton, G. Ferrat, N. Andreotti, H. Darbon, M. De Waard, and J.-M. Sabatier, "Evidence for domain-specific recognition of SK and Kv channels by MTX and HsTx1 scorpion toxins," *The Journal of Biological Chemistry*, vol. 279, pp. 55690–55696, Dec. 2004.

[139] A. I. Kuzmenkov and A. A. Vassilevski, "Labelled animal toxins as selective molecular markers of ion channels: Applications in neurobiology and beyond," *Neuroscience Letters*, vol. 679, pp. 15–23, July 2018.

[140] P. H. Ergen, S. Shorter, V. Ntziachristos, and S. V. Ovsepian, "Neurotoxin-Derived Optical Probes for Biological and Medical Imaging," *Molecular Imaging and Biology*, vol. 25, pp. 799–814, Oct. 2023.

[141] C. Y. Chow and G. F. King, "Shining a Light on Venom-Peptide Receptors: Venom Peptides as Targeted Agents for In Vivo Molecular Imaging," *Toxins*, vol. 16, p. 307, July 2024. Number: 7 Publisher: Multidisciplinary Digital Publishing Institute.

[142] S. Pei, N. Wang, Z. Mei, D. Zhangsun, D. J. Craik, J. M. McIntosh, X. Zhu, and S. Luo, "Conotoxins targeting voltage-gated sodium ion channels," *Pharmacological Reviews*, Jan. 2024. Publisher: American Society for Pharmacology and Experimental Therapeutics Section: Review Article.

[143] L. Azam and J. M. McIntosh, "Alpha-conotoxins as pharmacological probes of nicotinic acetylcholine receptors," *Acta Pharmacologica Sinica*, vol. 30, pp. 771–783, June 2009. Publisher: Nature Publishing Group.

[144] H. E. Hannon and W. D. Atchison, "Omega-Conotoxins as Experimental Tools and Therapeutics in Pain Management," *Marine Drugs*, vol. 11, pp. 680–699, Mar. 2013.

[145] B. M. Olivera, "*Conus* Venom Peptides: Reflections from the Biology of Clades and Species," *Annual Review of Ecology and Systematics*, vol. 33, pp. 25–47, Nov. 2002.

[146] O. Buczek, B. M. Olivera, and G. Bulaj, "Propeptide Does Not Act as an Intramolecular Chaperone but Facilitates Protein Disulfide Isomerase-Assisted Folding of a Conotoxin Precursor," *Biochemistry*, vol. 43, pp. 1093–1101, Feb. 2004. Publisher: American Chemical Society.

[147] S. R. Woodward, L. J. Cruz, B. M. Olivera, and D. R. Hillyard, "Constant and hypervariable regions in conotoxin propeptides," *EMBO Journal*, vol. 9, no. 4, pp. 1015–1020, 1990. Publisher: European Molecular Biology Organization.

[148] N. Puillandre, D. Koua, P. Favreau, B. M. Olivera, and R. Stöcklin, "Molecular Phylogeny, Classification and Evolution of Conopeptides," *Journal of Molecular Evolution*, vol. 74, pp. 297–309, June 2012.

[149] M. McIntosh, L. J. Cruz, M. W. Hunkapiller, W. R. Gray, and B. M. Olivera, "Isolation and structure of a peptide toxin from the marine snail *Conus magus*," *Archives of Biochemistry and Biophysics*, vol. 218, pp. 329–334, Oct. 1982.

[150] C. S. Walker, S. Jensen, M. Ellison, J. A. Matta, W. Y. Lee, J. S. Imperial, N. Duclos, P. J. Brockie, D. M. Madsen, J. T. Isaac, B. Olivera, and A. V. Maricq, "A Novel \textit{Conus} Snail Polypeptide Causes Excitotoxicity by Blocking Desensitization of AMPA Receptors," *Current Biology*, vol. 19, pp. 900–908, June 2009. Publisher: Cell Press.

[151] L. Chen, K. L. Dürr, and E. Gouaux, "X-ray structures of AMPA receptor-cone snail toxin complexes illuminate activation mechanism.," *Science*, vol. 345, no. 6200, pp. 1021–1026, 2014.

[152] R. W. Teichert, E. C. Jimenez, and B. M. Olivera, "αS-Conotoxin RVIIIA: A Structurally Unique Conotoxin That Broadly Targets Nicotinic Acetylcholine Receptors," *Biochemistry*, vol. 44, pp. 7897–7902, May 2005. Publisher: American Chemical Society.

[153] M. Loughnan, A. Nicke, A. Jones, C. I. Schroeder, S. T. Nevin, D. J. Adams, P. F. Alewood, and R. J. Lewis, "Identification of a Novel Class of Nicotinic Receptor Antagonists: DIMERIC CONOTOXINS VxXIIA, VxXIIB, and VxXIIC FROM CONUS VEXILLUM*," *Journal of Biological Chemistry*, vol. 281, pp. 24745–24755, Aug. 2006.

[154] X. C. Rodriguez-Ruiz, M. B. Aguilar, M. A. Ortíz-Arellano, H. Safavi-Hemami, and E. López-Vera, "A Novel Dimeric Conotoxin, FrXXA, from the Vermivorous Cone Snail \textit{Conus fergusoni}, of the Eastern Pacific, Inhibits Nicotinic Acetylcholine Receptors," *Toxins*, vol. 14, Aug. 2022. Publisher: Multidisciplinary Digital Publishing Institute (MDPI).

[155] C. M. Hackney, P. F. Salcedo, E. Mueller, T. L. Koch, L. D. Kjelgaard, M. Watkins, L. G. Zachariassen, P. S. Tuelung, J. R. McArthur, D. J. Adams, A. S. Kristensen, B. Olivera, R. K. Finol-Urdaneta, H. Safavi-Hemami, J. P. Morth, and L. Ellgaard, "A previously unrecognized superfamily of macro-conotoxins includes an inhibitor of the sensory neuron calcium channel Cav2.3," *PLOS Biology*, vol. 21, p. e3002217, Aug. 2023. Publisher: Public Library of Science.

[156] E. Müller, C. M. Hackney, L. Ellgaard, and J. P. Morth, "High-resolution crystal structure of the Mu8.1 conotoxin from *Conus mucronatus*," *Acta Crystallographica Section F Structural Biology Communications*, vol. 79, pp. 240–246, Sept. 2023.

[157] H. Zell, "\textit{Conus striatus} shell photograph, CC BY-SA 3.0, https://commons.wikimedia.org/w/index.php?curid=17922876."

[158] S. H. Lee, C. Jin, E. Cai, P. Ge, Y. Ishitsuka, K. W. Teng, A. A. De Thomaz, D. Nall, M. Baday, O. Jeyifous, D. Demonte, C. M. Dundas, S. Park, J. Y. Delgado, W. N. Green, and P. R. Selvin, "Super-resolution imaging of synaptic and extra-synaptic AMPA receptors with Different-Sized fluorescent probes," *eLife*, vol. 6, July 2017. Publisher: eLife Sciences Publications Ltd.

[159] L. J. Harris, S. B. Larson, K. W. Hasel, J. Day, A. Greenwood, and A. McPherson, "The three-dimensional structure of an intact monoclonal antibody for canine lymphoma," *Nature*, vol. 360, pp. 369–372, Nov. 1992. Publisher: Nature Publishing Group.

[160] S. Spinelli, L. Frenken, D. Bourgeois, L. d. Ron, W. Bos, T. Verrips, C. Anguille, C. Cambillau, and M. Tegonil, "The crystal structure of a llama heavy chain variable domain," *Nature Structural Biology*, vol. 3, pp. 752–757, Sept. 1996. Publisher: Nature Publishing Group.

[161] F. Yang, L. G. Moss, and G. N. Phillips, "The molecular structure of green fluorescent protein," *Nature Biotechnology*, vol. 14, pp. 1246–1251, Oct. 1996. Publisher: Nature Publishing Group.

[162] A. A. Kermani, "A guide to membrane protein X-ray crystallography," *The FEBS Journal*, vol. 288, no. 20, pp. 5788–5804, 2021. _eprint: https://onlinelibrary.wiley.com/doi/pdf/10.1111/febs.15676.

[163] A. M. Gigolaev, A. I. Kuzmenkov, S. Peigneur, V. M. Tabakmakher, E. L. Pinheiro-Junior, A. O. Chugunov, R. G. Efremov, J. Tytgat, and A. A. Vassilevski, "Tuning Scorpion Toxin Selectivity: Switching From K V 1.1 to K V 1.3," *Frontiers in pharmacology*, July 2020.

[164] D. L. Mateos and V. Yarov-Yarovoy, "Structural modeling of peptide toxin–ion channel interactions using RosettaDock," *Proteins: Structure, Function, and Bioinformatics*, vol. 91, no. 7, pp. 872–889, 2023. _eprint: https://onlinelibrary.wiley.com/doi/pdf/10.1002/prot.26474.

[165] M. Italia, E. Ferrari, M. D. Luca, and F. Gardoni, "GluA3-containing AMPA receptors: From physiology to synaptic dysfunction in brain disorders," *Neurobiology of Disease*, vol. 161, p. 105539, 2021.

[166] I. H. Greger, J. F. Watson, and S. G. Cull-Candy, "Structural and Functional Architecture of AMPA-Type Glutamate Receptors and Their Auxiliary Proteins," *Neuron*, vol. 94, pp. 713–730, May 2017. Publisher: Elsevier.

[167] K. Fosgerau and T. Hoffmann, "Peptide therapeutics: current status and future directions," *Drug Discovery Today*, vol. 20, no. 1, pp. 122–128, 2015.

[168] L. Cao, B. Coventry, I. Goreshnik, B. Huang, W. Sheffler, J. S. Park, K. M. Jude, I. Marković, R. U. Kadam, K. H. G. Verschueren, K. Verstraete, S. T. R. Walsh, N. Bennett, A. Phal, A. Yang, L. Kozodoy, M. DeWitt, L. Picton, L. Miller, E.-M. Strauch, N. D. DeBouver, A. Pires, A. K. Bera, S. Halabiya, B. Hammerson, W. Yang, S. Bernard, L. Stewart, I. A. Wilson, H. Ruohola-Baker, J. Schlessinger, S. Lee, S. N. Savvides, K. C. Garcia, and D. Baker, "Design of protein-binding proteins from the target structure alone," *Nature*, vol. 605, pp. 551–560, May 2022. Publisher: Nature Publishing Group.

[169] Y. Tan, H. Wu, T. Wei, and X. Li, "Chemical Protein Synthesis: Advances, Challenges, and Outlooks," *Journal of the American Chemical Society*, vol. 142, pp. 20288–20298, Dec. 2020. Publisher: American Chemical Society.

[170] A. D. J. MacKerell, D. Bashford, M. Bellott, R. L. J. Dunbrack, J. D. Evanseck, M. J. Field, S. Fischer, J. Gao, H. Guo, S. Ha, D. Joseph-McCarthy, L. Kuchnir, K. Kuczera, F. T. K. Lau, C. Mattos, S. Michnick, T. Ngo, D. T. Nguyen, B. Prodhom, W. E. Reiher, B. Roux, M. Schlenkrich, J. C. Smith, R. Stote, J. Straub, M. Watanabe, J. Wiórkiewicz-Kuczera, D. Yin, and M. Karplus, "All-Atom Empirical Potential for Molecular Modeling and Dynamics Studies of Proteins," *The Journal of Physical Chemistry B*, vol. 102, pp. 3586–3616, Apr. 1998. Publisher: American Chemical Society.

[171] J. W. Ponder and D. A. Case, "Force fields for protein simulations," *Advances in Protein Chemistry*, vol. 66, pp. 27–85, 2003.

[172] J. A. Maier, C. Martinez, K. Kasavajhala, L. Wickstrom, K. E. Hauser, and C. Simmerling, "ff14SB: Improving the Accuracy of Protein Side Chain and Backbone Parameters from ff99SB," *Journal of Chemical Theory and Computation*, vol. 11, pp. 3696–3713, July 2015.

[173] C. Tian, K. Kasavajhala, K. A. A. Belfon, L. Raguette, H. Huang, A. N. Migues, J. Bickel, Y. Wang, J. Pincay, Q. Wu, and C. Simmerling, "ff19SB: Amino-Acid-Specific Protein Backbone Parameters Trained against Quantum Mechanics Energy Surfaces in Solution," *Journal of Chemical Theory and Computation*, vol. 16, pp. 528–552, Jan. 2020. Publisher: American Chemical Society.

[174] M. Abraham, A. Alekseenko, V. Basov, C. Bergh, E. Briand, A. Brown, M. Doijade, G. Fiorin, S. Fleischmann, S. Gorelov, G. Gouaillardet, A. Gray, M. E. Irrgang, F. Jalalypour, J. Jordan, C. Kutzner, J. A. Lemkul, M. Lundborg, P. Merz, V. Miletic, D. Morozov, J. Nabet, S. Pall, A. Pasquadibisceglie, M. Pellegrino, H. Santuz, R. Schulz, T. Shugaeva, A. Shvetsov, A. Villa, S. Wingbermuehle, B. Hess, and E. Lindahl, "GROMACS 2024.3 Source code," Aug. 2024.

[175] P.-C. Do, E. H. Lee, and L. Le, "Steered Molecular Dynamics Simulation in Rational Drug Design," *Journal of Chemical Information and Modeling*, vol. 58, pp. 1473–1482, Aug. 2018.

[176] J. A. McCammon, B. R. Gelin, and M. Karplus, "Dynamics of folded proteins," *Nature*, vol. 267, no. 5612, pp. 585–590, 1977. Publisher: Nature Publishing Group.

[177] D. E. Shaw, M. M. Deneroff, R. O. Dror, J. S. Kuskin, R. H. Larson, J. K. Salmon, C. Young, B. Batson, K. J. Bowers, J. C. Chao, M. P. Eastwood, J. Gagliardo, J. P. Grossman, C. R. Ho, D. J. Ierardi, I. Kolossváry, J. L. Klepeis, T. Layman, C. McLeavey, M. A. Moraes, R. Mueller, E. C. Priest, Y. Shan, J. Spengler, M. Theobald, B. Towles, and S. C. Wang, "Anton, a special-purpose machine for molecular dynamics simulation," *Commun. ACM*, vol. 51, pp. 91–97, July 2008.

[178] D. E. Shaw, J. Grossman, J. A. Bank, B. Batson, J. A. Butts, J. C. Chao, M. M. Deneroff, R. O. Dror, A. Even, C. H. Fenton, A. Forte, J. Gagliardo, G. Gill, B. Greskamp, C. R. Ho, D. J. Ierardi, L. Iserovich, J. S. Kuskin, R. H. Larson, T. Layman, L.-S. Lee, A. K. Lerer, C. Li, D. Killebrew, K. M. Mackenzie, S. Y.-H. Mok, M. A. Moraes, R. Mueller, L. J. Nociolo, J. L. Peticolas, T. Quan, D. Ramot, J. K. Salmon, D. P. Scarpazza, U. B. Schafer, N. Siddique, C. W. Snyder, J. Spengler, P. T. P. Tang, M. Theobald, H. Toma,

B. Towles, B. Vitale, S. C. Wang, and C. Young, "Anton 2: Raising the Bar for Performance and Programmability in a Special-Purpose Molecular Dynamics Supercomputer," in *SC '14: Proceedings of the International Conference for High Performance Computing, Networking, Storage and Analysis*, pp. 41–53, Nov. 2014. ISSN: 2167-4337.

[179] D. E. Shaw, P. J. Adams, A. Azaria, J. A. Bank, B. Batson, A. Bell, M. Bergdorf, J. Bhatt, J. A. Butts, T. Correia, R. M. Dirks, R. O. Dror, M. P. Eastwood, B. Edwards, A. Even, P. Feldmann, M. Fenn, C. H. Fenton, A. Forte, J. Gagliardo, G. Gill, M. Gorlatova, B. Greskamp, J. Grossman, J. Gullingsrud, A. Harper, W. Hasenplaugh, M. Heily, B. C. Heshmat, J. Hunt, D. J. Ierardi, L. Iserovich, B. L. Jackson, N. P. Johnson, M. M. Kirk, J. L. Klepeis, J. S. Kuskin, K. M. Mackenzie, R. J. Mader, R. McGowen, A. McLaughlin, M. A. Moraes, M. H. Nasr, L. J. Nociolo, L. O'Donnell, A. Parker, J. L. Peticolas, G. Pocina, C. Predescu, T. Quan, J. K. Salmon, C. Schwink, K. S. Shim, N. Siddique, J. Spengler, T. Szalay, R. Tabladillo, R. Tartler, A. G. Taube, M. Theobald, B. Towles, W. Vick, S. C. Wang, M. Wazlowski, M. J. Weingarten, J. M. Williams, and K. A. Yuh, "Anton 3: twenty microseconds of molecular dynamics simulation before lunch," in *Proceedings of the International Conference for High Performance Computing, Networking, Storage and Analysis*, SC '21, (New York, NY, USA), pp. 1–11, Association for Computing Machinery, Nov. 2021.

[180] D. Xu, M. J. Williamson, and R. C. Walker, "Advancements in Molecular Dynamics Simulations of Biomolecules on Graphical Processing Units," in *Annual Reports in Computational Chemistry*, vol. 6, pp. 2–19, Elsevier, Jan. 2010. ISSN: 1574-1400.

[181] S. Y. Joshi and S. A. Deshmukh, "A review of advancements in coarse-grained molecular dynamics simulations," *Molecular Simulation*, vol. 47, pp. 786–803, July 2021. Publisher: Taylor & Francis _eprint: https://doi.org/10.1080/08927022.2020.1828583.

[182] S. A. Hollingsworth and R. O. Dror, "Molecular Dynamics Simulation for All," *Neuron*, vol. 99, pp. 1129–1143, Sept. 2018. Publisher: Elsevier.

[183] J. Yoo, D. Winogradoff, and A. Aksimentiev, "Molecular dynamics simulations of DNA–DNA and DNA–protein interactions," *Current Opinion in Structural Biology*, vol. 64, pp. 88–96, 2020.

[184] R. Lazim, D. Suh, and S. Choi, "Advances in Molecular Dynamics Simulations and Enhanced Sampling Methods for the Study of Protein Systems," *International Journal of Molecular Sciences*, vol. 21, p. 6339, Jan. 2020. Number: 17 Publisher: Multidisciplinary Digital Publishing Institute.

[185] H. M. Berman, J. Westbrook, Z. Feng, G. Gilliland, T. N. Bhat, H. Weissig, I. N. Shindyalov, and P. E. Bourne, "The Protein Data Bank," *Nucleic Acids Research*, vol. 28, no. 1, pp. 235–242, 2000.

[186] N. Armstrong, Y. Sun, G.-Q. Chen, and E. Gouaux, "Structure of a glutamate-receptor ligand-binding core in complex with kainate," *Nature*, vol. 395, pp. 913–917, Oct. 1998.

[187] A. Hogner, J. R. Greenwood, T. Liljefors, M.-L. Lunn, J. Egebjerg, I. K. Larsen, E. Gouaux, and J. S. Kastrup, "Competitive Antagonism of AMPA Receptors by Ligands of Different Classes: Crystal Structure of ATPO Bound to the GluR2 Ligand-Binding Core, in Comparison with DNQX," *Journal of Medicinal Chemistry*, vol. 46, pp. 214–221, Jan. 2003. Publisher: American Chemical Society.

[188] R. Jin, T. G. Banke, M. L. Mayer, S. F. Traynelis, and E. Gouaux, "Structural basis for partial agonist action at ionotropic glutamate receptors," *Nature Neuroscience*, vol. 6, pp. 803–810, Aug. 2003. Publisher: Nature Publishing Group.

[189] M. M. Holm, M.-L. Lunn, S. F. Traynelis, J. S. Kastrup, and J. Egebjerg, "Structural determinants of agonist-specific kinetics at the ionotropic glutamate receptor 2," *Proceedings of the National Academy of Sciences*, vol. 102, pp. 12053–12058, Aug. 2005. Publisher: Proceedings of the National Academy of Sciences.

[190] J. Mendieta, G. Ramrez, and F. Gago, "Molecular dynamics simulations of the conformational changes of the glutamate receptor ligand-binding core in the presence of glutamate and kainate," *Proteins: Structure, Function and Genetics*, vol. 44, no. 4, pp. 460–469, 2001.

[191] Y. Arinaminpathy, M. S. Sansom, and P. C. Biggin, "Molecular dynamics simulations of the ligand-binding domain of the ionotropic glutamate receptor GluR2," *Biophysical Journal*, vol. 82, no. 2, pp. 676–683, 2002. Publisher: Elsevier.

[192] T. Mamonova, M. J. Yonkunas, and M. G. Kurnikova, "Energetics of the cleft closing transition and the role of electrostatic interactions in conformational rearrangements of the glutamate receptor ligand binding domain," *Biochemistry*, vol. 47, no. 42, pp. 11077–11085, 2008.

[193] M. Musgaard and P. C. Biggin, "Steered Molecular Dynamics Simulations Predict Conformational Stability of Glutamate Receptors," *Journal of Chemical Information and Modeling*, vol. 56, no. 9, pp. 1787–1797, 2016.

[194] J. Aittoniemi, M. O. Jensen, A. C. Pan, and D. E. Shaw, "Desensitization dynamics of the AMPA receptor.," *Structure (London, England : 1993)*, vol. 31, pp. 724–734.e3, June 2023. Place: United States.

[195] K. Speranskiy and M. Kurnikova, "On the binding determinants of the glutamate agonist with the glutamate receptor ligand binding domain," *Biochemistry*, vol. 44, no. 34, pp. 11508–11517, 2005.

[196] A. Y. Lau and B. Roux, "The Free Energy Landscapes Governing Conformational Changes in a Glutamate Receptor Ligand-Binding Domain," *Structure*, vol. 15, no. 10, pp. 1203–1214, 2007.

[197] T. Mamonova, K. Speranskiy, and M. Kurnikova, "Interplay between structural rigidity and electrostatic interactions in the ligand binding domain of GluR2.," *Proteins*, vol. 73, pp. 656–671, Nov. 2008. Place: United States.

[198] T. Wolter, T. Steinbrecher, and M. Elstner, "Computational Study of Synthetic Agonist Ligands of Ionotropic Glutamate Receptors," *PLoS ONE*, vol. 8, no. 3, 2013.

[199] H. Dong and H. X. Zhou, "Atomistic mechanism for the activation and desensitization of an AMPA-subtype glutamate receptor," *Nature Communications*, vol. 2, no. 1, 2011. Publisher: Nature Publishing Group.

[200] J. Biedermann, S. Braunbeck, A. J. R. Plested, and H. Sun, "Nonselective cation permeation in an AMPA-type glutamate receptor," *Proceedings of the National Academy of Sciences*, vol. 118, no. 8, p. e2012843118, 2021. _eprint: https://www.pnas.org/doi/pdf/10.1073/pnas.2012843118.

[201] F. K. Schackert, J. Biedermann, S. Abdolvand, S. Minniberger, C. Song, A. J. R. Plested, P. Carloni, and H. Sun, "Mechanism of Calcium Permeation in a Glutamate Receptor Ion Channel," *Journal of Chemical Information and Modeling*, vol. 63, pp. 1293–1300, Feb. 2023. Publisher: American Chemical Society.

[202] A. Sumino, T. Sumikama, Y. Zhao, H. Flechsig, K. Umeda, N. Kodera, H. Konno, M. Hattori, and M. Shibata, "High-Speed Atomic Force Microscopy Reveals Fluctuations and Dimer Splitting of the N-Terminal Domain of GluA2 Ionotropic Glutamate Receptor-Auxiliary Subunit Complex," *ACS Nano*, vol. 18, pp. 25018–25035, Sept. 2024. Publisher: American Chemical Society.

[203] G. C. K. W. Koh, P. Porras, B. Aranda, H. Hermjakob, and S. E. Orchard, "Analyzing Protein–Protein Interaction Networks," *Journal of Proteome Research*, vol. 11, pp. 2014–2031, Apr. 2012. Publisher: American Chemical Society.

[204] D. Szklarczyk, A. L. Gable, K. C. Nastou, D. Lyon, R. Kirsch, S. Pyysalo, N. T. Doncheva, M. Legeay, T. Fang, P. Bork, L. J. Jensen, and C. von Mering, "The STRING database in 2021: customizable protein–protein networks, and functional characterization of user-uploaded gene/measurement sets," *Nucleic Acids Research*, vol. 49, pp. D605–D612, Jan. 2021.

[205] P. H. Guzzi, L. Di Paola, A. Giuliani, and P. Veltri, "PCN-Miner: an open-source extensible tool for the analysis of Protein Contact Networks," *Bioinformatics*, vol. 38, pp. 4235–4237, Sept. 2022.

[206] S. Rosignoli, L. di Paola, and A. Paiardini, "PyPCN: protein contact networks in PyMOL," *Bioinformatics*, vol. 39, p. btad675, Nov. 2023.

[207] D. K. Brown, D. L. Penkler, O. Sheik Amamuddy, C. Ross, A. R. Atilgan, C. Atilgan, and O. Tastan Bishop, "MD-TASK: a software suite for analyzing molecular dynamics trajectories," *Bioinformatics*, vol. 33, pp. 2768–2771, Sept. 2017.

[208] O. Sheik Amamuddy, M. Glenister, T. Tshabalala, and O. Tastan Bishop, "MDM-TASK-web: MD-TASK and MODE-TASK web server for analyzing protein dynamics," *Computational and Structural Biotechnology Journal*, vol. 19, pp. 5059–5071, 2021.

[209] B. Chakrabarty, V. Naganathan, K. Garg, Y. Agarwal, and N. Parekh, "NAPS update: network analysis of molecular dynamics data and protein–nucleic acid complexes," *Nucleic Acids Research*, vol. 47, pp. W462–W470, July 2019.

[210] C. Motono, S. Yanagida, M. Sato, and T. Hirokawa, "MDContactCom: a tool to identify differences of protein molecular dynamics from two MD simulation trajectories in terms of interresidue contacts," *Bioinformatics*, vol. 38, pp. 273–274, Dec. 2021.

[211] D. Mercadante, F. Gräter, and C. Daday, "CONAN: A Tool to Decode Dynamical Information from Molecular Interaction Maps," *Biophysical Journal*, vol. 114, pp. 1267–1273, Mar. 2018.

[212] S. Contreras-Riquelme, J.-A. Garate, T. Perez-Acle, and A. J. Martin, "RIP-MD: a tool to study residue interaction networks in protein molecular dynamics," *PeerJ*, vol. 6, p. e5998, Dec. 2018.

[213] A. Ribeiro and V. Ortiz, "MDN: A Web Portal for Network Analysis of Molecular Dynamics Simulations," *Biophysical Journal*, vol. 109, pp. 1110–1116, Sept. 2015.

[214] O. Sercinoglu and P. Ozbek, "gRINN: a tool for calculation of residue interaction energies and protein energy network analysis of molecular dynamics simulations," *Nucleic Acids Research*, vol. 46, pp. W554–W562, July 2018.

[215] A. Spanò, L. Fanton, D. Pizzolato, J. Moi, F. Vinci, A. Pesce, C. J. Dongmo Foumthuim, A. Giacometti, and M. Simeoni, "Rinmaker: a fast, versatile and reliable tool to determine residue interaction networks in proteins," *BMC Bioinformatics*, vol. 24, p. 336, Sept. 2023.

[216] A. Del Conte, G. F. Camagni, D. Clementel, G. Minervini, A. M. Monzon, C. Ferrari, D. Piovesan, and S. E. Tosatto, "RING 4.0: faster residue interaction networks with novel interaction types across over 35,000 different chemical structures," *Nucleic Acids Research*, vol. 52, pp. W306–W312, July 2024.

[217] D. Clementel, A. Del Conte, A. M. Monzon, G. Camagni, G. Minervini, D. Piovesan, and S. C. E. Tosatto, "RING 3.0: fast generation of probabilistic residue interaction networks from structural ensembles," *Nucleic Acids Research*, vol. 50, pp. W651–W656, July 2022.

[218] A. J. M. Martin, M. Vidotto, F. Boscariol, T. Di Domenico, I. Walsh, and S. C. E. Tosatto, "RING: networking interacting residues, evolutionary information and energetics in protein structures," *Bioinformatics*, vol. 27, pp. 2003–2005, July 2011. Publisher: Oxford Academic.

[219] D. Piovesan, G. Minervini, and S. Tosatto, "The RING 2.0 web server for high quality residue interaction networks," *Nucleic Acids Research*, vol. 44, pp. W367–W374, July 2016. Publisher: Oxford Academic.

[220] A. I. Derman, W. A. Prinz, D. Belin, and J. Beckwith, "Mutations that Allow Disulfide Bond Formation in the Cytoplasm of *Escherichia coli*," *Science*, vol. 262, pp. 1744–1747, Dec. 1993.

[221] E. J. Stewart, F. Åslund, and J. Beckwith, "Disulfide bond formation in the Escherichia coli cytoplasm: an in vivo role reversal for the thioredoxins," *The EMBO Journal*, vol. 17, pp. 5543–5550, Oct. 1998.

[222] P. H. Bessette, F. Åslund, J. Beckwith, and G. Georgiou, "Efficient folding of proteins with multiple disulfide bonds in the *Escherichia coli* cytoplasm," *Proceedings of the National Academy of Sciences*, vol. 96, pp. 13703–13708, Nov. 1999.

[223] V. D. Nguyen, F. Hatahet, K. E. Salo, E. Enlund, C. Zhang, and L. W. Ruddock, "Pre-expression of a sulfhydryl oxidase significantly increases the yields of eukaryotic disulfide bond containing proteins expressed in the cytoplasm of E.coli," *Microbial Cell Factories*, vol. 10, p. 1, Jan. 2011.

[224] L. D. Nielsen, M. M. Foged, A. Albert, A. B. Bertelsen, C. L. Søltoft, S. D. Robinson, S. V. Petersen, A. W. Purcell, B. M. Olivera, R. S. Norton, T. Vasskog, H. Safavi-Hemami, K. Teilum, and L. Ellgaard, "The three-dimensional structure of an H-superfamily conotoxin reveals a granulin fold arising from a common ICK cysteine framework," *Journal of Biological Chemistry*, vol. 294, pp. 8745–8759, May 2019.

[225] A. B. Bertelsen, C. M. Hackney, C. N. Bayer, L. D. Kjelgaard, M. Rennig, B. Christensen, E. S. Sørensen, H. Safavi-Hemami, T. Wulff, L. Ellgaard, and M. H. H. Nørholm, "DisCoTune: versatile auxiliary plasmids for the production of disulphide-containing proteins and peptides in the E. coli T7 system," *Microbial Biotechnology*, vol. 14, no. 6, pp. 2566–2580, 2021. _eprint: https://onlinelibrary.wiley.com/doi/pdf/10.1111/1751-7915.13895.

[226] P. Eastman, M. S. Friedrichs, J. D. Chodera, R. J. Radmer, C. M. Bruns, J. P. Ku, K. A. Beauchamp, T. J. Lane, L. P. Wang, D. Shukla, T. Tye, M. Houston, T. Stich, C. Klein, M. R. Shirts, and V. S. Pande, "OpenMM 4: A reusable, extensible, hardware independent library for high performance molecular simulation," *Journal of Chemical Theory and Computation*, vol. 9, pp. 461–469, Jan. 2013.

[227] E. C. Twomey and A. I. Sobolevsky, "Structural Mechanisms of Gating in Ionotropic Glutamate Receptors," *Biochemistry*, vol. 57, pp. 267–276, Jan. 2018.

[228] J. Wang, R. M. Wolf, J. W. Caldwell, P. A. Kollman, and D. A. Case, "Development and testing of a general Amber force field," *Journal of Computational Chemistry*, vol. 25, pp. 1157–1174, July 2004.

[229] J. B. Grimm, B. P. English, H. Choi, A. K. Muthusamy, B. P. Mehl, P. Dong, T. A. Brown, J. Lippincott-Schwartz, Z. Liu, T. Lionnet, and L. D. Lavis, "Bright photoactivatable fluorophores for single-molecule imaging," *Nature Methods*, vol. 13, pp. 985–988, Dec. 2016. Publisher: Nature Publishing Group.

[230] S. B. Needleman and C. D. Wunsch, "A general method applicable to the search for similarities in the amino acid sequence of two proteins," *Journal of Molecular Biology*, vol. 48, pp. 443–453, Mar. 1970.

[231] B. Herguedas, J. F. Watson, H. Ho, O. Cais, J. García-Nafría, and I. H. Greger, "Architecture of the heteromeric GluA1/2 AMPA receptor in complex with the auxiliary subunit TARP γ8," *Science*, vol. 364, Apr. 2019.

[232] D. Zhang, J. F. Watson, P. M. Matthews, O. Cais, and I. H. Greger, "Gating and modulation of a hetero-octameric AMPA glutamate receptor," *Nature*, vol. 594, pp. 454–458, June 2021.

[233] J. Yu, P. Rao, S. Clark, J. Mitra, T. Ha, and E. Gouaux, "Hippocampal AMPA receptor assemblies and mechanism of allosteric inhibition," *Nature 2021 594:7863*, vol. 594, pp. 448–453, May 2021. Publisher: Nature Publishing Group.

[234] M. B. Kastan, Q. Zhan, W. S. El-Deiry, F. Carrier, T. Jacks, W. V. Walsh, B. S. Plunkett, B. Vogelstein, and A. J. Fornace, "A mammalian cell cycle checkpoint pathway utilizing p53 and *GADD45* is defective in ataxia-telangiectasia," *Cell*, vol. 71, pp. 587–597, Nov. 1992.

[235] E. Yonish-Rouach, D. Resnftzky, J. Lotem, L. Sachs, A. Kimchi, and M. Oren, "Wild-type p53 induces apoptosis of myeloid leukaemic cells that is inhibited by interleukin-6," *Nature*, vol. 352, pp. 345–347, July 1991. Publisher: Nature Publishing Group.

[236] J. Momand, G. P. Zambetti, D. C. Olson, D. George, and A. J. Levine, "The *mdm-2* oncogene product forms a complex with the p53 protein and inhibits p53-mediated transactivation," *Cell*, vol. 69, pp. 1237–1245, June 1992.

[237] M. S. Greenblatt, W. P. Bennett, M. Hollstein, and C. C. Harris, "Mutations in the p53 tumor suppressor gene: clues to cancer etiology and molecular pathogenesis," *Cancer Research*, vol. 54, pp. 4855–4878, Sept. 1994.

[238] L. Cahilly-Snyder, T. Yang-Feng, U. Francke, and D. L. George, "Molecular analysis and chromosomal mapping of amplified genes isolated from a transformed mouse 3T3 cell line," *Somatic Cell and Molecular Genetics*, vol. 13, pp. 235–244, May 1987.

[239] P. H. Kussie, S. Gorina, V. Marechal, B. Elenbaas, J. Moreau, A. J. Levine, and N. P. Pavletich, "Structure of the MDM2 oncoprotein bound to the p53 tumor suppressor transactivation domain," *Science*, vol. 274, pp. 948–953, Nov. 1996.

[240] D. Case, I. Ben-Shalom, S. Brozell, D. Cerutti, T. Cheatham, III, V. Cruzeiro, T. Darden, R. Duke, D. Ghoreishi, G. Giambasu, T. Giese, M. Gilson, H. Sohlke, A. Goetz, D. Greene, R. Harris, N. Homeyer, Y. Huang, S. Izadi, A. Kovalenko, R. Krasny, T. Kurtzman, T. Lee, S. LeGrand, P. Li, C. Lin, J. Liu, T. Luchko, R. Luo, V. Man, D. Mermelstein, K. Merz, Y. Miao, G. Monrad, C. Nguyen, H. Nguyen, A. Onufriev, F. Pan, R. Qu, D. Roe, A. Roitberg, C. Sagui, S. Schott-Verdugo, J. Shen, C. Simmerling, J. Smith, J. Swails, R. Walker, J. Wang, H. Wei, L. Wilson, R. Wolf, X. Wu, L. Xiao, Y. Xiong, D. York, and P. Kollman, "AMBER2019," 2019.

[241] D. Case, K. Belfon, I. Ben-Shalom, S. Brozell, D. Cerutti, T. Cheatham III, V. Cruzeiro, T. Darden, R. Duke, G. Giambasu, M. Gilson, H. Gohlke, A. Goetz, R. Harris, S. Izadi, S. Izmailov, K. Kasavajhala, A. Kovalenko, R. Krasny, T. Kurtzman, T. Lee, S. LeGrans,

P. Li, C. Lin, J. Liu, T. Luchko, R. Luo, V. Man, K. Merz, Y. Miao, O. Mikhailovskii, G. Monard, H. Nguyen, A. Onufriev, F. Pan, S. Pantano, R. Qi, D. Roe, A. Roitberg, C. Sagui, S. Schott-Verdugo, J. Shen, C. Simmerling, N. Skrynnikov, J. Smith, J. Swails, R. Walker, H. Wang, L. Wilson, R. Wolf, X. Wu, Y. Xiong, Y. Xue, D. York, and P. Kollman, "AMBER 2020," 2020.

[242] W. L. Jorgensen, J. Chandrasekhar, J. D. Madura, R. W. Impey, and M. L. Klein, "Comparison of simple potential functions for simulating liquid water," *The Journal of Chemical Physics*, vol. 79, no. 2, pp. 926–935, 1983.

[243] P. Eastman, J. Swails, J. D. Chodera, R. T. McGibbon, Y. Zhao, K. A. Beauchamp, L.-P. P. Wang, A. C. Simmonett, M. P. Harrigan, C. D. Stern, R. P. Wiewiora, B. R. Brooks, and V. S. Pande, "OpenMM 7: Rapid development of high performance algorithms for molecular dynamics," *PLoS Computational Biology*, vol. 13, pp. 1–17, July 2017.

[244] J. J. Perez, M. Santos Tomas, and J. Rubio-Martinez, "Assessment of the Sampling Performance of Multiple-Copy Dynamics versus a Unique Trajectory," *Chemical Information and Modeling*, vol. 56, pp. 1950–1962, 2016.

[245] S. Yan, J. M. Peck, M. Ilgu, M. Nilsen-Hamilton, and M. H. Lamm, "Sampling Performance of Multiple Independent Molecular Dynamics Simulations of an RNA Aptamer," *ACS Omega*, vol. 5, Aug. 2020.

[246] J. A. Izaguirre, C. R. Sweet, and V. S. Pande, "Multiscale dynamics of macromolecules using normal mode Langevin.," *Pacific Symposium on Biocomputing*, pp. 240–51, 2010.

[247] U. Essmann, L. Perera, M. L. Berkowitz, T. Darden, H. Lee, and L. G. Pedersen, "A smooth particle mesh Ewald method," *The Journal of Chemical Physics*, vol. 103, pp. 8577–8593, Nov. 1995.

[248] J. Farmer, F. Kanwal, N. Nikulsin, M. C. Tsilimigras, and D. J. Jacobs, "Statistical measures to quantify similarity between molecular dynamics simulation trajectories," *Entropy*, vol. 19, Dec. 2017.

[249] D. R. Roe and T. E. Cheatham, "PTRAJ and CPPTRAJ: Software for processing and analysis of molecular dynamics trajectory data," *Journal of Chemical Theory and Computation*, vol. 9, pp. 3084–3095, July 2013. Publisher: American Chemical Society.

[250] D. R. Roe, "CPPTRAJ Manual," tech. rep., 2020.

[251] B. C. Cunningham and J. A. Wells, "High-resolution epitope mapping of hGH-receptor interactions by alanine-scanning mutagenesis," *Science*, vol. 244, no. 4908, pp. 1081–1085, 1989. Publisher: Science.

[252] I. Massova and P. A. Kollman, "Computational Alanine Scanning To Probe Protein-Protein Interactions: A Novel Approach To Evaluate Binding Free Energies," *Journal of the American Chemical Society*, vol. 121, pp. 8133–8143, Sept. 1999. Publisher: American Chemical Society.

[253] A. A. Ibarra, G. J. Bartlett, Z. Hegedüs, S. Dutt, F. Hobor, K. A. Horner, K. Hetherington, K. Spence, A. Nelson, T. A. Edwards, D. N. Woolfson, R. B. Sessions, and A. J. Wilson, "Predicting and Experimentally Validating Hot-Spot Residues at Protein-Protein Interfaces," *ACS Chemical Biology*, vol. 14, pp. 2252–2263, Oct. 2019.

[254] C. W. Wood, A. A. Ibarra, G. J. Bartlett, A. J. Wilson, D. N. Woolfson, and R. B. Sessions, "BAlaS: fast, interactive and accessible computational alanine-scanning using BudeAlaScan," *Bioinformatics*, vol. 36, pp. 2917–2919, May 2020.

[255] T. Kortemme and D. Baker, "A simple physical model for binding energy hot spots in protein-protein complexes," *Proceedings of the National Academy of Sciences of the United States of America*, vol. 99, pp. 14116–14121, Oct. 2002.

[256] R. T. McGibbon, K. A. Beauchamp, M. P. Harrigan, C. Klein, J. M. Swails, C. X. Hernández, C. R. Schwantes, L. P. Wang, T. J. Lane, and V. S. Pande, "MDTraj: A Modern Open Library for the Analysis of Molecular Dynamics Trajectories," *Biophysical Journal*, vol. 109, pp. 1528–1532, Oct. 2015. Publisher: Biophysical Society.

[257] A. A. Hagberg, D. A. Schult, and P. J. Swart, "Exploring Network Structure, Dynamics, and Function using NetworkX," in *Proceedings of the 7th Python in Science Conference* (G. Varoquaux, T. Vaught, and J. Millman, eds.), (Pasadena, CA USA), pp. 11 – 15, 2008.

[258] Bokeh Development Team, "Bokeh: Python library for interactive visualization," 2022.

[259] F. W. Studier and B. A. Moffatt, "Use of bacteriophage T7 RNA polymerase to direct selective high-level expression of cloned genes," *Journal of Molecular Biology*, vol. 189, pp. 113–130, May 1986.

[260] "SnapGene software (www.snapgene.com)."

[261] M. V. Nesterenko, M. Tilley, and S. J. Upton, "A simple modification of Blum's silver stain method allows for 30 minute detection of proteins in polyacrylamide gels," *Journal of Biochemical and Biophysical Methods*, vol. 28, pp. 239–242, Apr. 1994.

[262] A. J. R. Plested and M. H. Poulsen, "Crosslinking glutamate receptor ion channels," *Methods in Enzymology*, vol. 652, pp. 161–192, 2021.

[263] A. Böttger, V. Böttger, C. Garcia-Echeverria, P. Chène, H.-K. Hochkeppel, W. Sampson, K. Ang, S. F. Howard, S. M. Picksley, and D. P. Lane, "Molecular characterization of the hdm2-p53 interaction1," *Journal of Molecular Biology*, vol. 269, pp. 744–756, July 1997.

[264] P. Chène, "Inhibition of the p53-MDM2 interaction: targeting a protein-protein interface," *Molecular cancer research: MCR*, vol. 2, pp. 20–28, Jan. 2004.

[265] H. Zhong and H. A. Carlson, "Computational studies and peptidomimetic design for the human p53–MDM2 complex," *Proteins: Structure, Function, and Bioinformatics*, vol. 58, no. 1, pp. 222–234, 2005. _eprint: https://onlinelibrary.wiley.com/doi/pdf/10.1002/prot.20275.

[266] J. K. Murray and S. H. Gellman, "Targeting protein-protein interactions: lessons from p53/MDM2," *Biopolymers*, vol. 88, no. 5, pp. 657–686, 2007.

[267] Y. Ding, Y. Mei, and J. Z. H. Zhang, "Quantum Mechanical Studies of Residue-Specific Hydrophobic Interactions in p53MDM2 Binding," *The Journal of Physical Chemistry B*, vol. 112, pp. 11396–11401, Sept. 2008. Publisher: American Chemical Society.

[268] W. Cheng, Z. Liang, W. Wang, C. Yi, H. Li, S. Zhang, and Q. Zhang, "Insight into binding modes of p53 and inhibitors to MDM2 based on molecular dynamic simulations and principal component analysis," *Molecular Physics*, vol. 114, pp. 128–140, Jan. 2016. Publisher: Taylor & Francis _eprint: https://doi.org/10.1080/00268976.2015.1087598.

[269] A. C. Pan, D. Jacobson, K. Yatsenko, D. Sritharan, T. M. Weinreich, and D. E. Shaw, "Atomic-level characterization of protein–protein association," *Proceedings of the National Academy of Sciences*, vol. 116, pp. 4244–4249, Mar. 2019. Publisher: Proceedings of the National Academy of Sciences.

[270] M. T. Jacobsen, M. Fairhead, P. Fogelstrand, and M. Howarth, "Amine Landscaping to Maximize Protein-Dye Fluorescence and Ultrastable Protein-Ligand Interaction," *Cell Chemical Biology*, vol. 24, no. 8, pp. 1040–1047.e4, 2017.

[271] S. J. F. van der Spek, N. J. Pandya, F. Koopmans, I. Paliukhovich, R. C. van der Schors, M. Otten, A. B. Smit, and K. W. Li, "Expression and Interaction Proteomics of GluA1- and GluA3-Subunit-Containing AMPARs Reveal Distinct Protein Composition," *Cells*, vol. 11, p. 3648, Jan. 2022. Number: 22 Publisher: Multidisciplinary Digital Publishing Institute.

[272] D. Colquhoun, P. Jonas, and B. Sakmann, "Action of brief pulses of glutamate on AMPA/kainate receptors in patches from different neurones of rat hippocampal slices.,"

The Journal of Physiology, vol. 458, pp. 261–287, Dec. 1992. Publisher: Wiley-Blackwell.

[273] J. Santos-López, S. Gómez, F. J. Fernández, and M. C. Vega, "Protein-Protein Binding Kinetics by Biolayer Interferometry," in *Advanced Technologies for Protein Complex Production and Characterization: Volume II* (M. C. Vega and F. J. Fernández, eds.), pp. 73–88, Cham: Springer Nature Switzerland, 2024.

[274] A. Jug, T. Bratkovič, and J. Ilaš, "Biolayer interferometry and its applications in drug discovery and development," *TrAC Trends in Analytical Chemistry*, vol. 176, p. 117741, 2024.

[275] N. Durisic, L. L. Cuervo, and M. Lakadamyali, "Quantitative super-resolution microscopy: pitfalls and strategies for image analysis," *Current Opinion in Chemical Biology*, vol. 20, pp. 22–28, 2014.

[276] T. M. Dankovich and S. O. Rizzoli, "Challenges facing quantitative large-scale optical super-resolution, and some simple solutions," *iScience*, vol. 24, no. 3, p. 102134, 2021.

[277] M. Lelek, M. T. Gyparaki, G. Beliu, F. Schueder, J. Griffié, S. Manley, R. Jungmann, M. Sauer, M. Lakadamyali, and C. Zimmer, "Single-molecule localization microscopy," *Nature Reviews Methods Primers*, vol. 1, pp. 1–27, June 2021. Publisher: Nature Publishing Group.

[278] C. S. Theile, M. D. Witte, A. E. M. Blom, L. Kundrat, H. L. Ploegh, and C. P. Guimaraes, "Site-specific N-terminal labeling of proteins using sortase-mediated reactions," *Nature Protocols*, vol. 8, pp. 1800–1807, Sept. 2013. Publisher: Nature Publishing Group.

[279] M. Steinhagen, K. Zunker, K. Nordsieck, and A. G. Beck-Sickinger, "Large scale modification of biomolecules using immobilized sortase A from Staphylococcus aureus," *Bioorganic & Medicinal Chemistry*, vol. 21, no. 12, pp. 3504–3510, 2013.